8-8-2023

# Fractional Quantum Hall Effect Under Tilted Magnetic Fields in GaAs/AlGaAs Heterostructure Hall Bar Devices, and the Effect of Current Annealing in CVD Graphene Devices

Udagamage Wijewardena

# Fractional Quantum Hall Effect Under Tilted Magnetic Fields in GaAs/AlGaAs Heterostructure Hall Bar Devices, and the Effect of Current Annealing in CVD Graphene Devices

by

Udagamage Kushan Wijewardena

Under the Direction of Ramesh Mani, PhD

A Dissertation Submitted in Partial Fulfillment of the Requirements for the Degree of

Doctor of Philosophy

in the College of Arts and Sciences

Georgia State University

2023

ABSTRACT

This dissertation presents two distinct research studies. The first study focuses on the fractional quantum Hall effect (FQHE) observed in two-dimensional electron systems subjected to high transverse magnetic fields. Specifically, we investigate the interplay between Zeeman spin splitting and correlation energy in a GaAs/AlGaAs 2D electron system. By tuning the spin energy, we observe transitions in the quantized Hall effect, resulting in changes in both the resistivity minimum ($\rho_{xx}$) and the Hall resistance ($R_{xy}$). We also uncover a size dependence in the tilt angle interval for the vanishing of certain resistance minima, with observable shifts in $R_{xy}$. These findings highlight the competition and crossover between different spin polarized states and distinct FQHE phenomena.

The second study focuses on different methods of fabricating graphene devices, including exfoliation techniques such as dry transferring and creating heterostructures, as well as chemical vapor deposition (CVD). The main objective is to investigate the hysteresis effect in graphene devices. Graphene samples prepared using these methods often display p-type characteristics and significant hysteresis under ambient conditions. Current annealing has emerged as a promising in-situ approach for cleaning graphene samples. However, extended periods of current annealing may introduce defects in the underlying substrate. To address this concern, we examine the hysteresis behavior of a graphene Hall bar device before and after current annealing. The graphene sample, grown on copper foils via CVD, undergoes annealing with different current levels. Our experimental methodology involves studying electron/hole transport by cooling the sample from room temperature to 35 K while applying a back-gate bias. By analyzing the hysteresis characteristics, we obtain valuable insights into the impact of current annealing on the electrical properties of graphene.

These two studies contribute to our understanding of complex electronic phenomena and the behavior of graphene under different experimental conditions. The findings presented in this dissertation offer valuable insights into the underlying physics and practical considerations for these systems, paving the way for further research and potential technological applications.

INDEX WORDS: Fractional quantum Hall effect, Integer quantum Hall effect, Two dimensional electron gas, Magnetoresistance, Graphene, Tilted magnetic field, Spin polarization

Fractional Quantum Hall Effect Under Tilted Magnetic Fields in GaAs/AlGaAs Heterostructure Hall Bar Devices, and the Effect of Current Annealing in CVD Graphene Devices

by

Udagamage Kushan Wijewardena

Committee Chair: Ramesh Mani

Committee: Sidong Lei

Murad Sarsour

Mukesh Dhamala

Electronic Version Approved:

Office of Graduate Services

College of Arts and Sciences

Georgia State University

August 2023

## DEDICATION

To my wife Sujani, son Nithil, parents, brother, and family

## ACKNOWLEDGEMENTS

I am deeply grateful to Professor Ramesh Mani, my esteemed research advisor, for his guidance, support, and the nurturing environment he provided throughout my journey as a graduate student. His invaluable expertise and mentorship have been instrumental in shaping both my academic and personal growth. I would like to express my sincere gratitude to all the members of my committee for their support, insightful ideas, and inspiring discussions. Their collective wisdom and dedicated commitment in serving on my dissertation committee have immensely contributed to the depth and quality of my research.

I extend my heartfelt thanks to the past and present members of the Nanoscience, Low Temperature and High Magnetic Field Laboratory for their continual support and encouragement. Their collaborative spirit and shared passion for scientific inquiry have created a dynamic environment that fueled my curiosity and motivated me to push the boundaries of knowledge.

I am profoundly grateful to Georgia State University for the continuous support and the invaluable research opportunities provided throughout my doctoral studies. I would like to express my sincere appreciation to the Georgia State University Dissertation Grant Program for their generous financial assistance, which enabled the acquisition of essential research equipment and materials. Additionally, I am deeply grateful for the Provost Dissertation Fellowship, which not only provided vital financial support but also offered invaluable guidance and motivation, enabling me to accomplish my research goals and the dissertation in a timely manner.

Special thanks are due to our collaborators from ETH Zürich, Switzerland, for their generous contribution in providing us with the GaAs/AlGaAs samples. Their partnership and shared expertise have significantly broadened the scope and impact of my research.

Furthermore, I would like to extend my gratitude to the funding agencies that have generously supported my research, namely the National Science Foundation (NSF), Army Research Office (ARO), and Department of Energy (DOE). Their financial backing has not only facilitated the progress of my work but has also reaffirmed the importance and relevance of scientific exploration in addressing real-world challenges.

I wish to express my appreciation to all the members of the Instrument Shop at GSU for their support and technical assistance throughout my research journey. Their dedication and expertise have been pivotal in the successful execution of my experiments. I am sincerely grateful to all my colleagues at the Department of Physics and Astronomy at GSU. The collaborative and intellectually engaging environment within the department has created a strong sense of teamwork and facilitated productive discussions that have greatly enriched my academic experience.

Last but certainly not least, I am deeply indebted to my loving mother and father, brother, aunt Dr. Kanthi Herath, and other supportive relatives and friends, especially my wife, Sujani. Your commitment to supporting me during this challenging journey has been a constant source of strength and motivation. I am also grateful to my son, Nithil, whose infectious laughter and innocent joy have kept me entertained and filled my days with love. I recognize that this endeavor would have been far more challenging without the love and support of each and every one of you.

# TABLE OF CONTENTS

# LIST OF FIGURES

## LIST OF ABBREVIATIONS

2D: Two dimensional

2DEG: Two dimensional electron gas

QHE: Quantum Hall effect

IQHE: Integer quantum Hall effect

FQHE: Fractional quantum Hall effect

MOSFET: Metal-oxide-semiconductor field-effect transistor

MBE: Molecular beam epitaxy

LL: Landau level

CF: Composite Fermions

LPCVD: Low pressure chemical vapor deposition

CVD: Chemical vapor deposition

PDMS: Polydimethylsiloxane

AFM: Atomic force microscope

PMMA: Poly methyl methacrylate

MFC: Mass flow controller

OM: Optical microscope

CNP: Charge neutrality point

GV: Gate voltage

OVC: Outer vacuum chamber

# 1 INTRODUCTION

This dissertation consists of two parts. The first part focuses on magnetotransport measurements in the fractional quantum Hall regime conducted on a GaAs/AlGaAs Two-Dimensional Electron Gas (2DEG) system. These measurements were performed using a rotatable sample holder that was carefully assembled within a dry dilution refrigerator. The second part discusses fabrication of graphene-based devices by exfoliation and Chemical Vapor Deposition (CVD) techniques and investigates the impact of current annealing on the CVD graphene devices.

Chapter 2 presents a fundamental overview of the 2DEG and its behavior within external electric and magnetic fields. Initially, the requirements for observing the quantum effect are discussed in Section 2.1. Following that, the formation of a 2DEG at the interface of a Heterojunction, comprising semiconductors with distinct band gaps, is examined in section 2.2. The subsequent portion of this chapter delves into carrier transport within the 2DEG, the Hall effect, the Integer Quantum Hall Effect (IQHE), and the Fractional Quantum Hall Effect (FQHE).

Chapter 3 focuses on the FQHE in a tilted magnetic field, beginning with a concise introduction to previous research conducted on this topic. The remainder of the chapter reviews results from the publication titled "Size dependence and induced transformations of fractional quantum Hall effects under tilted magnetic fields," which was published in Scientific Reports in 2022 [2]. Within this chapter, several significant discoveries are discussed, such as the transformations of the fractional quantized Hall effect caused by tilt, resulting in a transition from one distinct filling factor ($\nu$) to another (specifically, from $\nu = 11/7$ to $\nu = 8/5$) as the tilt

angle increases. Additionally, the results highlight a remarkable size dependence within the tilt angle range, leading to the disappearance of the 4/3 and 7/5 states.

Chapter 4 delves into the fabrication of devices using graphene through two distinct methods: exfoliation from naturally occurring graphite and CVD techniques. Section 4.1 focuses on the device fabrication process involving exfoliation of 2-D materials. This section provides a comprehensive overview of exfoliation techniques, dry transfer methods, and the subsequent device fabrication procedures. On the other hand, Section 4.2 explores the growth of graphene on a catalytic substrate using the Low-Pressure Chemical Vapor Deposition (LPCVD) method. The intricacies of this growth process are discussed, highlighting the key steps and considerations involved in achieving high-quality graphene films on the chosen substrate.

Chapter 5 explores the impact of current annealing on the quality of graphene grown via CVD. The chapter incorporates textual content and figures derived from the article titled "Effects of long-time current annealing on the hysteresis in CVD graphene on $SiO_2$," published in MRS Advances in 2019. Its primary focus lies in investigating the influence of impurities on carrier transport within CVD-grown graphene. Furthermore, the chapter examines the hysteresis phenomena commonly observed in CVD-grown graphene devices and analyzes how long-term current annealing can affect both the hysteresis effect and the overall quality of the graphene material.

# 2 TWO-DIMENSIONAL ELECTRON GAS

A 2D electron gas (2DEG) is a system of electrons that are confined to move in two dimensions within a thin layer or interface. This system is typically formed at the interface between two materials with different electronic properties, such as a semiconductor and an insulator. In a 2DEG, the electrons can only move in a plane that is perpendicular to a certain direction and are tightly confined by a potential barrier. This confinement leads to quantization of electronic energy levels, resulting in a series of electronic states that are characterized by their energy, momentum, and spin. The phenomenon of quantum size effects, commonly referred to as size quantization, is observed in systems where electrons are confined to regions of comparable dimensions as their corresponding de Broglie wavelength. The size quantization arises due to the discrete energy levels that electrons can occupy in the confined space, which depend on the properties of the confining potential.

Consider the case where electrons are confined in the z-direction and are free to move in the x and y-directions, resulting in the creation of a 2DEG. In a 2DEG, the energies of electrons are quantized in the z-direction, leading to the formation of discrete electronic energy levels. Similarly, a 2D hole system can be formed by confining holes to a 2D plane. For example, an electron confined in a square well of width $a$ with an infinite potential energy along the z-direction results in a size quantized system. From fundamental quantum mechanics, it is known that the energy of such a system can be expressed as,

$$E_N = \frac{\pi^2 \hbar^2 N^2}{2m^* a^2} \tag{2.1}$$

where $N$ is the quantum number and $m^*$ is the effective mass of the electron. [1, 3]

The equation (2.1) is not applicable for a quantum well with finite depth and a nonrectangular shape. Therefore, in such a situation, a qualitative approximation can be given for the energy as,

$$E_N \sim \frac{\hbar^2}{m^* a^2} \tag{2.2}$$

The confinement is only in z-direction and the carriers are free to move in x and y-directions resulting a total energy that consist of discrete energy levels due to confinement and a continuous

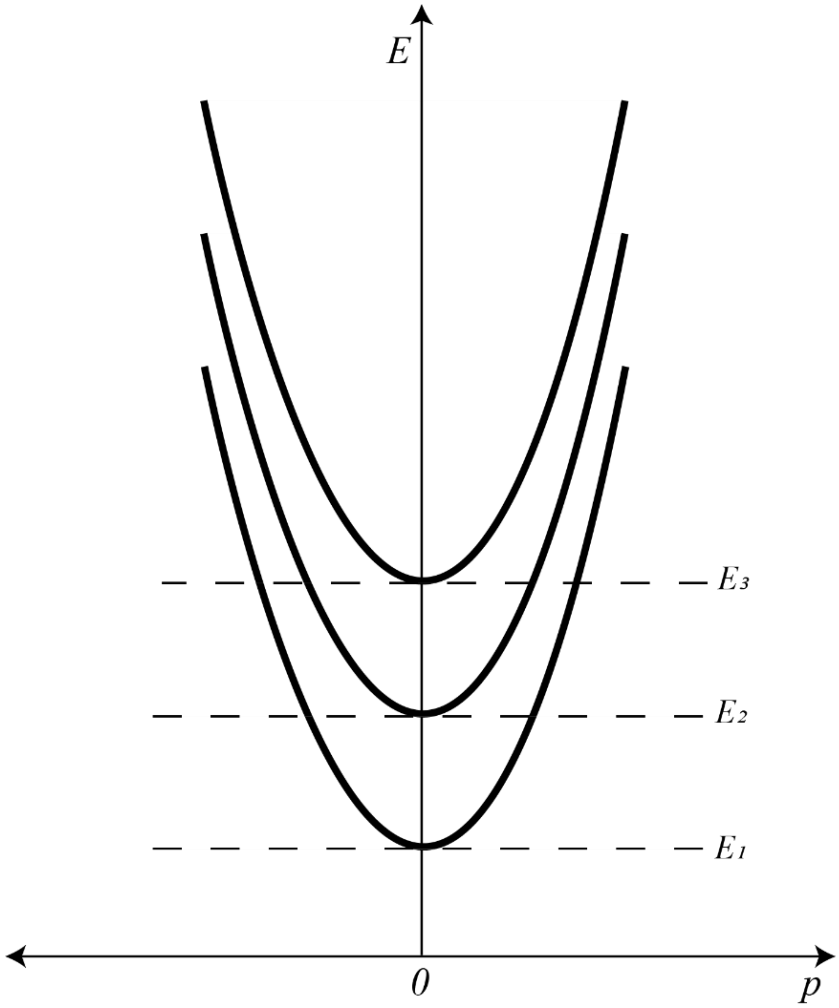


*Figure 2.1 Energy diagram of electrons in a 2DEG with respect to momentum (P) in 2D plane[1].*

component $(p_x^2 + p_y^2)/2m^*$due to motion of carriers in xy-plane. So, the total energy can be given as,

$$E = E_N + \frac{p_x^2 + p_y^2}{2m^*} \tag{2.3}$$

where x and y components of the momentum are given as $p_x$ and $p_y$ respectively. Since the momentum of the carriers can get any value from zero to infinity, the total energy of the carriers can get any value between $E_N$ and infinity as depicted in Figure 2.1[1].

## 2.1 Quantum effects in 2DEG

To observe any quantum effects in a 2D sample, the background thermal energy must be significantly lower than the energy separation between two consecutive energy levels.

$$E_{N+1} - E_N \gg k_B T \tag{2.4}$$

Here, $k_B$ is the Boltzmann constant and $T$ is the temperature of the system in Kelvin. If the background thermal energy is not significantly lower than the energy separation between two consecutive energy levels in a 2D sample, then the thermal fluctuations of the particles in the system will start to dominate and obscure any quantum effects that may be present.

This is because thermal energy can cause the particles in the system to randomly transition between different energy levels, which would effectively average out any quantum mechanical behavior that may be observed in the system. As a result, the system would appear to behave classically, rather than exhibiting the unique properties associated with quantum mechanics.

Therefore, in order to observe quantum effects in a 2D sample, it is necessary to cool the system down to a temperature that is sufficiently lower than the energy separation between consecutive energy levels, so that the particles are not subject to significant thermal fluctuations.

Another important factor for observing quantum effect is the transport lifetime ($\tau$), which is directly proportional to the carrier mobility μ.

$$\mu = \frac{e\tau}{m^*} \tag{2.5}$$

And the single-particle lifetime ($\tau_s$), which is inversely proportional to the broadening, $\Delta E$, of energy levels,

$$\tau_s = \frac{\hbar}{\Delta E} \tag{2.6}$$

The transport lifetime is extracted from the dc conductivity, while the single particle lifetime can be, for example, obtained by fitting the lineshape of the Shubnikov de Haas oscillations often observed in the magnetoresistance. The single particle lifetime is influenced by all scattering events, and it is taken to be a measure of carrier lifetime in a quantum state. The transport lifetime, on the other hand, is more sensitive to large-angle scattering. In a system characterized by mostly large-angle scattering, the two lifetimes approach each other. On the other hand, these lifetimes differ significantly in systems exhibiting mostly small-angle scattering. Since it is more difficult to measure $\tau_s$, one often just uses the $\tau$ as a proxy, since the dc conductivity is easily measured. To consider the system as having separate and distinct energy levels, the energy separation must be greater than $\Delta E$. Hence,

$$E_{N+1} - E_N \gg \frac{\hbar}{\tau_s} \tag{2.7}$$

Therefore, a higher $\tau_s$ is desired for the observation of quantum effects in the 2DEG. However, if $\tau_s$ is not available, one might roughly say that higher mobility is desired for the observation of quantum effects and quantum size effects in the 2DEG.

In summary, in order to observe quantum effects in thin films, having high surface quality is important for achieving specular reflection, which means that the angle of incidence

and angle of reflection are equal, and the momentum of the electrons is conserved during reflection. If the momentum is not conserved during reflection, the electrons will scatter, and the film will not have a uniform thickness. In order to observe quantum effects in thin films, certain conditions must be met, such as having a film thickness smaller than the de Broglie wavelength of the carriers, high carrier mobility, low temperature, and low carrier concentration. These conditions are necessary to ensure that the carriers exhibit level quantization. Among many ways that a 2DEG can be realized[3-5], Molecular Beam Epitaxy (MBE) growth of GaAs/AlGaAs heterostructure proved to be providing high-quality samples that are suitable for studying quantum effects[6].

## 2.2 Heterostructure 2DEG

A heterojunction is created when two materials with different band gaps come into contact. By carefully selecting semiconductors with a proper lattice match, heterostructures can achieve atomically smooth interfaces. Compared to silicon MOS structures or semimetallic thin films, heterostructures offer the potential to create devices of exceptionally high quality. The precise lattice matching allows for the formation of heterostructures with superior characteristics, making them ideal for applications that require enhanced performance and efficiency.

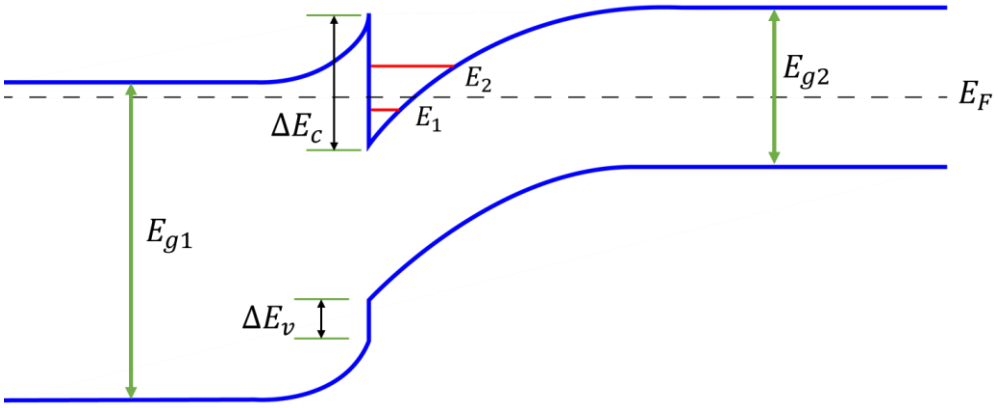


*Figure 2.2 An illustration depicting a typical band diagram of a single heterojunction between n- and p- type semiconductors.[1]*

Figure 2.2 shows the band diagram for a typical single heterojunction between n-type and p-type semiconductors. $E_{g1}$and $E_{g2}$ are the energy gap between the conduction and valence bands of material 1 and 2 respectively. The difference between the electron affinities of the materials in the junction is given by $\Delta E_c$ which is known as the conduction band offset. $\Delta E_v$ is known as the valance band offset which is given by $\Delta E_v = E_{g1} - E_{g2} - \Delta E_c$ [1]. To obtain a uniform Fermi level, electrons are moved from the wide band gapped semiconductor to the semiconductor with a smaller band gap. The band bending, resulting from the band offset between the two materials, ensures that these electrons accumulate specifically at the interface where the two layers meet. These electrons become confined within a triangular potential well that is formed at the interface of the two materials. Due to their limited ability to move, the trapped electrons can only freely travel along the interface. Hence, these localized electrons are commonly known as two-dimensional electron gases[6]. It is worth noting that depending on the dopants, a potential well can be designed to trap holes instead of electrons that would provide a two-dimensional hole gas[7].

In heterojunction systems, similar to other configurations, the presence of scattering poses a challenge for the formation of a high quality 2DEG. Various factors contribute to scattering in heterostructures, such as ionized impurities, phonons, and interface roughness, among others. However, there are effective strategies to address these scattering phenomena.

One important aspect is the careful engineering of smooth interfaces during the growth process, which helps to control and minimize interface scattering. Furthermore, at cryogenic temperatures below 4.2 K, the impact of phonon scatterings can be significantly reduced.

To tackle the scattering caused by ionized impurities, a technique called modulation doping or remote δ-doping is employed. This approach involves using a spacer layer to

effectively separate the impurities from the two-dimensional electron gas. By implementing this method, the adverse effects of impurities on the electron mobility can be mitigated, leading to improved performance of the 2DEG[8]. Typical band diagram of a modulation doped heterojunction that illustrates formation of 2DEG is shown in Figure 2.3.

Moreover, to enhance the separation between ionized impurities and the electron layer, it is possible to further widen the undoped region $d$ as depicted in Figure 2.3. This approach can indeed result in an increase in mobility. However, it is important to note that mobility will continue to rise with the increase in d only up to a certain threshold. Beyond this limit, widening the undoped region can lead to a decrease in carrier concentration. Therefore, while expanding the undoped region initially improves mobility, there exists an optimal point where further widening can have diminishing returns and negatively impact carrier concentration.

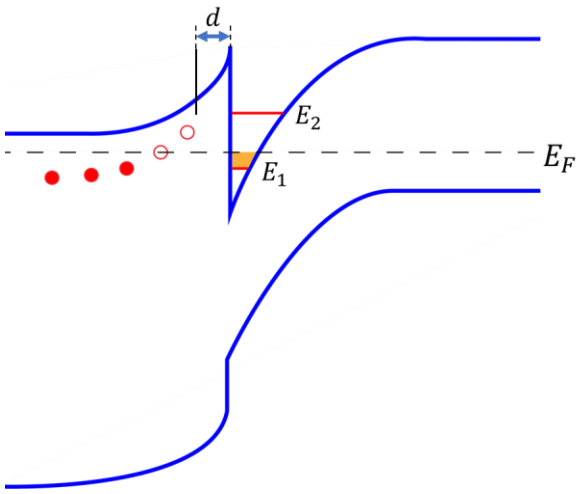


*Figure 2.3 Triangular quantum well in a heterojunction created by modulation doping. Ionized impurity and occupied electronic states are indicated in the wide bandgap semiconductor. Spacer layer is indicated as "d". Colored region inside the quantum well indicates formation of 2DEG.[1]*

For instance, the GaAs and AlGaAs materials exhibit an exceptionally sharp interface, thanks to their closely matched lattice constants. This remarkable interface quality greatly reduces lattice errors caused by crystal strain. In particular, GaAs/AlGaAs heterostructures are

known to yield remarkable two-dimensional electron systems (2DES) with mobilities reaching nearly $10^8 cm^2/Vs$ at cryogenic temperatures [9, 10]. Such high mobilities make GaAs/AlGaAs heterostructures an ideal choice for investigating and exploring quantum phenomena.

### 2.3 Energy of 2DEG in a magnetic field

The impact of a magnetic field on a two-dimensional electron gas (2DEG) can be examined by considering its components: one parallel to the plane of the 2DEG and the other perpendicular to it. Studies have demonstrated that the magnetic field component parallel to the plane does not qualitatively affect the energy spectrum of the 2DEG. However, it does alter both the energy associated with size quantization and the effective mass of motion perpendicular to the direction of the applied magnetic field[1]. On the other hand, the component of the magnetic field perpendicular to the 2DEG plane has a significant influence on the energy spectrum, leading to notable changes.

Let's imagine a scenario where the externally applied magnetic field is oriented perpendicular to the two-dimensional (2D) plane, and for the sake of simplicity, there is no magnetic field component within the plane considered in our analysis. In this particular situation, the applied magnetic field does not affect the motion of electrons along the z-axis. Consequently, there are no alterations to the energy levels associated with size quantization, as they continue to be governed by the potential of the quantum well. The movement of spin-less, non-interacting, massive electrons within the $xy$-plane in a vector potential $A = A_x = -yB$ can be mathematically expressed as follows:

$$-\frac{\hbar^2}{2m^*}\left[\left(-i\frac{\partial}{\partial x}-\frac{eB}{\hbar}\right)^2-\frac{\partial^2}{\partial y^2}\right].\phi = E_{\perp}.\phi \tag{2.8}$$

where, $B$ is the magnetic field considered in z-direction. If we assume that the wave function

takes the form of $\phi(x,y) = e^{ip_x x/\hbar}\chi(y)$, the resulting equation for $\chi$ will represent a harmonic oscillator,

$$-\frac{\hbar^2}{2m^*}\chi'' + \frac{m\omega_c^2(y-y_0)^2}{2}\chi = E_\perp \chi \tag{2.9}$$

The frequency of the oscillator will be equal to the cyclotron frequency $\omega_c = eB/m^*$ and center of the oscillator,

$$y_0 = -\left(\frac{1}{eB}\right) p_x \tag{2.10}$$

If the magnetic length corresponds to electrons cyclotron orbit is given by, $l_B = \sqrt{\hbar/eB}$, Equation (2.10) can be written as,

$$y_0 = -l_B^2\left(\frac{p_x}{\hbar}\right) \tag{2.11}$$

Total energy,

$$E = E_N + \hbar\omega_c\left(M + \frac{1}{2}\right), \qquad M = 0, 1, 2, \ldots \tag{2.12}$$

The energy levels, $E_{M=}\ \hbar\omega_c(M + 1/2)$ are called Landau Levels (LL), which are separated by $\hbar\omega_c$ from each other. Consequently, in an ideal 2DEG exposed to a magnetic field perpendicular to the 2D plane, the energy spectrum is composed of size quantized energy levels and LL separated by cyclotron gaps ($\hbar\omega_c$). If spin is added, these LL are further split by the Zeeman energy ($g\mu_B B$), which accounts for the interaction between the electron spins and the magnetic field. Notably, in this instance, the energy spectrum of the carriers is discrete, exhibiting distinct energy levels with quantized values. Then the total energy can be given by,

$$E = E_N + \hbar\omega_c\left(M + \frac{1}{2}\right) \pm \frac{1}{2}\ g\mu_B B, \qquad M = 0, 1, 2, \ldots \tag{2.13}$$

Here, the g-factor of the electron is given by $g$ and $\mu_B$ represent Bohr magneton. Since the spin-down state is higher in energy than the spin-up state, the positive (+) sign in Equation (2.13)

corresponds to the spin-down state of the electron, while the negative sign (-) corresponds to the spin-up state.

In the absence of a magnetic field, The Fermi energy of the system can be given as,

$$E_F = \frac{\hbar^2 k_F^2}{2m^*} \tag{2.14}$$

where $k_F$ is the fermi wave vector. At cryogenic temperatures, the energy gap between the size-quantized energy levels is much larger compared to Fermi energy. As a result, the lowest energy level ($N$=1) among the size-quantized energy levels becomes occupied and the Equation (2.13) will become,

$$E = E_1 + \hbar\omega_c \left(M + \frac{1}{2}\right) \pm \frac{1}{2}\, g\mu_B B, \tag{2.16}$$

The energy values rely solely on the quantum number $M$ and the spin direction, resulting in a high degree of degeneracy. This degeneracy is primarily determined by the dimensions of the sample's $xy$-plane. The LL degeneracy per unit area can be given as $n_L = 1/2\pi l_B^2$. The density of state for a LL, $n_{DOS}$ is given by,

$$n_{DOS} = \frac{eB}{h} \tag{2.17}$$

The degeneracy per unit area can also be represented as $n_L = B/\phi$, where $\phi = h/e$ is magnetic flux quanta. Thus, each Landau level can accommodate as many magnetic flux quanta ($\phi$) as the magnetic field allows to penetrate the sample. The filling factor ($\upsilon$) is defined as the total number of LL filled by the carriers in the system. Which can be expressed as,

$$\nu = \frac{n_e}{n_{DOS}} = \frac{n_e h}{eB} \tag{2.18}$$

where, $n_e$ is the electron density. To determine the density of states per LL for a degenerate electron system, Equation (2.17) needs to be multiplied by the corresponding degeneracy factor.

In Figure 2.4, the continuum of energy states in a 2DEG at zero magnetic flux is depicted (a), illustrating the separation into Landau levels (b) and subsequent subdivision into sub-bands (c) because of the Zeeman energy in the presence of a magnetic field. Furthermore, Figure 2.4 (b) and (c) demonstrate that as the magnetic field strength increases, the separation between energy levels becomes more pronounced. This increased separation can cause certain levels to surpass the Fermi level, effectively making them inaccessible to electrons at temperatures close to absolute zero.

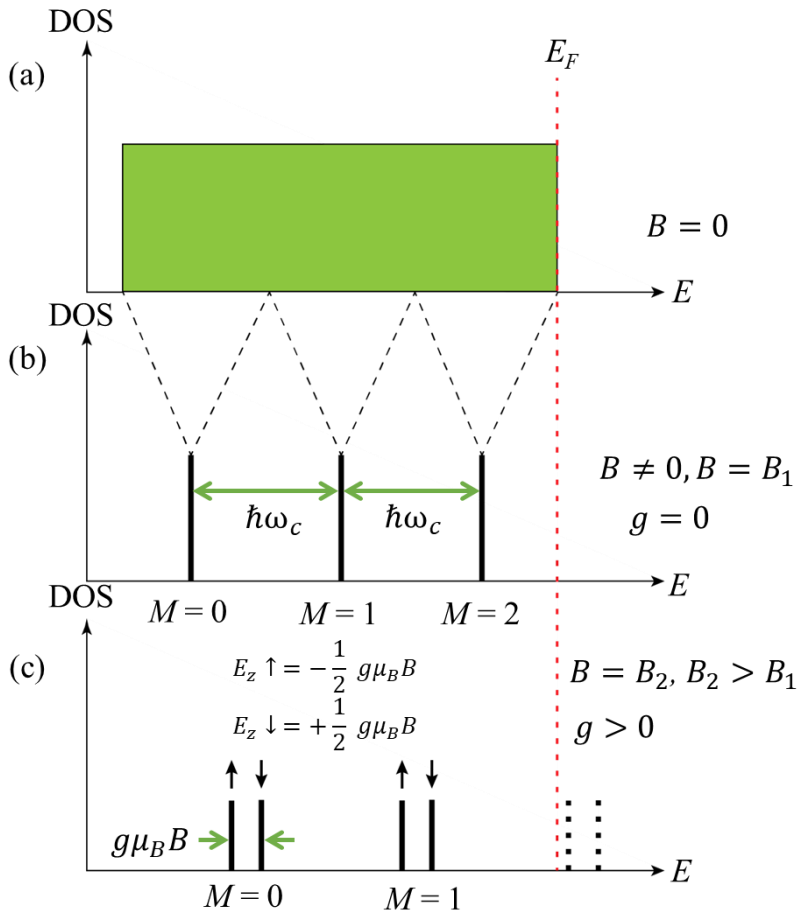


*Figure 2.4 Landau level diagram for a 2DEG at various conditions (a) Landau level diagram illustrating the continuum of states in a 2DEG at zero magnetic field (B=0). (b) Introduction of a nonzero magnetic field leads to the quantization of the continuum of states into Landau levels. The depicted level separation does not account for the spin degree of freedom. (c) Landau levels are further split into two sub-bands due to the inclusion of spin ($E_z$ = Zeeman energy). Increasing the magnetic field enhances the separation between energy levels, causing some levels to exceed the Fermi level, rendering them inaccessible to electrons.*

## 2.4 Carrier transport in 2DEG

The classical Drude model, developed by Paul Drude, provides a framework for understanding how electrons move in metals[11-13]. This model assumes that electrons can be treated as separate entities, disregarding their Coulomb interactions with each other (independent electron approximation). It also assumes that electron-ion interactions can be ignored (free electron approximation). In the absence of external electric or magnetic fields, electrons move in a straight line until they collide. These collisions, treated as instantaneous and unrelated events, cause sudden changes in electron velocities. The mean free time ($\tau$) represents the average time between collisions, while the mean free path represents the maximum distance an electron can travel without colliding. Collisions lead to the establishment of thermal equilibrium between the electrons and their surroundings.

The relationship between resistivity ($\rho$), electric field ($E$), and current density ($j$) is given by the equation $E = \rho j$. The current density ($j$) can be expressed as $j = -nev_{av}$, where $n$ represents the electron density and $v_{av}$ denotes the average electron velocity. The average velocity ($v_{av}$) is determined by $v_{av} = -eE\tau/m,$ considering the electron charge ($e$) and mass ($m$) and it opposes the direction of the applied electric field. If the material exhibits a conductivity of $\sigma_0$, the relationship $j = \sigma_0 E$ holds. The conductivity $\sigma_0$ can be calculated as $\sigma_0 = ne^2\tau$/m, considering factors such as electron density, charge, mean free time, and mass.

If we consider a magnetic field $\vec{B} = (0, 0, B_z)$, and an electric field $\vec{E} = (E_x, 0, 0)$, an equation of motion for an electron that is moving with a velocity $\vec{v} = (\dot{x}, \dot{y}, 0)$ can be given as,

$$m\dot{\vec{v}} = -e\vec{E} - e\vec{v} \times \vec{B} - \frac{m\vec{v}}{\tau} \tag{2.19}$$

The term $m\vec{v}/\tau$ here accounts for the linear friction caused by the scattering due to the disorder and impurities. For the steady state (i.e., $\dot{\vec{v}} = 0$), the Equation 2.19 can be written as,

$$\vec{v} = -\frac{e\tau}{m}(\vec{E} + \vec{v} \times \vec{B}) \tag{2.20}$$

which can be also written as,

$$\dot{x} = -\frac{e\tau}{m}E_x - \omega_c \tau \dot{y} \tag{2.21}$$

$$\dot{y} = -\frac{e\tau}{m}E_y + \omega_c \tau \dot{x} \tag{2.22}$$

where cyclotron frequency $\omega_c = eB/m$. By solving the equations (2.21) and (2.22) for $\dot{x}$ and $\dot{y}$,

$$\dot{x} = \frac{1}{1 + \omega_c^2 \tau^2}\left(-\frac{e\tau}{m}E_x + \frac{e\omega_c \tau^2}{m}E_y\right) \tag{2.23}$$

$$\dot{y} = \frac{1}{1 + \omega_c^2 \tau^2}\left(-\frac{e\tau}{m}E_y - \frac{e\omega_c \tau^2}{m}E_x\right) \tag{2.24}$$

Since $j = -nev = \sigma E$, the conductivity tensor can be written as,

$$\sigma = \frac{\sigma_0}{1 + \omega_c^2 \tau^2}\begin{pmatrix} 1 & -\omega_c \tau \\ \omega_c \tau & 1 \end{pmatrix} \tag{2.25}$$

where the conductivity at $B = 0$ is $\sigma_0 = ne^2\tau/m$. The resistivity, denoted by $\rho$, is the reciprocal of the conductivity. From the Drude model we get,

$$\rho = \frac{1}{\sigma_0}\begin{pmatrix} 1 & \omega_c \tau \\ -\omega_c \tau & 1 \end{pmatrix} \tag{2.26}$$

The resistivities that are relevant to transport, in relation to conductivity, can be expressed as,

$$\rho_{xx} = \frac{\sigma_{xx}}{\sigma_{xx}^2 + \sigma_{xy}^2} \tag{2.27}$$

$$\rho_{xy} = \frac{\sigma_{xy}}{\sigma_{xx}^2 + \sigma_{xy}^2} \tag{2.28}$$

When an electric field is applied in the $x$-direction, it induces a current density $j_x$. The motion of this current is affected by the presence of a perpendicular magnetic field, resulting in a deflection due to the Lorentz force. As a result, the current bends towards the $y$-direction. This bending leads to a buildup of charge along the edges of the device, creating an associated electric field

$E_y$. This process continues until the Lorentz force exerted on the charge carriers is balanced by the electric force[11]. The induced electric field $E_y$ gives rise to the Hall voltage, $V_H$. At equilibrium, when the $y$-direction current density $j_y$ is zero, an important parameter known as the Hall coefficient $R_H$ can be defined. The Hall coefficient $R_H$ is expressed as,

$$R_H = \frac{E_y}{Bj_x} = -\frac{1}{n_e e} \tag{2.29}$$

The results strongly indicate that the $R_H$ is solely dependent on the carrier density and not on any material-specific parameters. Moreover, the sign of the Hall coefficient can be used to determine the type of carriers present ("−" sign in Equation (2.29) is due to the fact the carriers are electrons). The Hall effect was discovered by E.H. Hall in 1879.

## 2.5 Integer Quantum Hall Effect

The journey to understand the quantum Hall effect began in 1975 when Tsuneya Ando, Yukio Matsumoto, and Yasutada Uemura predicted the phenomenon of integer quantization in Hall conductivity[14]. Building on this theoretical foundation, Jun-ichi Wakabayashi and Shinji Kawaji conducted experimental work in 1978, observing plateaus in the Hall effect[15]. It occurs when a magnetic field induces charge accumulation through the Lorentz force in an electronic system. Surprisingly, at low temperatures and high magnetic fields, the Hall resistance displayed unexpected plateaus that contradicted the predictions of the Drude model. In 1980, Klaus von Klitzing made a significant contribution by conducting meticulous measurements on silicon-based MOSFETs at high magnetic fields, which revealed the precise quantization of Hall resistance on these plateaus [16], which later became known as the integer quantum Hall effect (IQHE) [17]. Remarkably, the resistance exhibited on these plateaus depended solely on the values of Planck's constant and the elementary charge of the carrier, independent of the geometry

of the Hall bar. This experiment involved monitoring transverse and longitudinal voltages as a function of gate voltage while maintaining a constant magnetic field strength of 18 Tesla, as shown in Figure 2.5. The intensity of the magnetic field ensured well-separated Landau levels within the system, enabling an accurate determination of the charge carrier concentration.

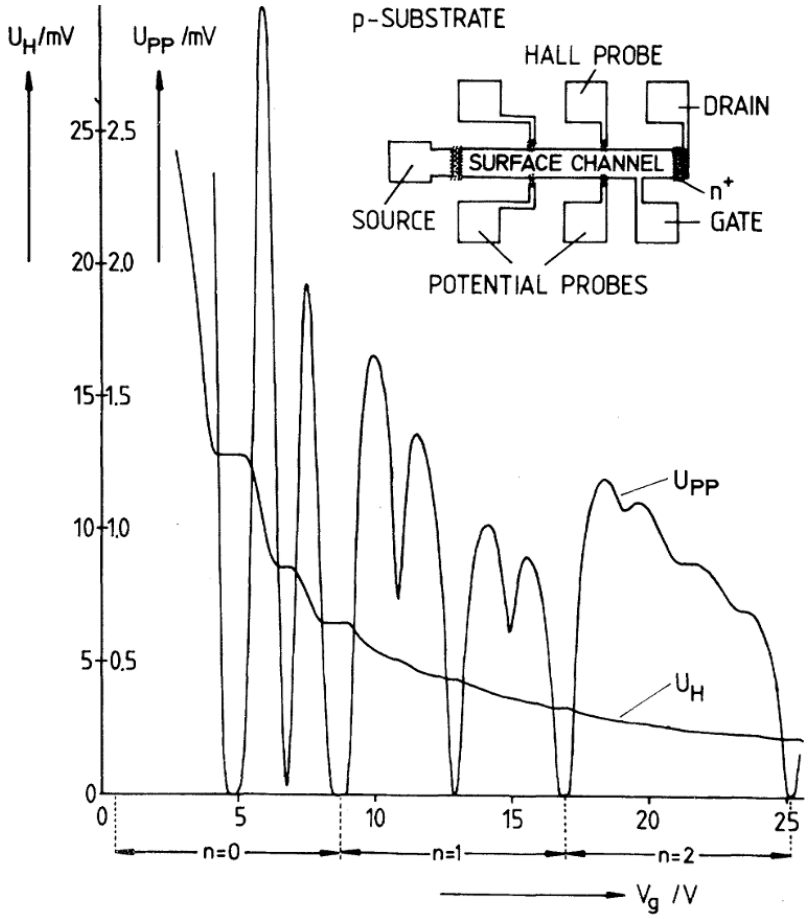


*Figure 2.5 Integer Quantum Hall Effect observed in a silicon-MOSFET. Hall voltage ($U_H$) and the longitudinal voltage ($U_{pp}$) are plotted against the applied gate voltage. The temperature is 1.5K and the fixed magnetic field is 18 T. The top view of the sample is depicted in the inset. Reproduced from von Klitzing et al. (1980)[16].*

In the absence of an external magnetic field, the system exhibits a constant density of states with respect to energy. However, when a non-zero magnetic field is applied along the z-direction, the energy continuum starts to separate into Landau levels. Theoretically, Landau levels are idealized as perfectly sharp energy levels in a magnetic field. In practical scenarios,

however, Landau levels can be broadened due to various factors, including disorder, impurities, and electron-electron interactions, creating a broadening known as Landau level broadening. This broadening can lead to the formation of localized states within the material. As a result, a weak magnetic field fails to completely isolate the Landau levels, resulting in a narrower separation between adjacent Landau levels compared to the width of an individual Landau level. As the magnetic field strength increases, the separation between Landau levels expands, reducing the overlap between them. Notably, the magnetic field variation causes the Landau levels to shift relative to the Fermi level.

Consider a scenario where the Fermi energy $E_F$ lies between two adjacent Landau levels in a localized state, and all states below $E_F$ are fully occupied by electrons. According to the Pauli exclusion principle, electrons within these states are prohibited from scattering into other available states. Consequently, all scattering events are suppressed, leading to dissipationless transport and a resistance that goes to zero.

When a 2DEG is in a strong magnetic field we can consider $\omega_c \tau \gg 1$, then,

$$\sigma_{xx} = \frac{e^2 n_e}{m\omega_c^2 \tau} \tag{2.30}$$

and,

$$\sigma_{xy} = \frac{e^2 n_e}{m\omega_c^2} \tag{2.31}$$

where $\sigma_{xx}$ denotes diagonal conductivity and $\sigma_{xy}$ represent the Hall conductivity. It can be shown that by considering the Equations (2.17, 2.18, and 2.31), the Hall conductivity can be written as,

$$\sigma_{xy} = \left(\frac{e^2}{\hbar}\right)\nu, \qquad \nu = 1,2,3,\ldots \tag{2.32}$$

The Equation (2.32) indicates that the Hall conductivity takes integer multiples of $e^2/\hbar$. For instance, when the Fermi energy lies in between the N and N+1 Landau levels, there will be a plateau in the Hall resistance, and the diagonal resistance will be zero. Figure 2.6. depict such features observed in Hall resistance and diagonal resistance of a GaAs/AlGaAs 2DEG Hall bar device[18].

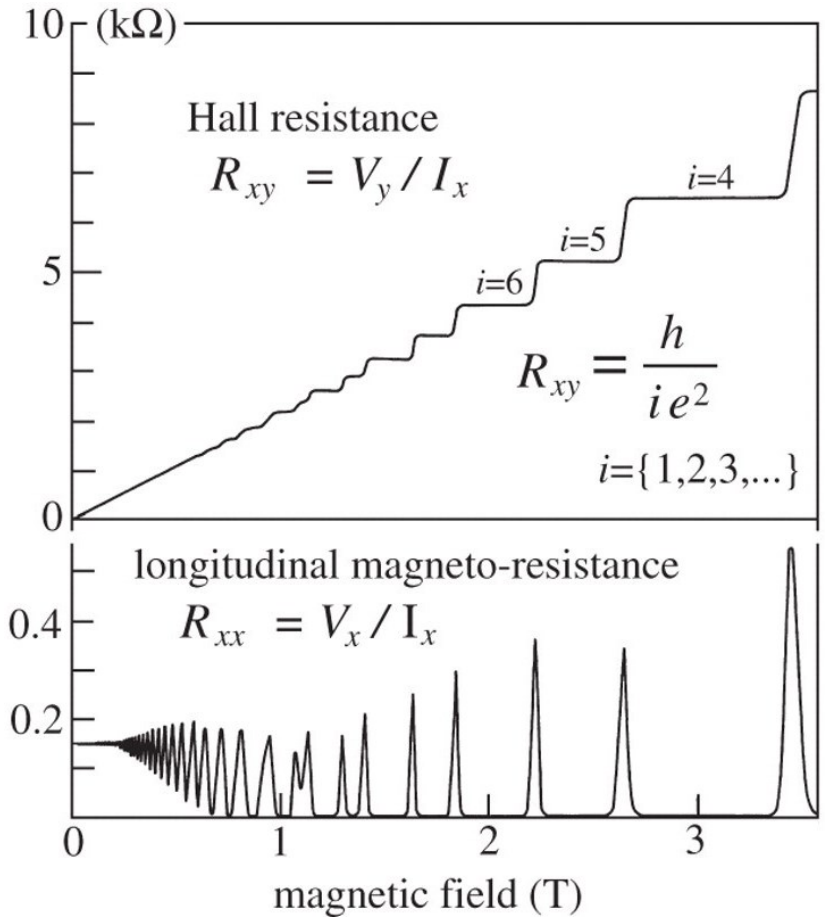


*Figure 2.6 Hall resistance and diagonal resistance curves plotted against the magnetic field is depicted in top and bottom panels respectively. Reproduced from Weis et al. (2011)[18].*

The phenomenon of zero-resistance and Hall plateaus in the quantum Hall effect can be understood through two theoretical models: the localization theory and the edge state model. These models provide insights into the behavior of electrons in a 2DEG subjected to a strong magnetic field and low temperatures.

In the localization theory, the electron states in the 2DEG can be classified as localized or extended. At low temperatures, the localized states do not contribute to the current flow, while the extended states near the unperturbed Landau levels can carry current. By adjusting the electron density or the magnetic field strength, the position of the Fermi level relative to the LLs can be shifted. When the Fermi level lies within a localized state, the occupation of the extended states remains unchanged, resulting in a constant Hall resistance, which gives rise to a Hall plateau. Simultaneously, the longitudinal resistance vanishes because only localized states are in proximity to the Fermi level. As the Fermi level crosses to the next LL, dissipation occurs, and the Hall resistance transitions to the next plateau. Thus, the appearance of the QHE can be understood as a series of localization-delocalization transitions as the Fermi energy moves across the density of states[19].

On the other hand, the edge state model explains the QHE by considering the effects of the confining potential near the sample boundaries. The LLs experience an upward bending due to the confining potential, leading to the formation of extended states near the Fermi energy along the edges of the sample[19]. When the magnetic field is strong enough to suppress backscattering of electrons over a distance larger than their cyclotron orbits, a dissipation-less current flows along the edges. This flow of current along the edges is responsible for the observation of the QHE.

### *2.5.1 Dual simultaneous ordinary and quantized Hall effects in Mani's anti-Hall bar within a Hall bar geometry*

In 1993, Mani invented a groundbreaking approach to measure two distinct boundaries within a single sample by utilizing dual currents in a unique geometry that incorporates an anti-

Hall bar within a Hall bar (see Figure 2.7)[20-22]. They conducted a comprehensive study on both the ordinary and quantized Hall effects [23-29].

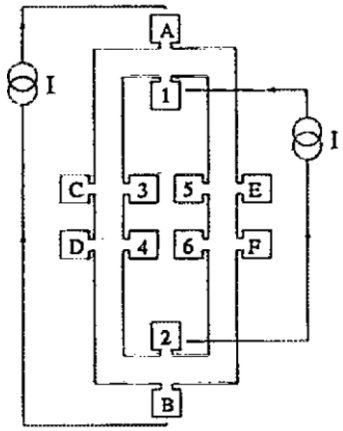


*Figure 2.7 Illustration of anti-Hall bar withing a Hall bar with dual current injection. Two boundary currents injected into the specimen simultaneously result in two Hall resistances. The first resistance,* $V_{D,F} / I_{A,B}$ *, is observed at the exterior boundary, while the second resistance,* $V_{4,6} / I_{1,2}$ *, is measured at the interior boundary. Reproduced from Mani et al., (1994)[27].*

Figure 2.7 illustrates the dual current injection a doubly connected sample, which gives rise to two simultaneous and independent Hall resistances (also see Figure 2.8). Mani et al. shows that the Hall effect observed on each boundary exclusively reflects the current injected through that specific boundary. Which means altering the current flowing through one boundary does not impact the Hall resistance observed at the other boundary. They also demonstrated the occurrence of dual ordinary and quantized Hall effects when dual injected currents are present, even when the total current cancels out in both branches of the doubly connected structure. These findings highlight the possibility of observing a classical Hall effect even in the absence of a net current [27].

Mani et al. conducted further investigations into the dual ordinary and quantized Hall effects in specimens with striplike, bimodal electron density distributions within the 2DEG device by employing various partial top gates in different regions of an anti-Hall bar within a Hall bar device.

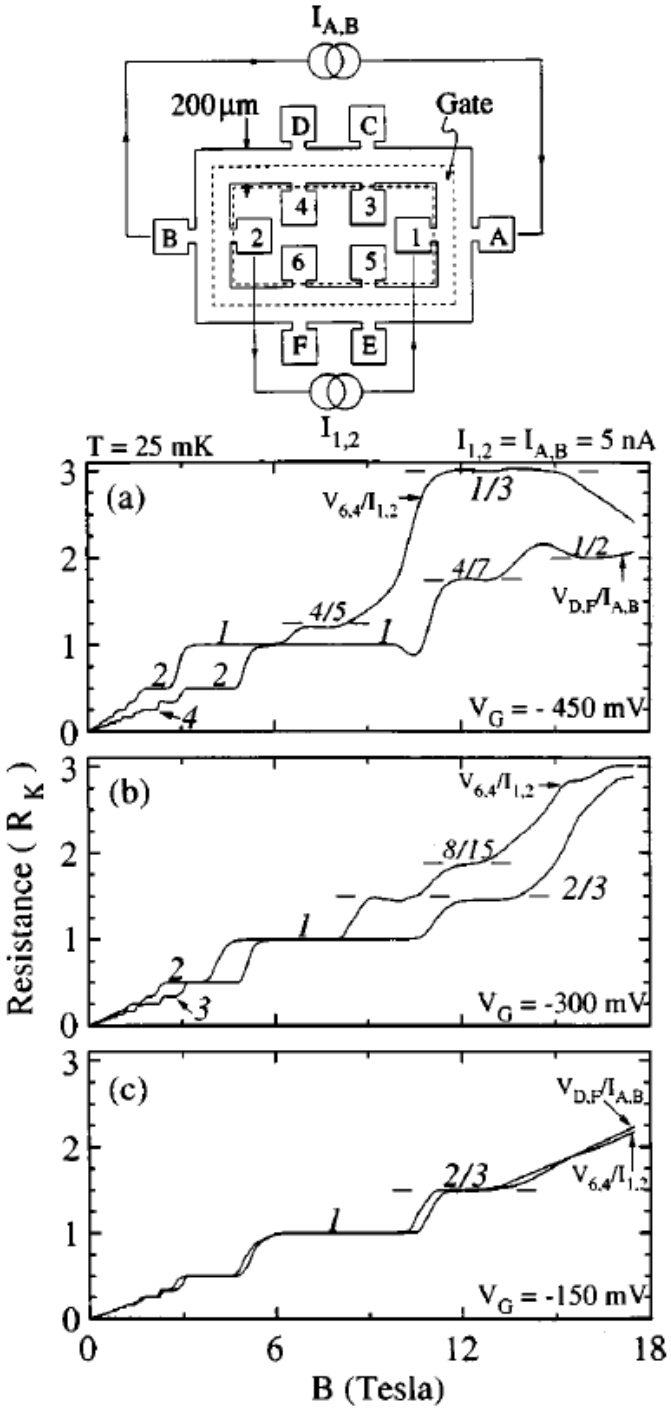


*Figure 2.8 Dual ordinary and quantized Hall effects in doubly connected and partially top gated GaAs/AlGaAs heterostructure device. The top panel shows an illustration of the anti-Hall bar withing a Hall bar device with the dual supply currents and a top gate that covers the anti-Hall bar section of the device (area of top gate is indicated by the dotted lines). In panels (a-c) show the Hall resistances measured from inner ($V_{6,4}$ / $I_{1,4}$) and outer ($V_{D,F}$ / $I_{A,B}$) boundaries in units of the Klitzing constant $R_K$ (ordinate). The gate voltage $V_G$ was varied from -150 mV in panel (c) to -450 mV in panel (a). Reproduced from Mani et. al., (1997) [30].*

They showed that the Hall effect at a specific set of contacts can exhibit significant variations based on the off-diagonal resistivity of the material connecting the source and drain[30]. In Figure 2.8, they presented Hall resistance measurements on an anti-Hall bar within a Hall bar device, where a partial top gate was utilized to cover only the anti-Hall bar region (inner boundary) of the device. The top panel of Figure 2.8 illustrate the sample connections and geometry. In Figure 2.8 (c), Hall resistance data is presented, which was collected under nearly homogeneous conditions with $V_G = -150$ mV. The inner and outer Hall resistance curves coincide, spanning the same range of magnetic fields.

A further reduction in the gate potential leads, however, to interior depletion and an increase in the slope of the inner Hall effect curve (as shown in Figure 2.8 1(b) and 1(a)), while the slope of the outer Hall curve remains unchanged. At a gate potential of -450 mV, there is a significant difference in the slopes of the inner and outer Hall curves, with nearly a twofold contrast showing two distinct quantum Hall effects within the specimen simultaneously [30].

## 2.6 Fractional Quantum Hall Effect

The fractional quantum Hall effect (FQHE) is a remarkable phenomenon that occurs in two-dimensional electron systems subjected to a strong magnetic field and low temperatures. It was first discovered experimentally by Tsui, Stormer, and Gossard in 1982[31](see Figure 2.9). Tsui et al., observed a plateau in the Hall resistance at $\nu = 1/3$ and a corresponding minimum in the diagonal resistance. Observation of plateaus in the Hall resistance at fractional values of the fundamental quantum of conductance ($e^2/\hbar$) is taken to indicate the presence of fractional charges in the 2DEG. The fractional charge arises due to the strong interactions among the electrons, leading to the breakdown of the concept of individual electrons and the emergence of collective behavior.

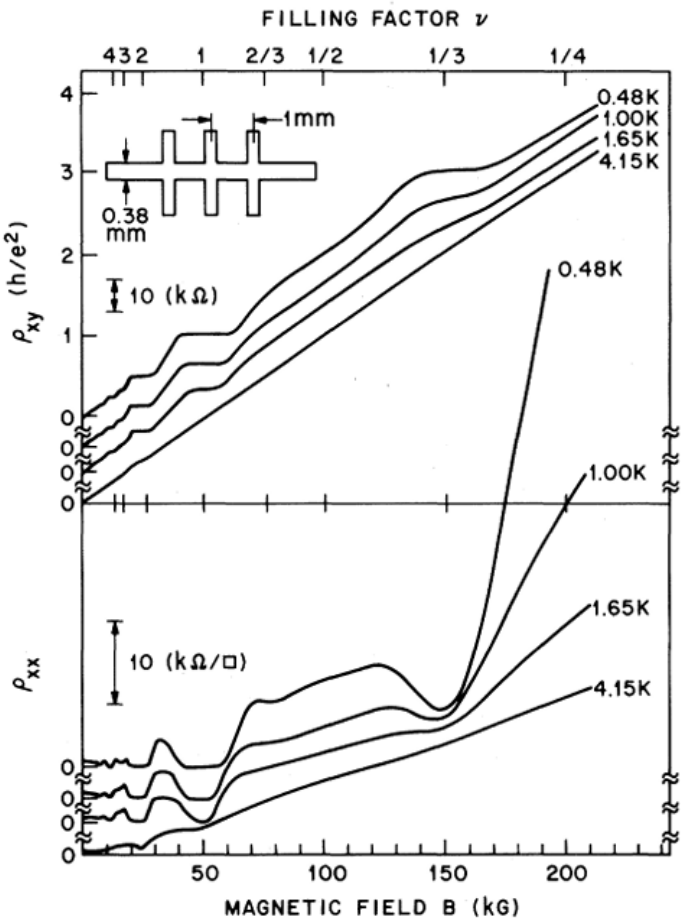


*Figure 2.9 First observation of a platau in Hall resistance and minima in the logitudinal resistance corresponds to a fractional filling factor ν =1/3. Measurements were from a GaAs/AlGaAs sample with* $n_e = 1.23 \times 10^{11}\ cm^{-2}$ , $\mu = 90000\ cm^2/Vs$ *[31].*

One of the pioneering theoretical models in the field was formulated by Robert Laughlin, who introduced a wave function known as the Laughlin wave function. Laughlin's model describes the FQHE states as incompressible quantum fluids, where the electrons form a correlated state exhibiting fractional charges. The wave function represents a many-body state that satisfies a set of unique mathematical properties and accounts for the observed fractional charges and their quantization. Laughlin's wave function successfully explains the prominent FQHE fractions observed experimentally, such as $\nu = 1/3$[32]. Horst Störmer, Daniel Tsui, and

Robert Laughlin were awarded the Nobel Prize in Physics in 1998 for their significant contributions to understanding the FQHE.

Another pioneering theoretical framework in understanding the FQHE is the composite fermion (CF) theory, proposed by Jainendra K. Jain[33]. This theory introduces the concept of composite fermions, which arise from the binding of electrons with an even number of quantized vortices of the background magnetic field. The composite fermions effectively experience a reduced magnetic field due to the presence of vortices, leading to the formation of new energy levels. The CF theory successfully explains the observed FQHE fractions as the integer quantum Hall effect of composite fermions and explains some sequences of states observed at fractional fillings.

At the heart of Jain's Composite Fermion theory is the concept of attaching an even number of quantized vortices to each electron, creating composite fermions that behave as if they were subjected to an effective magnetic field. This effective magnetic field is determined by the difference between the external magnetic field and the average magnetic field due to the attached vortices. By considering composite fermions as weakly interacting, Jain's theory provides a means to describe their behavior within a non-interacting electron picture.

According to the theory, the relationship between the filling factors of FQHE and the corresponding integer quantum Hall effect (IQHE) states through the formula $\nu = p/(2ps \pm 1)$, where $\nu$ represents the filling factor, $p$ is an integer, and $s$ denotes the number of attached flux quanta per composite fermion. This prediction accurately accounts for the observed fractional filling factors in various FQHE states.

For instance, let's consider the case where one electron is attached to two flux quanta, forming a composite fermion. In this scenario, the electron filling factor $\nu = 1/3$ corresponds to

the composite fermion filling factor $\nu^*_{CF} = 1$, as depicted in Figure 2.10. Similarly, when $\nu = 2/5$, there will be five flux quanta for every two electrons in the system. If we consider the system as composite fermions, resulting in a composite fermion filling factor $\nu^*_{CF} = 2$ (as shown in Figure 2.10).

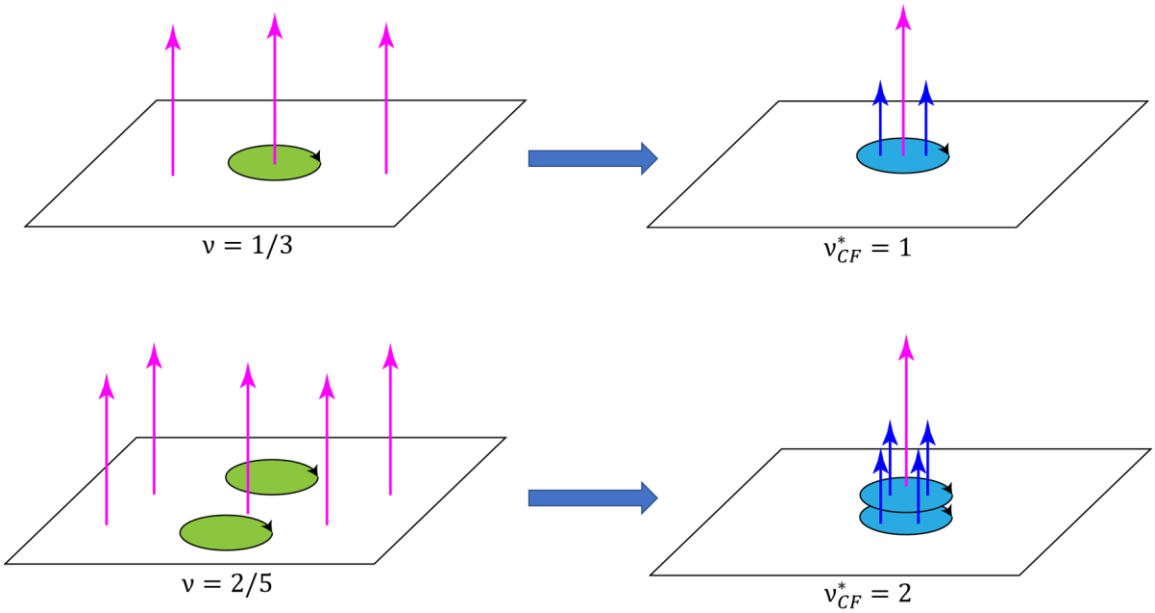


*Figure 2.10 Illustration of the relation between the electron filling factor ν and composite fermion filling factor $\nu^*_{CF}$. The top panel indicates that having three flux quanta per electron is equivalent to having one flux quanta per CF. Bottom panel indicates that five flux quanta per two electrons equal to having one flux quanta per two CF.*

The Hall resistance curve, including the Fractional Quantum Hall Effect (FQHE), exhibits intriguing fractal properties. Mani et al. demonstrated these properties through a method involving iterative transformations applied to the axes of Hall resistance and magnetic field. By constructing a template based on a fundamental Hall curve at filling factor $\nu = 1$, this technique enables the generation of diverse non-Jain sequences within the Hall resistance curve (see Figure 2.11). This novel approach not only reveals the fractal nature of the curve but also offers a convenient means to explore and comprehend the emergence of various non-Jain sequences within the realm of FQHE phenomena [34].

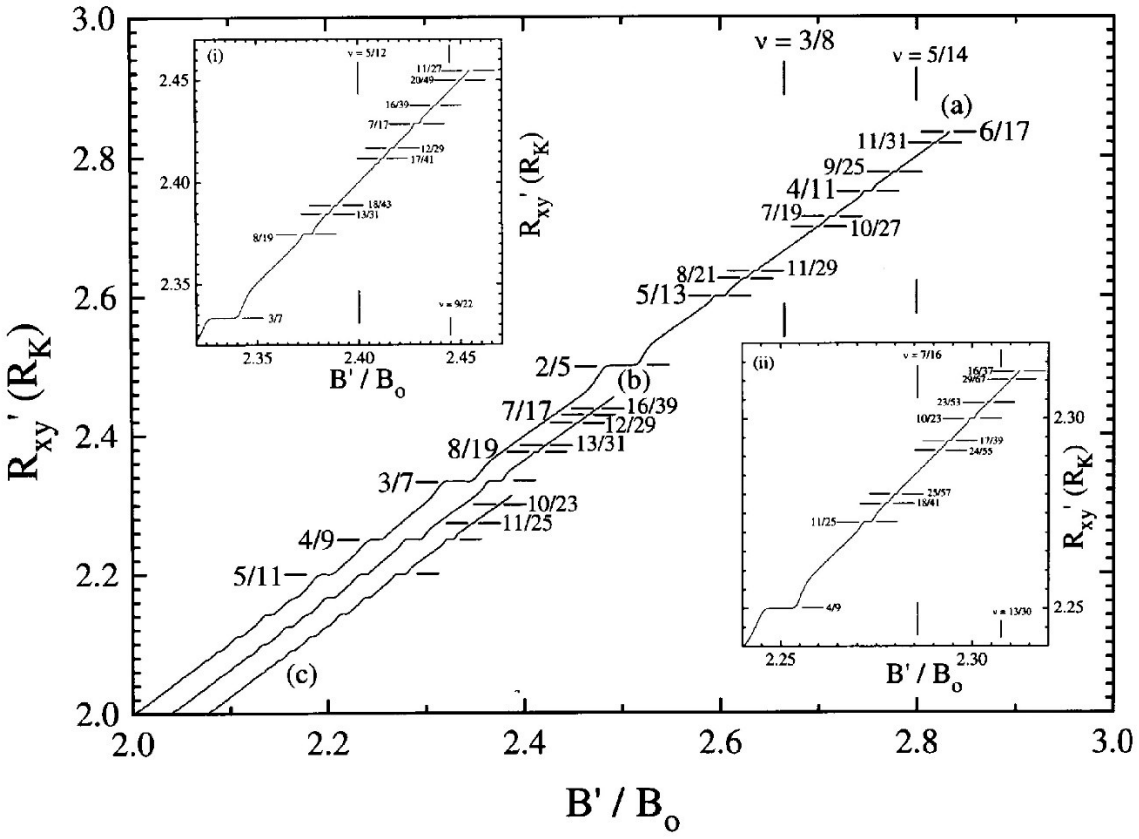


*Figure 2.11 A second-generation fractal reconstruction of an elementary FQHE curve to ν = 1/3 by the transformations $B'/B_0 = [8/3 \pm 1/(3(3\ B_0/B \pm 1))]$ and $R_{xy}'/R_K = [8/3 \pm 1/(3(3\ R_K/R_{xy} \pm 1))]$, respectively. Here, the '+' branch spans the range 3/8 > ν > 6/17, and the '1/3' FQHE is mapped onto the '6/17' FQHE in curve (a). In addition, the ν = 1/2 neighborhood is mapped onto the ν = 5/14 neighborhood. In the '-' branch, the '1' IQHE is transformed into the '2/5' FQHE in this curve. (b) The elementary FQHE curve has been rescaled by the transformations $B'/B_0 = [12/5 \pm 1/ (5(5\ B_0/B \pm 2))]$ and $R_{xy}'/R_K = [12/5 \pm 1/ (5(5\ R_K/R_{xy} \pm 2))]$, respectively. This produces additional FQHE's in the region 3/7 > ν > 2/5, which is shown in expanded scale in inset (i). (c) The elementary FQHE curve has been rescaled by the transformations $B'/B_0 = [16/7 \pm 1/ (7(7\ B_0/B \pm 3))]$ and $R_{xy}'/R_K = [16/7 \pm 1/ (7(7\ R_K/R_{xy} \pm 3))]$, respectively. This produces additional FQHE's in the region 4/9 > ν > 3/7, which is shown in expanded scale in inset (ii). Note that curves (a), (b), and (c) have been offset along the abscissa. Reproduced from Mani et. al., (1996)[34].*

# 3 FRACTIONAL QUANTUM HALL EFFECT IN A TILTED MAGNETIC FIELD

Two-dimensional electron systems under high transverse magnetic fields can display a fascinating phenomenon called the Fractional Quantum Hall Effect (FQHE). This effect is characterized by incompressible, correlated electronic states that emerge in the vicinity of specific odd and even denominator rational fractional filling factors, $\nu = (p/q)$ of the Landau levels [35-37]. These correlated electronic states exhibit a quantized Hall conductance that is a fraction of the conductance quantum, and the effect has been observed experimentally in various materials, including GaAs/AlGaAs heterostructures[38, 39] and graphene[40-42].

The GaAs/AlGaAs 2D electron system is characterized by a double degeneracy of Landau levels due to electron-spin. However, this degeneracy is removed by a small Zeeman spin splitting, $g\mu_B B$, which is comparable to the correlation energy. The relative change of the Zeeman splitting with respect to the correlation energy can lead to a re-ordering of the many body ground states at a constant filling factor. Specifically, the re-ordering can cause a transition between spin polarized, partially polarized, and unpolarized many body ground states[43-49].

Halperin proposed that a spin-unpolarized FQHE ground state could have a lower energy than a spin polarized ground state for a system that exhibits a small spin splitting, at filling fractions such as ν = 2/5[43]. As a result, efforts were made to find induced transitions between unpolarized and polarized ground states at a constant filling factor by manipulating the Zeeman energy. Eisenstein et al. reported experimental observations of a split in the minima at a filling factor of ν = 8/5 into two smaller minima at an angle of 30° during a tilted field measurement, as shown in Figure 3.1 (a). Subsequent investigations, including an activation energy study, revealed a sharp change in the angular dependence of the activation energy, as depicted in Figure

3.1 (b). This suggests a transition from a spin-unpolarized state to a spin-polarized state with an increased angle[45].

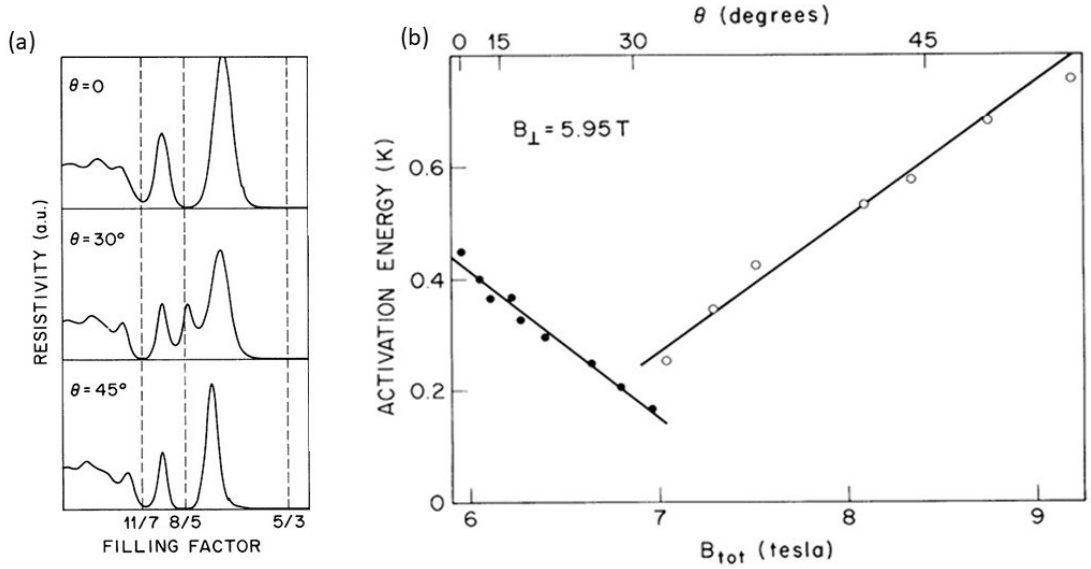


*Figure 3.1(a) Enlarged view of resistivity vs filling factor near ν = 8/5 at 30 mK temperature, (b) activation energy for ν = 8/5 vs total magnetic field. The solid and open circles depict low, and high field components of activation energies. The difference in the symbols is only relevant in the region near 30° where a doublet is formed. Reproduced from Eisenstein et al.,(1989)[45].*

Clark et al., reported their experimental findings on a fully spin-polarized 5/3 state that exhibits a persistent minimum when tilted, and a transition at ν = 4/3 indicating a spin-related transition from an unpolarized to a partially polarized state[46]. They have observed strong 5/3 and 4/3 minima and weak 8/5 and 7/5 minima at 0° as shown in Figure 3.2(a). 8/5 disappeared while a weak 11/7 minima appeared around 35° which later disappeared. 7/5 becomes stronger while 4/3 disappear at 52.1° as depicted in Figure 3.2(e). After about 60°, 4/3 reemerges while 7/5 gets weaker and disappears at higher angles. They have also studied the activation energies corresponds to these minima and suggest the transition from one spin polarization state to another, results in such disappearance and reappearance of FQHE minima[46].

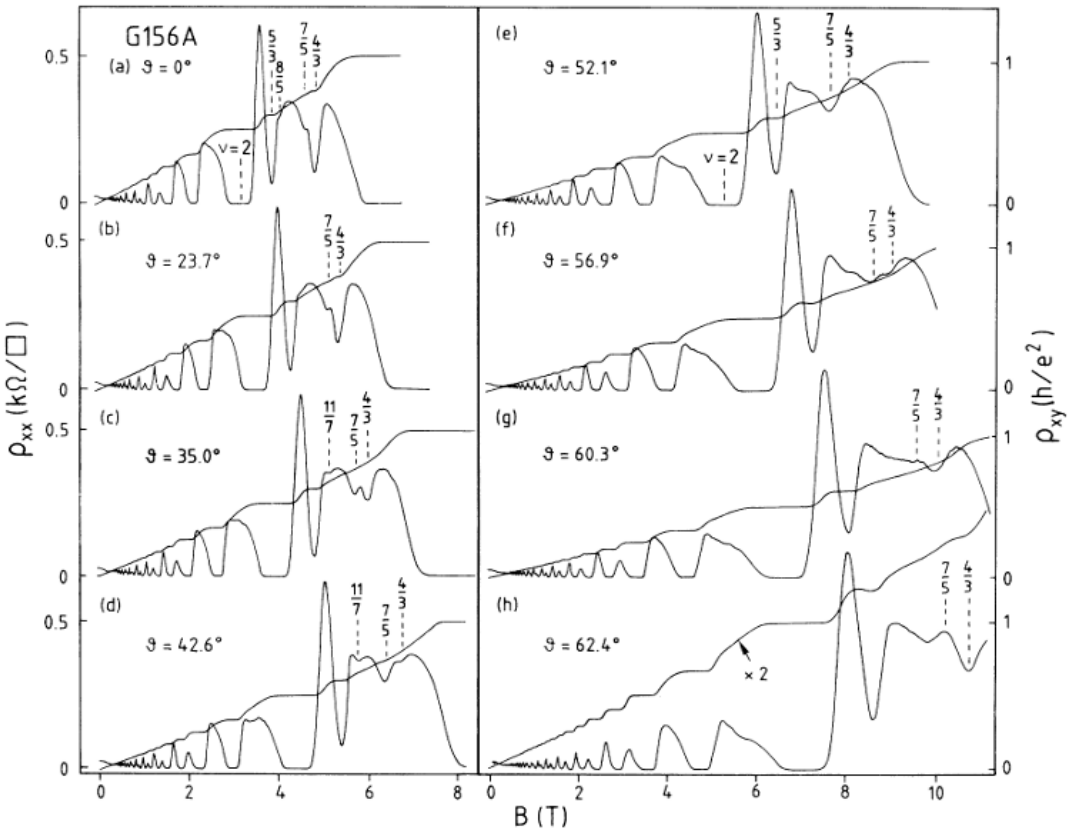


*Figure 3.2 Fractional Quantum Hall Effect of a GaAs/AlGaAs sample at different tilt angles and at 120 mK temperature. Reproduced from Clark et al.,(1989)[46].*

Eisenstein et al., also reported a re-entrant 2/3 energy gap from activation studies, suggestive again of a transition from a spin unpolarized to spin polarized state with increasing total magnetic fields [47]. Engel et al., reported a splitting of the 2/3 and 3/5 states in a tilted magnetic field that is associated with a spin transition [48].

In all the studies mentioned earlier, the analyzed state transitions consistently take place at a fixed filling factor. As these state transitions occur around a constant filling factor ($\nu = p/q$), the initial and final states possess identical quantized Hall resistance, denoted as, $R_{xy} = (p/q)^{-1}(h/e^2)$. In a recent study, Feldman et al., investigated the compressibility of suspended exfoliated graphene. Their findings revealed the presence of phase transitions characterized by areas of negative compressibility, which intersected incompressible peaks at

fractional quantum Hall effect (FQHE) filling factors [50]. Due to the absence of reported standard $R_{xx}$ and $R_{xy}$ measurements, it remains uncertain whether the different phases correspond to the same Hall resistance. Other relevant studies have also examined various aspects of FQHE including spin transitions [51-55].

In this chapter, I will present my experimental findings that revealed tilting a specimen in a fixed magnetic field would change the spin energy and could produce fractionally quantized Hall effect transitions that include both a change in $\nu$ for the $R_{xx}$ minimum [2]. Specifically, a transition from $\nu = 11/7$ to $\nu = 8/5$ and a corresponding change in the $R_{xy}$ from $R_{xy}/R_K = (11/7)^{-1}$ to $R_{xy}/R_K = (8/5)^{-1}$ with increasing tilt angle. Furthermore, the results show a size dependance in the tilt angle interval for the vanishing of $\nu = 4/3$ and $\nu = 7/5$ resistance minima, including "avoided crossing" type line shape characteristics, and observable shifts of $R_{xy}$ at the corresponding $R_{xx}$ minima.

### 3.1 Experimental method

The devices focused on this study were fabricated via standard photo lithography and wet etching techniques from MBE grown single interface GaAs/AlGaAs heterostructure including a triangular quantum well. The Hall bar device[23, 27, 30, 56] includes sections with widths, $W = 400, 200$ and $100\mu m$ as shown in Figure 3.3, in a way that maintains a length to width ratio $L/W = 1$[57]. The devices were characterized by a sheet electron density $n_0(55\ mK) = 2 \times 10^{11} cm^{-2}$ and an electron mobility $\mu(55\ mK) = 1.4 \times 10^7 cm^2/Vs$ after brief illumination during cooldown[58]. The devices also exhibited low density and low mobility conditions characterized by $n_0(55\ mK) = 1.2 \times 10^{11} cm^{-2}$ and $\mu(55\ mK) = 6.5 \times 10^6 cm^2/Vs$ when the specimens were cooled in the dark. The thickness of the 2D electron system is estimated to be ca. 50 nm. Electrical contacts were formed by depositing and alloying Au-Ge/Ni at the Hall bar

contact pads. The sample was wired into a chip carrier, loaded into a dilution refrigerator system, with the sample situated at the center of a superconducting solenoid, and the electrical response was measured using low frequency lock-in based techniques.

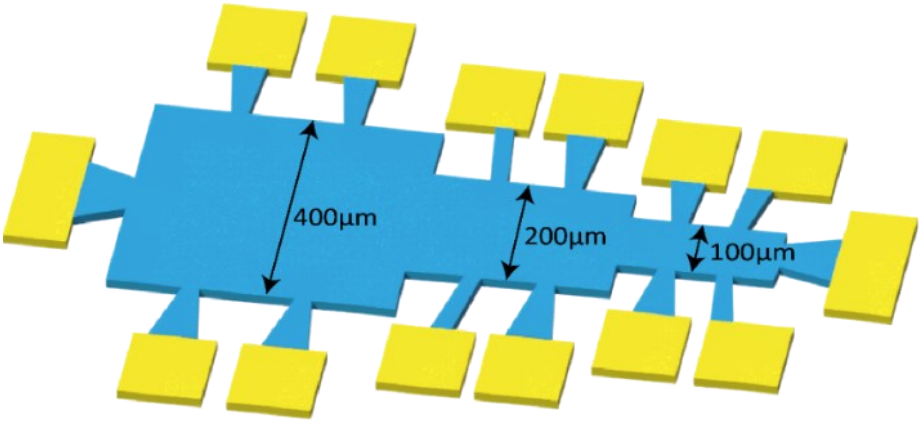


*Figure 3.3. GaAs/AlGaAs heterostructure 2D-electorn gas Hall bar device diagram.*

The applied current to the sample, I, was measured together with the diagonal and Hall voltages. The diagonal and Hall resistances were calculated as the voltages divided by the current. The sample could be tilted in-situ using a geared mechanical system; the tilt angle was determined from the expected $B_{\perp}$ dependence of the Hall effect and an additional angular sensor.

### 3.2 Exploring the Fractional Quantum Hall Effect through sample tilt.

One of the key features of the FQHE is the inverse relationship between the filling factor $(\nu = p/q)$ for the minimum $R_{xx}$ value and the normalized plateau Hall resistance $R_{xy}/R_K = (p/q)^{-1}$. Here, $R_K$ represents a constant value of 25.812 $k\Omega$ [36, 37]. At $\nu \leq 1$, FQHE mostly occur, about $\nu = p/(2kp \pm 1)$, on either side of the half-filled $(\nu = 1/2)$ state[33, 59, 60]. In the GaAs/AlGaAs 2D electron system, the FQHE is observed in the upper spin Landau subband at values such as $\nu = 1 + p/(2kp \pm 1)$. For instance, FQHE is observed at $\nu$ = 4/3, 7/5, 10/7, and so on for $\nu \leq 3/2$. Similarly, at $\nu \geq 3/2$, FQHE is observed at $\nu$ = 2, 5/3, 8/5, 11/7, and so forth[34, 60].

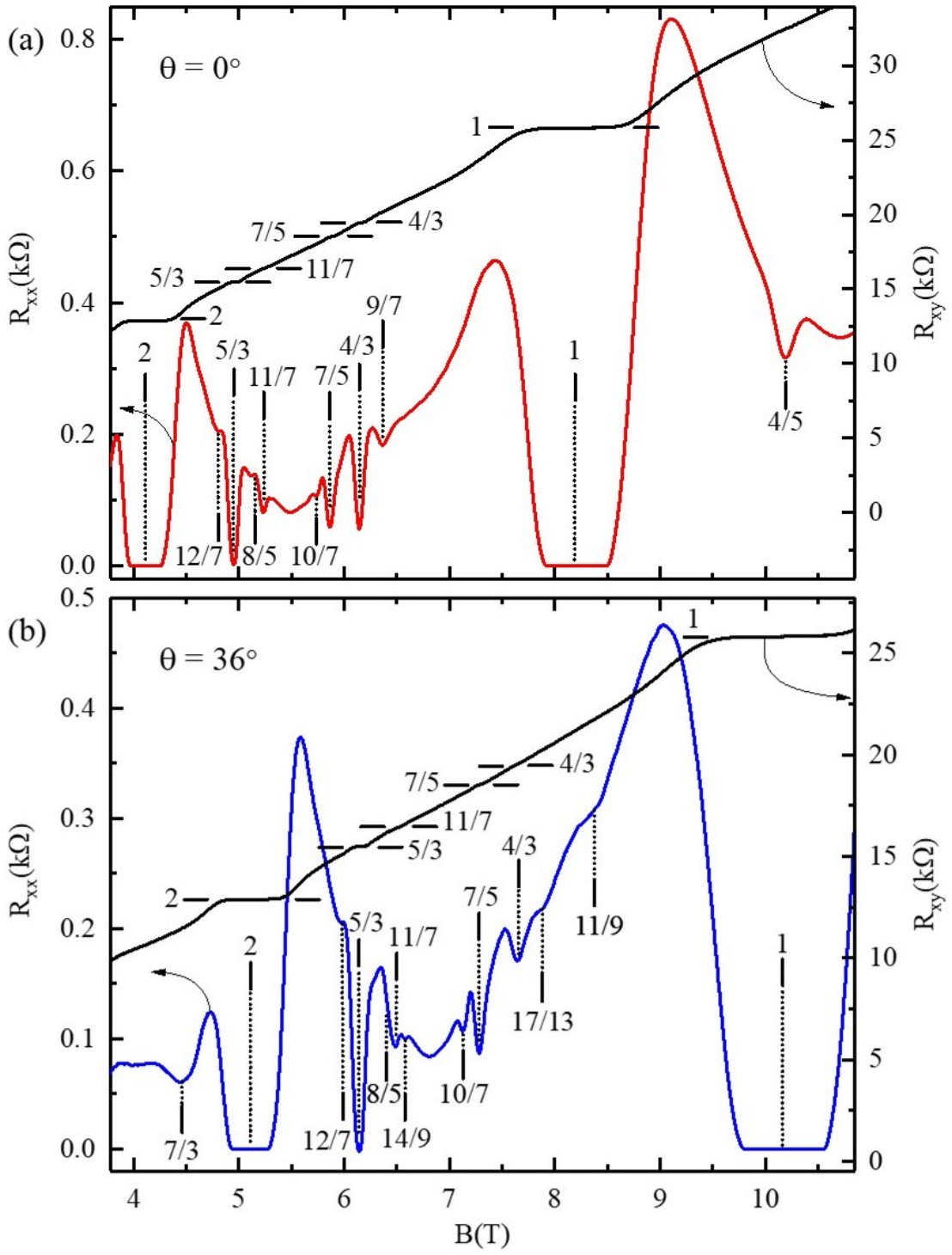


*Figure 3.4 The Hall ($R_{xy}$) and diagonal ($R_{xx}$) resistances of a GaAs/AlGaAs 2DEG Hall bar device at tilt angles $\theta = 0^{\circ}$ and at $\theta = 36^{\circ}$ shown in panel (a) and (b) respectively. The integer and fractional quantum Hall effects are labeled as observed in a device with a width of W = 400 μm at a temperature of 55 mK. Reproduced from Wijewardena et al.,(2022)[2].*

Figure 3.4 (a) shows such FQHE in the $R_{xx}$ and $R_{xy}$ traces against the magnetic field, $B$ with tilt angle $\theta = 0^{\circ}$, where $\theta$ is the angle between the magnetic field and the normal to the 2DEG plane. Figure 3.4(b) depict $\theta = 36^{\circ}$, where integer and fractional quantum Hall effects were moved to a higher total $B$. For $\nu \leq 3/2$, Figure 3.4(a) exhibits FQHE features at 4/5, 9/7, 4/3, 7/5, and 10/7, while for $\nu \geq 3/2$, FQHE features are observable at 5/3, and 11/7. At $\theta = 36^{\circ}$, for $\nu \leq 3/2$, Figure 3.4(b) exhibits FQHE features at 11/9 instead of 9/7, plus 17/13 which is not visible in Figure 3.4(a), in addition to 4/3, 7/5, and 10/7. In Figure 3.4(b) for $\nu \geq 3/2$, FQHE features are observable at 5/3, and 11/7 as in Figure 3.4(a). In addition, 7/3 is visible, with a weak feature at 14/9. Also note that, a resistance minimum is not observable at 8/5 in both Figure 3.4(a) and (b), while QHE at 1 and 2 are observable in both panels. The oscillatory pattern is shifted to higher $B$ in Figure 3.4(b) with respect to Figure 3.4(a) because Landau quantization depends on $B_{\perp}$ while $B = B_{\perp}/\cos(\theta)$ is plotted on the abscissa in Figure 3.4, and the experiment is limited to $0 < \cos(\theta) \leq 1$ for $90^{\circ} > \theta > 0^{\circ}$.

Measurements were carried out in three different sized regions as shown in Figure 3.3 with widths, $W = 400, 200$ and $100\ \mu m$ simultaneously. $R_{xx}$ and $R_{xy}$ traces were obtained at angles corresponding to equal increments in $\cos(\theta)$. The applied magnetic field $B$ is transformed to $B_{\perp} = Bcos(\theta)$, and then to $\nu = hn/eB_{\perp}$, where $n$ is the electron density, $h$ is Planck's constant, and $e$ is the electron charge. The collected line traces were combined to create color plots, as illustrated in Figure 3.5 (a), (c), and (e). The horizontal axis depicts $\nu$. The dark region within the figure signifies $R_{xx}$ minima, while short white vertical bars within the figure panels indicate $\nu$ associated with preeminent FQHE in the exhibited $\nu$ interval.

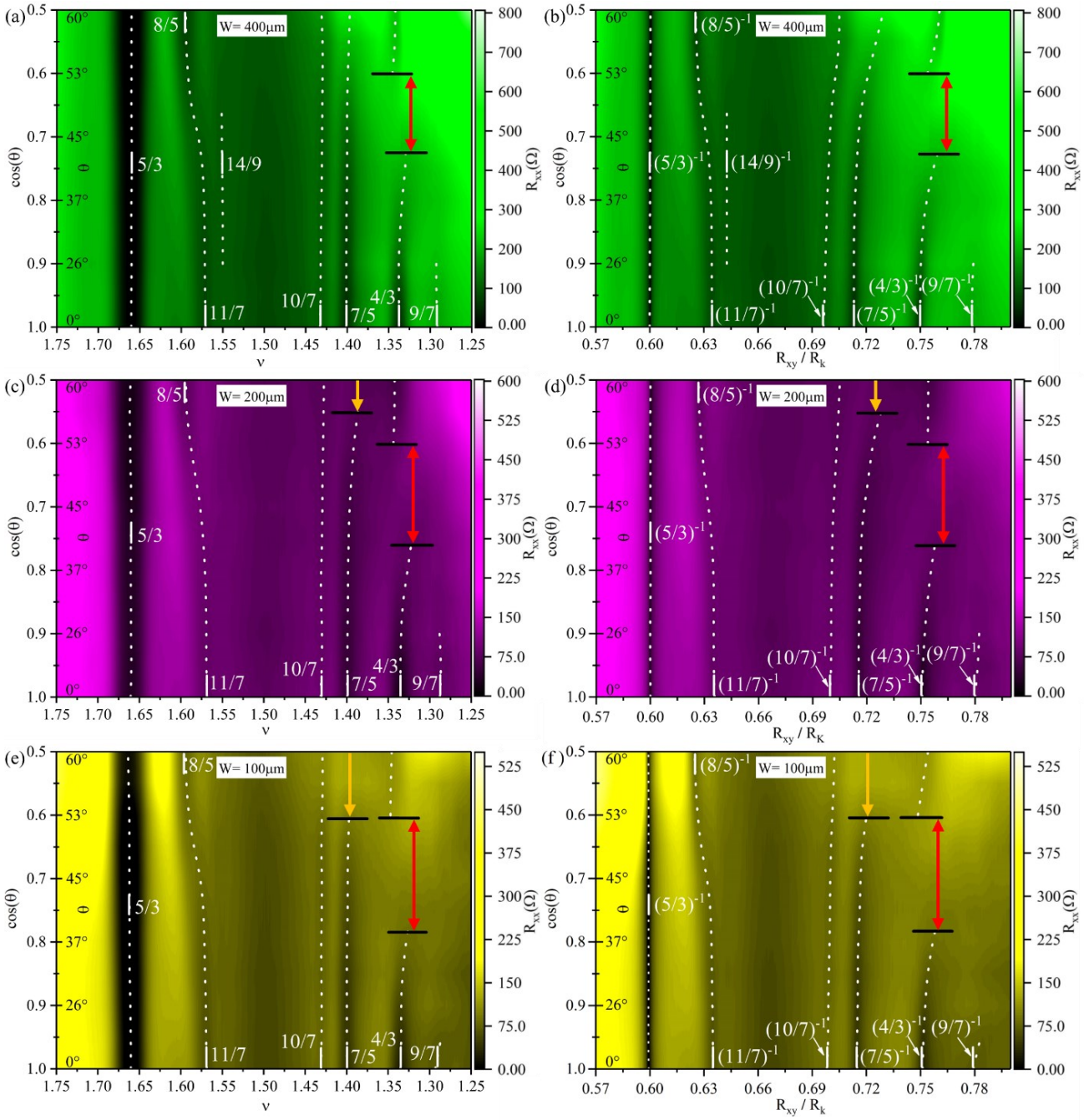


*Figure 3.5. Color plots illustrate the effect of sample tilt in different sized Hall bar devices at 55 mK temperature. Panels in the first column (a, c, e) shows color plots of $R_{xx}$ vs. cos(θ) and vs. ν. Panels in the second column (b, d, f) shows $R_{xx}$ vs. cos(θ) and vs. $R_{xy}$ / $R_K$. Green, magenta, and yellow color plots represent data from the sample regions with a width of 400, 200, and 100 μm respectively. The white dotted lines show the position of $R_{xx}$ minima. The boundary of the angular interval, where the disappearance of the diagonal resistance minimum occurs, is indicated by the black horizontal lines accompanied by colored vertical arrowed lines. Reproduced from Wijewardena et al.,(2022)[2].*

As visible in Figure 3.5 (a), (c), and (e), the 5/3 FQHE minimum is prominent, and it runs vertically. In sharp contrast, the 11/7 $R_{xx}$ minimum that is prominent at $\theta = 0^{\circ}$, $(\cos(\theta) = 1)$ moves toward higher $\nu$ (lower $B_{\perp}$) with increasing angle (decreasing $\cos(\theta)$) and ends up at $\nu = 8/5$ around $\theta \sim 50^{\circ}$, $(\cos(\theta) = 0.65)$. A $R_{xx}$ minimum at 14/9 occurs over a short angular interval only in Figure 3.5 (a). The 10/7 and the 7/5 FQHE minima run mostly vertically in the versus $\nu$ plots of Figure 3.5 (a) and (e). The 7/5 minimum appears to terminate at a smaller angle in the smaller $W$ sections. For instance, the 7/5 terminates at $\theta \sim 53^{\circ}$ in $W = 100\ \mu m$ section, at $\theta \sim 56^{\circ}$ for $W = 200\ \mu m$, while it decays towards $\theta = 60^{\circ}$ in the $W = 400\ \mu m$ section.

In Figure 3.5 (a), (c), and (e), the 4/3 is also prominent near $\theta = 0^{\circ}$ and then vanishes with increasing angle around $\cos(\theta) = 0.73$ in $W = 400\ \mu m$ and around $\cos(\theta) = 0.81$ in $W = 100\ \mu m$, and then reappears at smaller $\cos(\theta)$ (larger $\theta$). A remarkable attribute, which is denoted by the black horizontal lines for the 4/3, is an apparent size dependence in the range of angles over which the 4/3 minimum disappears. The figures depict that the 4/3 minimum vanishes in a broader range of $\theta$ in the narrower Hall bar device. Therefore, for instance, in the $W = 100\ \mu m$ device, the 4/3 resistance minimum disappears between $36^{\circ} \leq \theta \leq 56^{\circ}$, for the $W = 200\ \mu m$ device, it disappears between, $41^{\circ} \leq \theta \leq 56^{\circ}$, while for the $W = 400\ \mu m$ Hall bar device, the same occurs over the narrower interval $43^{\circ} \leq \theta \leq 53^{\circ}$.

To examine the correspondence between $R_{xx}$ and $R_{xy}$, color plots of $R_{xx}$, with $R_{xy}/R_K$ as the abscissa, and $\cos(\theta)$ as the ordinate are presented in Figure 3.5 (b), (d), and (f). Figure 3.5 (b), (d), and (f) show some of the same general features as Figure 3.5 (a), (c), and (e) including these differences:

I. The 5/3 minimum, for example, is narrower in Figure 3.5 (b), (d), and (f) in comparison to Figure 3.5 (a), (c), and (e). This feature follows from the flattening

of the Hall resistance versus $B$ about FQHE $R_{xx}$ minima. When there is a $R_{xx}$ minima and a corresponding plateau in the Hall resistance, $R_{xx}$ occurring at different $B$ then tend to show the same $R_{xy}$ over the $R_{xx}$ minimum, there occurs a "compression" of the $R_{xx}$ minima about the Hall plateau value as seen in Figure 3.5 (b), (d), and (f).

II. Figure 6 (b), (d), and (f) confirms that as the tilt angle increases from $0^{\circ}$ to $60^{\circ}$, $R_{xx}$ minimum at $\nu = 11/7$ moves in filling factor to $\nu = 8/5$, by demonstrating that the associated $R_{xy}$ shifts from $R_{xy}/R_K = (11/7)^{-1}$ to $R_{xy}/R_K = (8/5)^{-1}$.

III. While Figure 3.5 (a), (c), and (e) suggest a disappearance and reentrance of the $R_{xx}$ minimum in the vicinity of $\nu = 4/3$ with increasing $\theta$, Figure 6 (b), (d), and (f) also suggest a corresponding shift in the $R_{xy}/R_K$ in a way that, about "re-entrance", the $R_{xy}/R_K$ differs perceptibly from $R_{xy}/R_K = (4/3)^{-1}$ . That is, at the largest angles, the $\nu = 4/3$ state exhibits a different $R_{xy}/R_K$ relative to $R_{xy}/R_K = (4/3)^{-1}$observed at the smallest angles.

IV. An "avoided crossing" type trajectory for 4/3 about its re-entrance in Figure 3.5 (a), (c), and (e) seems even more pronounced in the Figure 6 (b), (d), and (f). Again, the angular span over which this $R_{xx}$ minimum disappears depends on the Hall bar width $W$, with disappearance over larger angular span at the smaller $W$.

V. The $\nu = 7/5$ state, which shows a mostly vertical trajectory in Figure 3.5 (a), and (e) shows strong bending to larger $R_{xy}/R_K$ at large angles in Figure 3.5 (b), (d), and (f) showing a deviation from $R_{xy}/R_K = (7/5)^{-1}$.

VI. The 10/7 also shows curvature in $R_{xy}/R_K$ towards higher $R_{xy}/R_K$ values in all three sections.

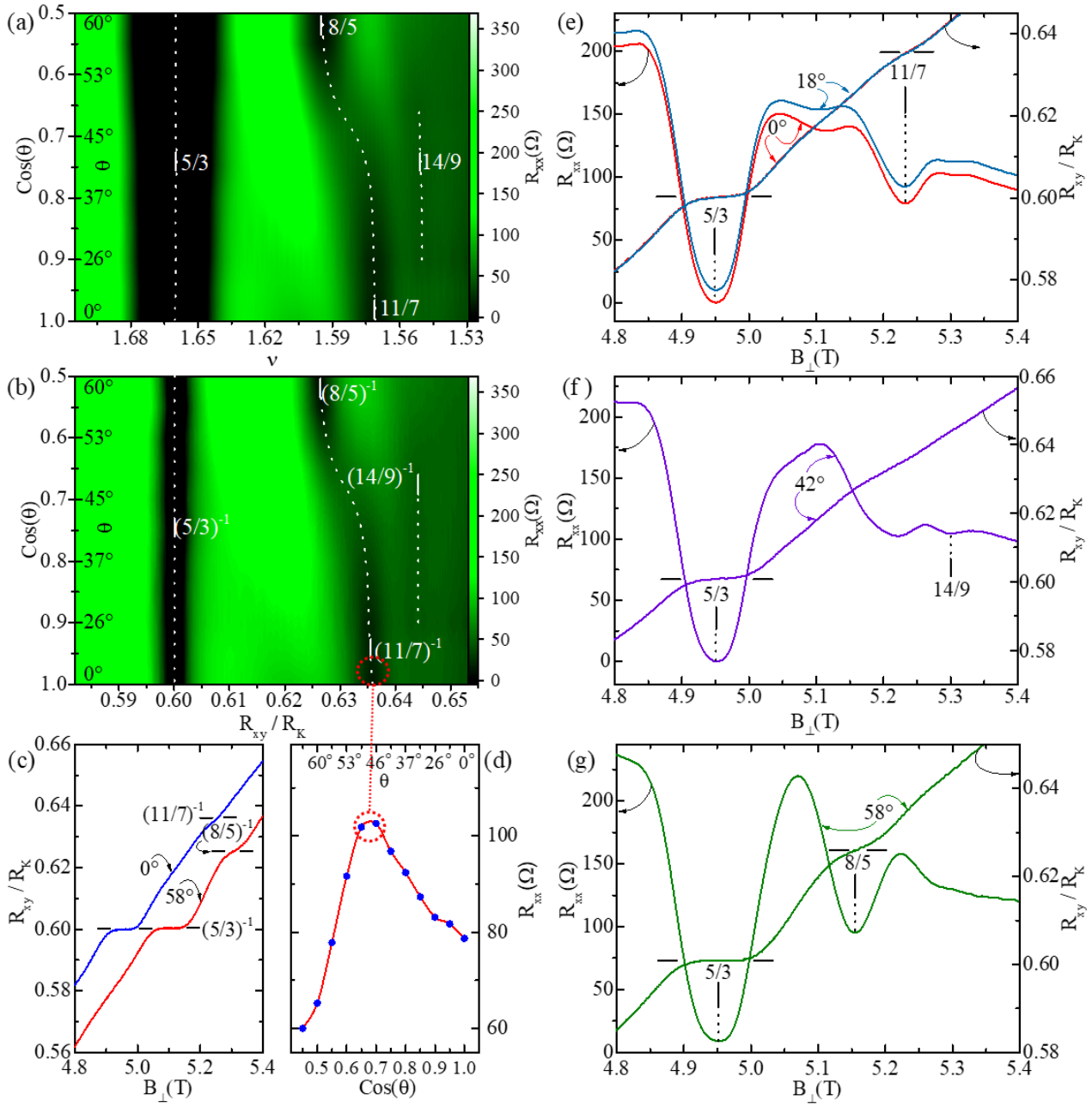


*Figure 3.6. Enlarged view of '11/7' to '8/5' transition with tilt angle (θ) for the Hall bar device with* $400\ \mu m$ *width. (a) A color plot of* $R_{xx}$ *vs.* $\cos(\theta)$*(ordinate) and vs. ν (abscissa). (b) A color plot of* $R_{xx}$ *vs.* $\cos(\theta)$*(ordinate) and vs.* $R_{xy}/R_K$ *(abscissa). The white dotted lines show the trajectory of* $R_{xx}$ *minima. The color bar on the right of (a) and (b) depicts the color scale for the magnitude of* $R_{xx}$*. (c)* $R_{xy}/R_K$ *is plotted vs.* $B_\perp$ $\theta = 0^\circ$ *and* $58^\circ$*. The plots were offset by 0.15 T for clarity. (d) Depict* $R_{xx}$ *values along the white dotted line in (b). (e), (f), and (g) shows the* $R_{xy}/R_K$ *and* $R_{xx}$ *curves against* $B_\perp$ *at* $\theta = (0^\circ, 18^\circ), 42^\circ,$ *and* $58^\circ$*, respectively. The* $R_{xx}$ *trace at* $18^\circ$ *in (e) is offset along the ordinate by 10 Ω. Reproduced from Wijewardena et al.,(2022)[2].*

Figure 3.6 illustrates the crossover that occurs due to the tilt-field between the 11/7 and the 8/5 FQHE in the $400\mu m$ Hall bar device. Figure 3.6 (a) and (b) depict the color plots of $R_{xx}$ with $\cos(\theta)$ on the ordinate as Figure 3.6 (a) depicts $\nu$ as the abscissa, while Figure 3.6 (b) depicts $R_{xy}/R_K$ on the abscissa. As discussed earlier, the narrowing of 5/3 dark -band resistance-minima in the $R_{xy}/R_K$ plot is visible in Figure 3.6 (b). The striking feature emphasized in this color plot is the sharp tilt-induced-crossover from a 11/7 FQHE to the 8/5 FQHE over the narrow angular span of $41^\circ \leq \theta \leq 49^\circ$. Figure 3.6 (c) shows line plots of the Hall resistance at $\theta = 0^\circ$ and $\theta = 58^\circ$. At $0^\circ$, a plateau in the Hall resistance is not visible at 8/5 as this plateau appears near $58^\circ$. Figure 3.6 (d) show the measured diagonal resistance values along the 11/7 → 8/5 resistance minima or the valley (shown in white dotted line in Figure 3.6 (b)) as a function of $\cos(\theta)$ (bottom) and $\theta$ (top). The figure demonstrates that $R_{xx}$ increases first with increasing $\theta$ before start decreasing for $\theta \geq 48^\circ$. Figure 3.6 (e-g) shows some representative line traces of $R_{xx}$ and $R_{xy}$ that were used in generating the color plots shown in Figure 3.6 (a) and (b).

Figure 3.7 highlights the observed resistance minima at $\nu \leq 3/2$ for $W = 400\ \mu m$. Figure 3.7 (a) and (b) show color plots of $R_{xx}$ with $\cos(\theta)$ on the ordinate, as Figure 3.7 (a) shows $\nu$ as the abscissa, while Figure 3.7 (b) shows $R_{xy}/R_K$ on the abscissa. In Figure 3.7 (a) we note that the $R_{xx}$ minimum around $\nu = 4/3$, appears very deep at $\theta = 0^\circ$, see also Figure 3.7 (c), but then becomes weaker with increasing $\theta$, see also Figure 3.7 (d), before vanishing entirely by $\theta = 43^\circ$ (Figure 3.7 (a)). The resistance minimum reappears at $\theta = 53^\circ$. Figure 3.7 (b) which includes $R_{xy}/R_K$ as the abscissa, shows up to a $\approx 2\%$ shift in the Hall resistance after re-entrance to a value above $R_{xy}/R_K = 0.75 = (4/3)^{-1}$. Note that the shape of the dotted lines associated with the "4/3" in Figure 3.7 (b) are reminiscent of "avoided crossing" type lineshape

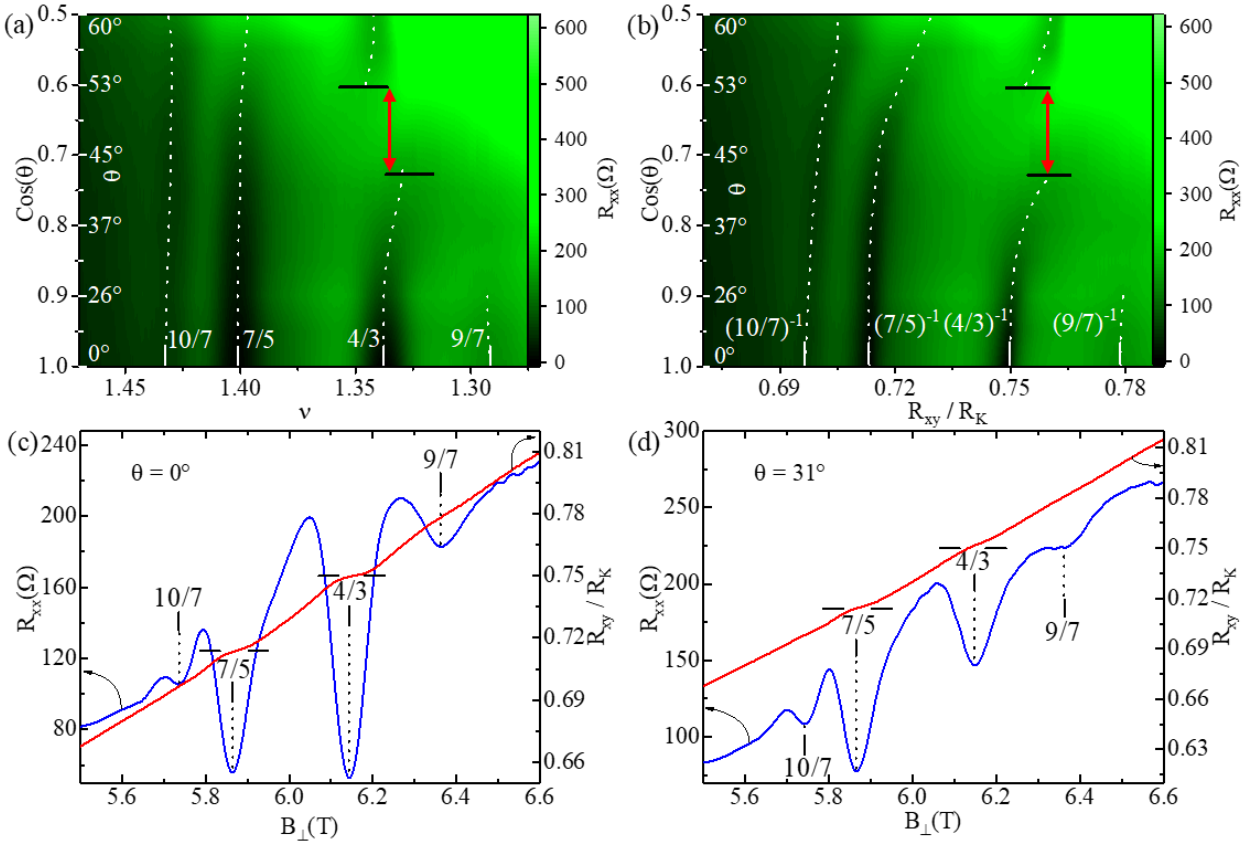


*Figure 3.7 Enlarged view of resistance minima vs. tilt angle for $\nu \leq 3/2$ and W = 400 μm. (a) A color plot of $R_{xx}$ vs. $\cos(\theta)$ and vs. ν. (b) A color plot of $R_{xx}$ vs. $\cos(\theta)$ and vs. $R_{xy}/R_K$. Note the disappearance and re-entrance of FQHE near $\nu = 4/3$ along with a tilt angle dependent shift away in (b) from $R_{xy}/R_K = (4/3)^{-1}$ with increasing $\cos(\theta)$. Here, the arrowed red vertical lines mark the boundary of the angular interval where the $R_{xx}$ minima vanishes. Note the $\cos(\theta)$ dependent shifts also for 10/7 and 7/5. (c) and (d) show the $R_{xy}/R_K$ and $R_{xx}$ traces plotted against $B_\perp$ at $\theta = 0^\circ$ and $31^\circ$ respectively. Reproduced from Wijewardena et al., (2022)[2].*

characteristics. Figure 3.7 (b) also indicates shifts in the 7/5 and 10/7 towards higher Hall resistances with increasing tilt angles. These curved dotted lines associated with the 7/5 and the 10/7 in Figure 3.7 (b) suggest incomplete tilt-induced transitions which may, perhaps, require higher tilt angles and higher fields, beyond what is possible in our setup, to complete the transition. Figure 3.8 illustrates the method utilized to determine the angular span over which the resistance minima vanish. Here, we measured the depth ($\delta R_{xx}$) of the $R_{xx}$ minimum as shown in

the inset of Figure 3.8 plotted the $\delta R_{xx}$ versus $cos(\theta)$, approximated the wings by straight lines, to determine the angular boundaries, as illustrated in Figure 3.8.

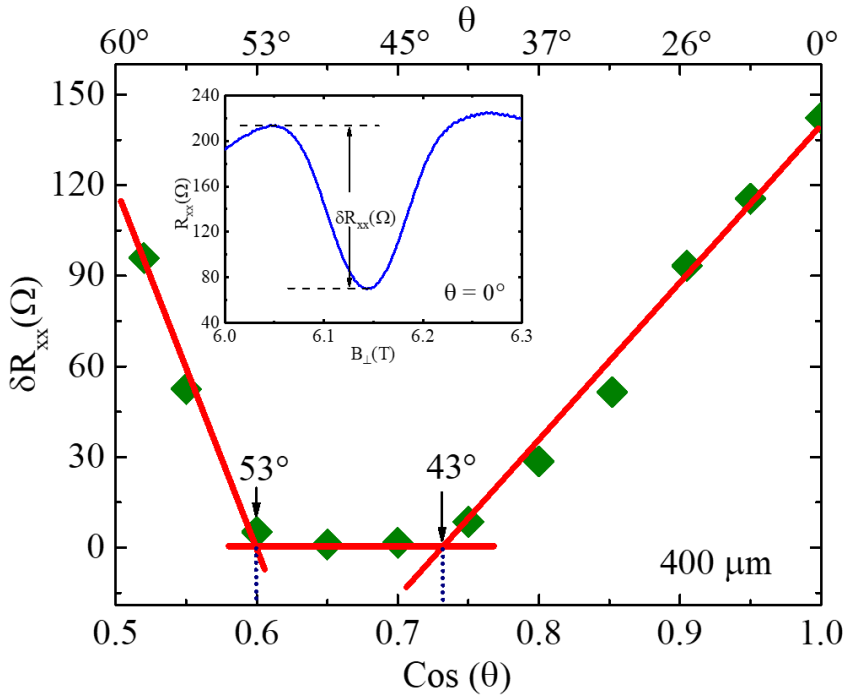


*Figure 3.8 Determination of the angular span where $R_{xx}$ vanishes. The angular span where $R_{xx}$ vanishes is determined by plotting $\delta R_{xx}$ versus $\cos(\theta)$ as shown in inset for 4/3. Reproduced from Wijewardena et al., (2022)[2].*

Figure 3.9 summarizes the Hall resistances obtained at the $R_{xx}$ minima as a function of $\cos(\theta)$ for $\nu \leq 3/2$ in Figure 3.9 (a) and $\nu \geq 3/2$ in Figure 3.9 (b), for $W = 400, 200$ and $100\ \mu m$. Figure 3.9 (a) shows, unsurprisingly, that for $\nu = 1$, the $R_{xy}/R_K = 1$, for the entire examined range of $\theta$. The 4/3 state exhibits the proper value $R_{xy}/R_K = 0.75 = (4/3)^{-1}$ in the absence of tilt within experimental uncertainties. Increasing the $\theta$, or equivalently, decreasing $\cos(\theta)$ produces a progressive shift in $R_{xy}/R_K$ towards higher values in specimens of all three sizes, until the 4/3 state disappears. When it re-appears near $\cos(\theta) = 0.6$ for $W = 400\ \mu m$, remarkably, the $R_{xy}/R_K$ appears shifted downwards relative to the last observable $R_{xy}/R_K$ value before disappearance.

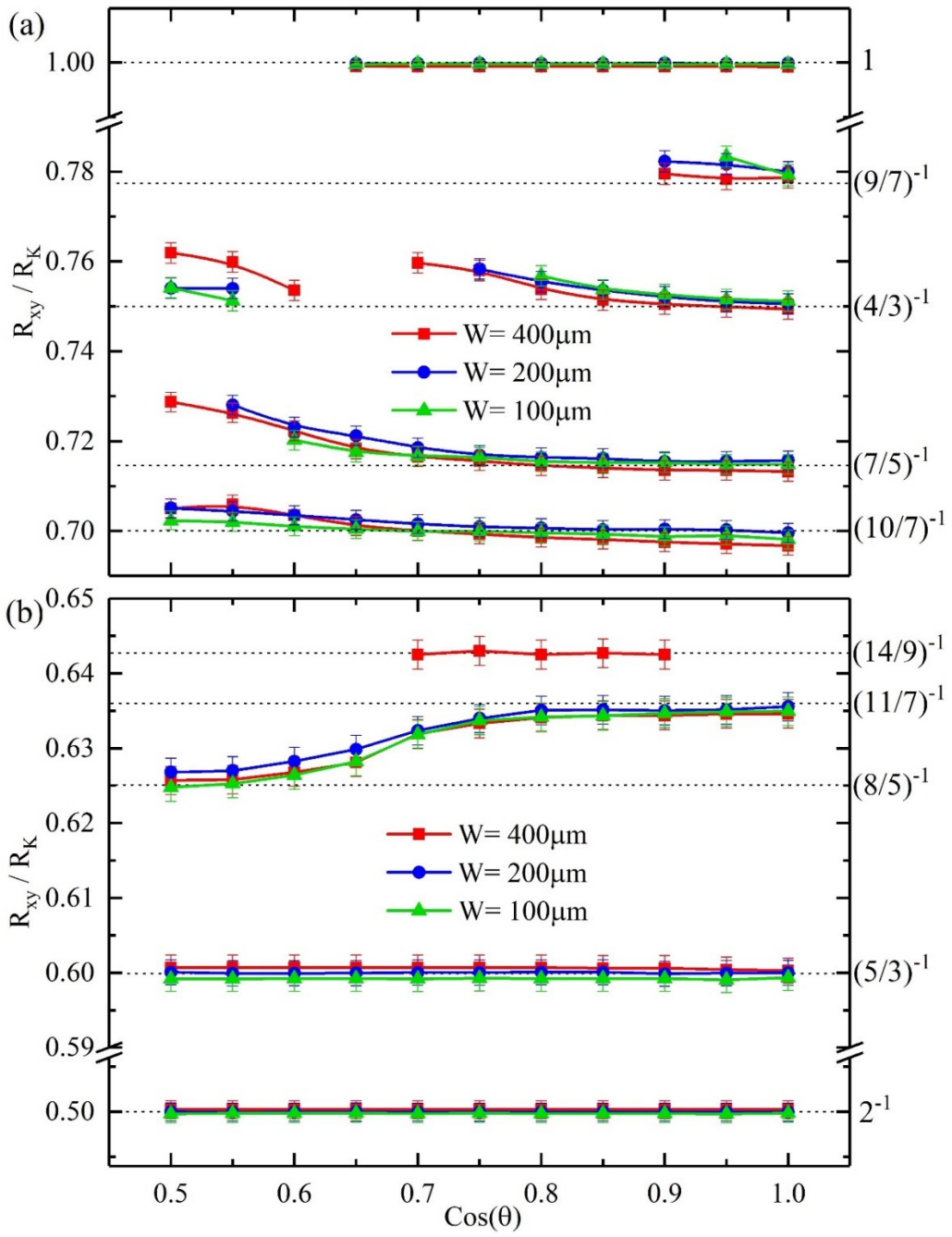


*Figure 3.9 Measured $R_{xy}$ / $R_K$ values at the diagonal resistance minima versus $\cos(\theta)$in Hall bars with W = 400, 200, 100 μm. (a) and (b) illustrate the observed $R_{xy}$ / $R_K$ versus$\cos(\theta)$where θ is the tilt angle, at the corresponding $R_{xx}$ minima for the sample widths of 400, 200, and 100 micrometers. The dotted lines indicate the expected $R_{xy}$ / $R_K$ values at the well-known fractional states labeled on the right ordinate. Note that, $\nu = p/q$, where p/q is a rational fraction, one expects Hall resistance $R_{xy}$ / $R_K$ = $(p/q)^{-1}$ Reproduced from Wijewardena et al., (2022)[2].*

Then, it begins to increase once again with decreasing $\cos(\theta)$. Note that the span of angles, where the 4/3 state vanishes, depends also on the size of the device, with the largest span for the vanishing minima in the narrowest specimen. The 7/5 and the 10/7 also indicate a progressive shift to larger $R_{xy}/R_K$ with decreasing $\cos(\theta)$ or increasing $\theta$. Figure 3.9 (b) shows that the $R_{xy}/R_K = 0.5 = 2^{-1}$ for the $\nu = 2$ QHE and $R_{xy}/R_K = 0.6 = (5/3)^{-1}$ for the $\nu = 5/3$ FQHE, independent of the tilt angle or $\cos(\theta)$. On the other hand, the 11/7 FQHE turns into the 8/5 FQHE with increasing tilt angle or decreasing $\cos(\theta)$. The 14/9 FQHE, which makes a brief appearance for an intermediate set of angles in the $= 400\ \mu m$ section, shows the expected $R_{xy}/R_K$ within experimental uncertainties.[61]

### *3.2.1 Analysis of activation energies*

In order to have a better understanding of the underline physics, the activation energies of 8/5, 11/7, 7/5, and 4/3 FQHE were extracted utilizing a similar technique introduced by Mani et. al.,(2021)[61]. We utilized microwave photoexcitation[62-68] to produce the heating required for the activation energy study. To achieve this objective, a cryostat was equipped with a microwave coaxial line connected to a magnetic dipole wire loop that wraps around the sample. This setup allowed for the transmission of externally generated microwaves to the sample. The microwaves were produced using a microwave synthesizer controlled by a computer, which enabled adjustment of both the frequency (*f*) and power (*P*). The coaxial line delivered the microwaves to the sample while the refrigerator maintained the base temperature.

Figure 3.10 (a) depicts line plots of $R_{xx}$ against *B* at microwave power levels between $-19 \leq \mathrm{P} \leq 3$ dBm at increments of $\Delta\mathrm{P} = 1\mathrm{dBm}$. The frequency was intentionally set to 20 GHz to make sure it is low enough to eliminate the possibility of single particle spin-resonance within the magnetic field range being studied[61].

Here, the microwave power units *dBm* (decibel-milliwatt) is defined as $dBm = 10\log(P(mW)/1mW)$. The power levels (*P*) are determined at the source and do not consider factors such as insertion losses, attenuation losses in the coaxial line, and other mismatch effects. The figure illustrates a gradual and continuous variation in the resistance curves, exhibiting a reduction in the amplitude of the oscillatory resistance fluctuations as the power level approaches 3 dBm[64]. As the resistance variation observed with increasing power (*P*) resembles the impact of temperature changes, additional transport measurements were conducted in the absence of microwave excitation (dark conditions), to investigate the temperature dependence. The results of these measurements are depicted in Figure 3.10 (b) for $50 \leq \mathrm{T} \leq 840$ mK. As depicted in Figure 3.10 (b), it is apparent that elevating the temperature results in a decline in the amplitude of the oscillatory variation, analogous to the effect observed when increasing *P* in Figure 3.10 (a).

The striking resemblance between the $R_{xx}$ vs. *B* curves in Figure 3.10 (a) with respect to *P* and in Figure 3.10 (b) with respect to *T*, prompted an investigation into the correlation between the effects of microwave power and sample temperature. The results from such an investigation are shown in Figure 3.11. Figure 3.11 (a) depicts $R_{xx}$ vs. *B* traces collected at several different temperatures superimposed on $R_{xx}$ vs. *B* traces collected with several different microwave power levels. We found that dark traces obtained at various temperatures can be correlated with a photo-excited trace at a specific power level across the entire range of magnetic fields we examined. As an example, Figure 3.11 (a) depicts that the $P = -14\ dBm$ $R_{xx}$ vs. *B* trace is same as the $R_{xx}$ vs. *B* dark trace collected at 120 *mK.* Also, the $P = -10\ dBm$ photo-excited curve is identical to the $T = 240\ mK$ dark curve. Similarly, the dark trace collected at $T = 360\ mK$ matches with the $P = -3\ dBm$ trace, and the $P = 2\ dBm$ curve can be superimposed on the

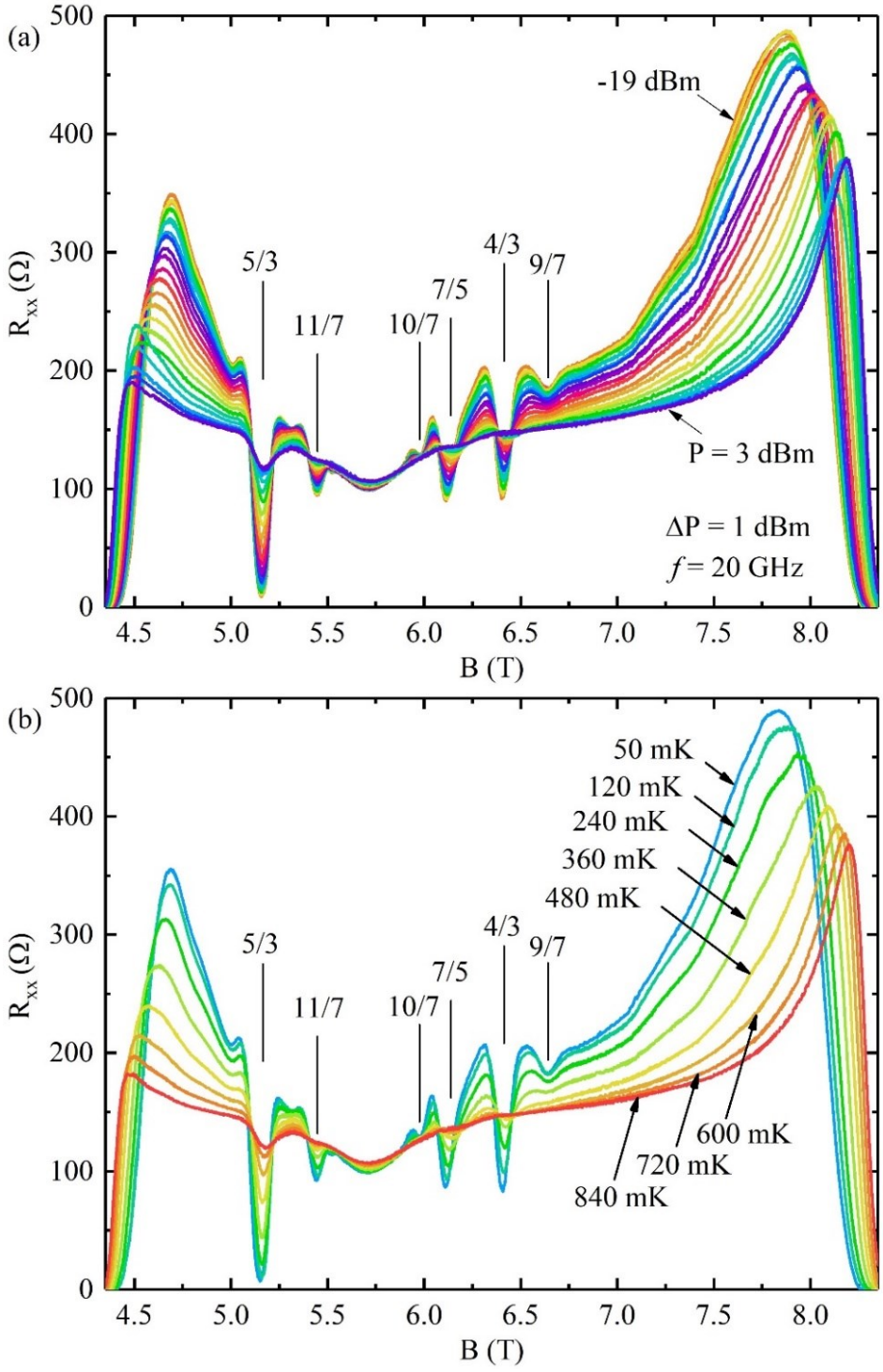


*Figure 3.10 Temperature dependance of FQHE. (a) $R_{xx}$ versus B at different microwave power P between $-19 \leq P \leq 3\ dBm$ in steps $\Delta P = 1 dBm$ at frequency f = 20GHz. (b) $R_{xx}$ versus B is plotted at temperatures $50 \leq T \leq 840\ mK$. Some of the fractions are marked by vertical lines in both panels.*

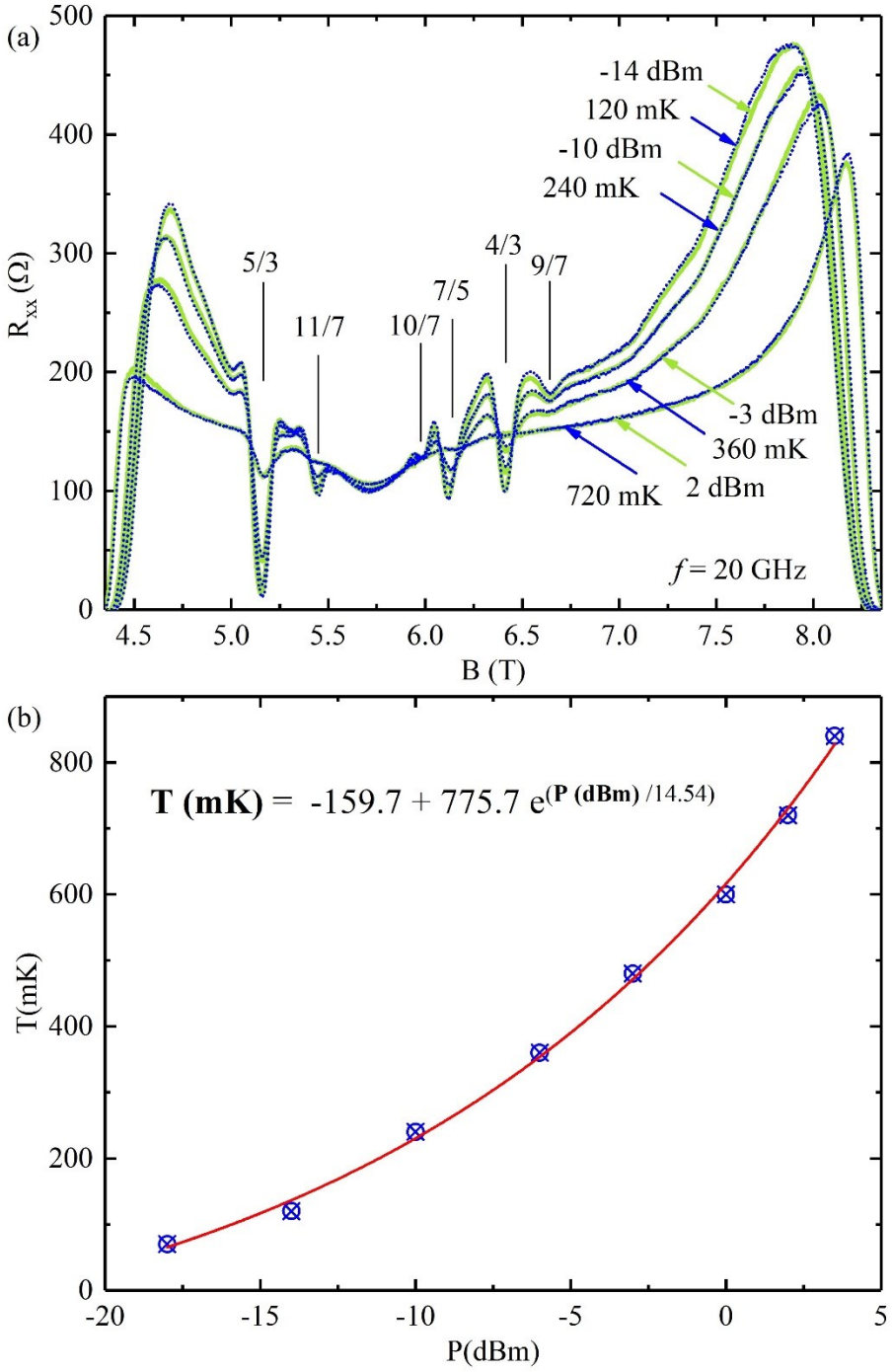


*Figure 3.11 Superimposition of power- and temperature- traces of $R_{xx}$ versus B and determining the carrier temperature at a specific microwave power level. (a) $R_{xx}$ versus B traces collected at different P (microwave power) were superimposed by dark $R_{xx}$ versus B curves collected at some temperatures, T. The findings indicate a strong correlation between the power and temperature traces across the entire range of displayed magnetic fields. (b) The carrier temperatures (T) corresponding to different microwave powers (P) are determined by aligning the power traces with the temperature traces, as depicted in the upper panel.*

dark curve obtained at $720\ mK$. The effective temperature at each microwave power level can be extracted by matching the $R_{xx}$ vs. $B$ traces collected at different temperatures and different power levels. The extracted temperatures were plotted against the corresponding microwave power level in Figure 3.11 (b). An equation that represents the correlation between the temperature and the microwave power is identified by fitting a curve to the data as shown in Figure 3.11 (b). The equation, $T(mK) = 775.7e^{(P(dBm)/14.54)} - 159.7$ can be utilized to convert microwave power-dependent data into temperature-dependent data, thereby offering a faster method for gathering the required data to study the activation energy of the FQHE.

Figure 3.12 (a) depict the extraction of activation energies from temperature dependence of $R_{xx}$.Figure 3.12 (b) summarizes measurements of the activation energies $\Delta$ as a function of $\cos(\theta)$ over the observed 11/7 → 8/5 crossover, while the inset in Figure 3.12 (b) shows the $R_{xx}$ vs. $B_{\perp}$ at the various tilt angles $\theta$. As in Figure 3.6 (d), the Figure 3.12 (b) inset shows that $R_{xx}$ at the minima initially increase with increasing $\theta$ before decreasing for $\theta \geq 47^0$. Figure 3.12 (b) shows that the $\Delta$ decrease initially with increasing $\theta$ before increasing once again for $\theta \geq 47^0$. These results (Figures 3.5, 3.6, and 3.12) indicate that tilting the specimen can, not only induce a crossover from one spin polarized state to another at the same filling factor as previously understood, but that tilt can also induce a crossover from one FQHE to another distinct FQHE.

Figure 3.13 exhibits the activation energies as a function of $\cos(\theta)$ (lower abscissa) for the 4/3 and 7/5 resistance minima. Figure 3.13 shows that the $E_A$ tends to vanish over the angular interval where the 4/3 minima vanish in Figure 3.7 (a) and (b). Figure 3.13Figure 3.12 also shows that for the 7/5, $E_A \rightarrow 0$ as $\theta \rightarrow 60^{\circ}$.

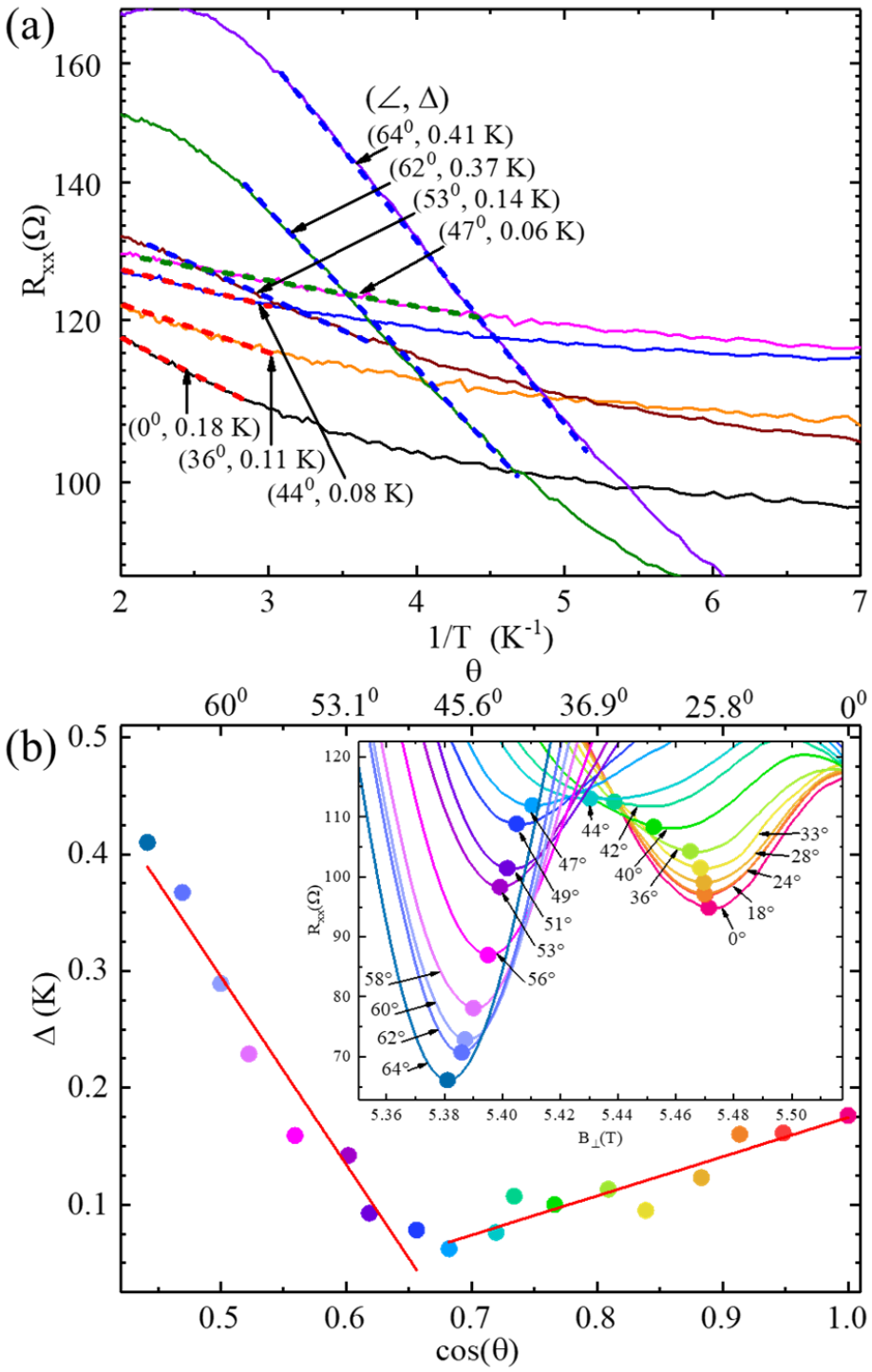


*Figure 3.12 Activation energies in the '11/7' to '8/5' transformation with tilt angle θ (a) $R_{xx}$ versus 1/T traces are exhibited for various angles θ here along with extracted activation energies. (b) The activation energy Δ is plotted vs. $\cos(\theta)$ and θ where θ is tilt angle, for $W = 400\ \mu m$. The figure shows that the Δ decreases with increasing angle until $\theta \approx 47^{\circ}$, before beginning to increase with θ. The inset shows the $R_{xx}$ vs. $B_\perp$ traces highlighting the 11/7−8/5 crossover versus θ at base temperature. Reproduced from Wijewardena et al.,(2022)[2].*

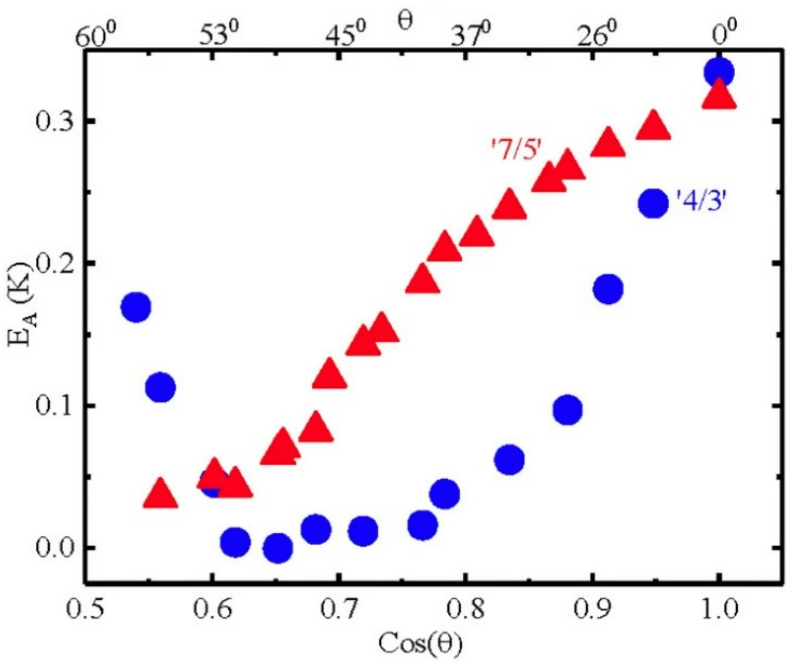


*Figure 3.13 The activation energies $E_A$, as a function of $\cos(\theta)$ for the 4/3 and 7/5, respectively. Note that the $E_A$ tends to vanish over angles where the resistance minima vanish. Reproduced from Wijewardena et al.,(2022)[2].*

### *3.2.2 The effect of sample tilt relative to B in low mobility and density conditions*

The GaAs/AlGaAs heterostructure devices examined for the above, also exhibited a low density ($n \sim 1.2 \times 10^{11}\ cm^{-2}$), low mobility ($\mu \sim 6.6 \times 10^{6}\ cm^{2}/Vs$) condition, when the specimens were cooled in the dark. These specimens, in this low mobility condition, exhibited fewer perceptible FQHE over the interval $1 \leq \nu \leq 2$. Yet, the 5/3 and 4/3 FQHE's were prominent in the un-tilted (θ = 0°) condition, with the specimen normal parallel to the magnetic field as shown in Figure 3.14 (a). At a tilt angle of θ = 60° of the specimen normal with respect to the magnetic the 5/3 minimum becomes deeper, as the 4/3 disappears, as depicted in Figure 3.14 (b). In comparing panels (a) and (b), we observe that the $\nu = 4/3$ resistance minimum of panel (a) becomes unobservable in panel (b), while an imperceptible $\nu = 7/5$ resistance minimum in panel (a) becomes observable in panel (b).

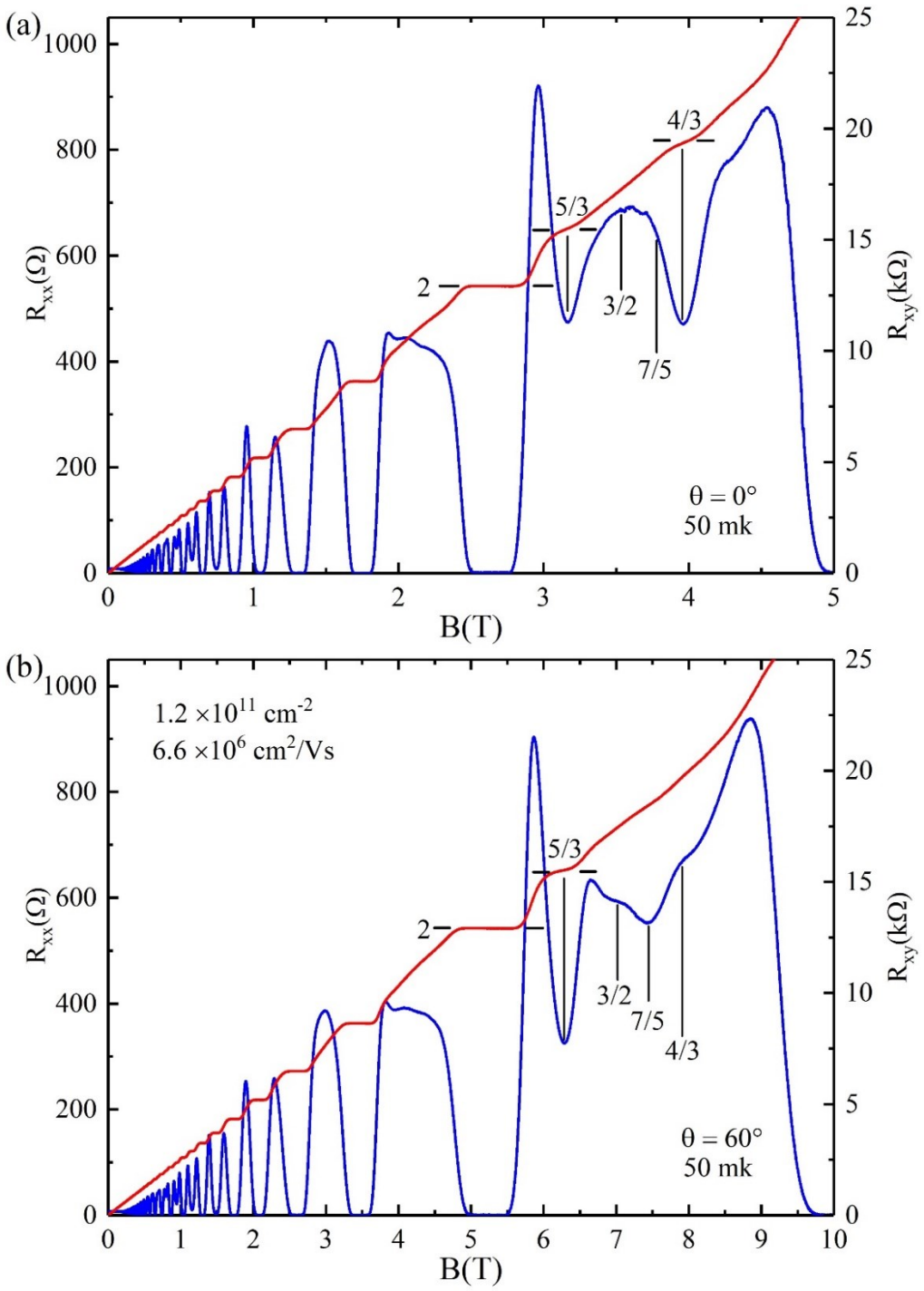


*Figure 3.14 The diagonal and Hall resistances versus the magnetic field in a GaAs/AlGaAs heterostructure in the low mobility, low density condition. The diagonal resistance ($R_{xx}$) and Hall resistance ($R_{xy}$) are shown with some marked Integral (I) and Fractional (F) Quantized Hall Effects (QHE). (a) The $R_{xx}$ - and $R_{xy}$ - vs B at a tilt angle $\theta = 0°$, where the sample normal is parallel to the magnetic field. (b) The results at a tilt angle $\theta = 60°$. Reproduced from Wijewardena et al.,(2022)[2].*

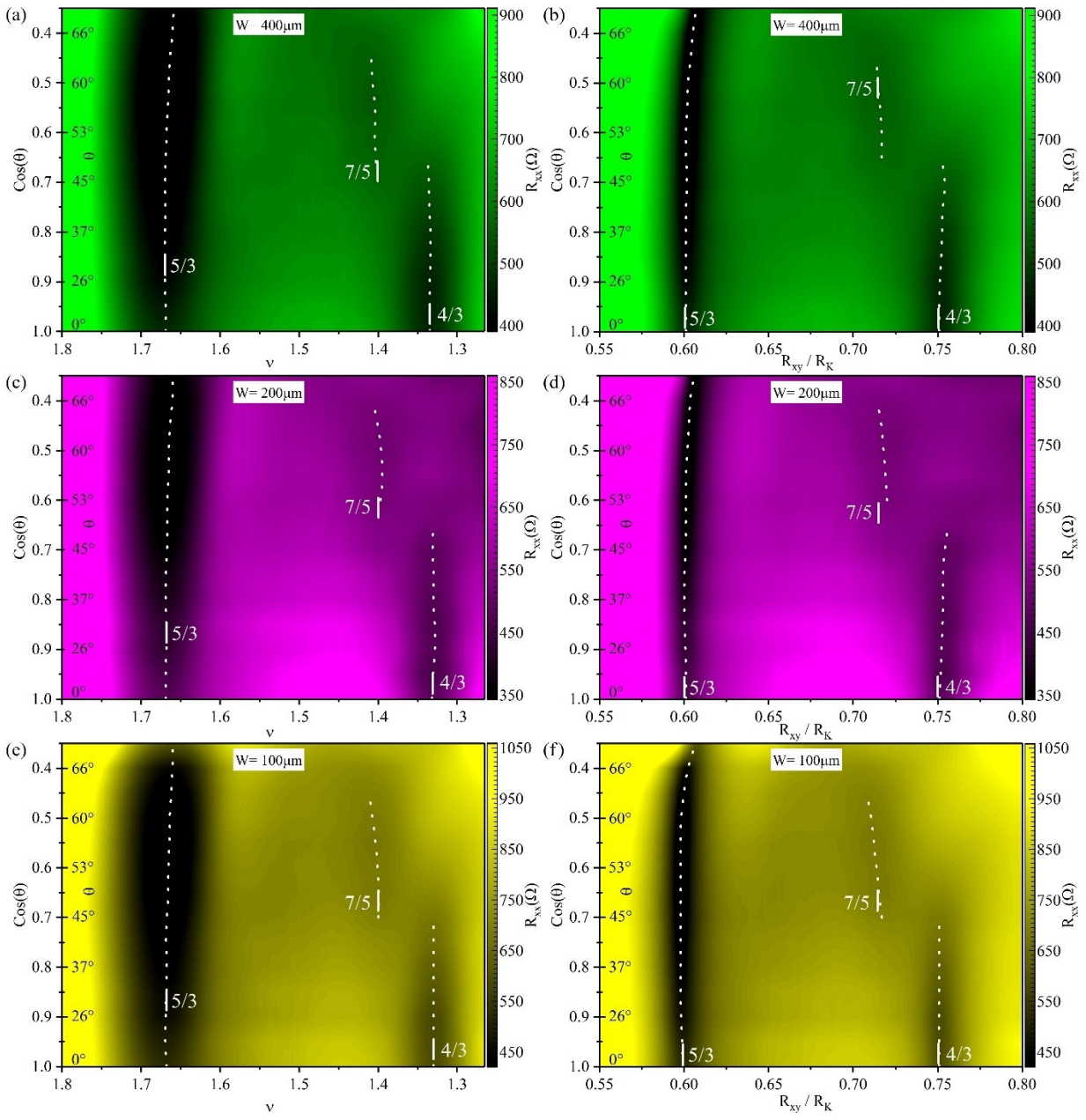


*Figure 3.15 Color plots of the tilt field effect in a low-density specimen with different widths (W). (a), (c), and (e) depict color plots of $R_{xx}$ vs. $\cos(\theta)$ and vs. $\nu$ for W = 400, 200, and 100 μm, respectively. (b), (d), and (f) shows color plots of $R_{xx}$ vs. $\cos(\theta)$ and vs. $R_{xy}$ / $R_K$ for W = 400, 200, and 100 μm, respectively. The dotted lines follow the $R_{xx}$ minima. Here, T = 55 mK, and n = 1.2 × $10^{11}$$cm^{-2}$ Reproduced from Wijewardena et al.,(2022)[2].*

Color plots of $R_{xx}$ with $\cos(\theta)$ as the ordinate, and with ν as the abscissa, are shown in Figure 3.15 (a), (c), and (e). Dark bands in the figure indicate resistance minima and

the trajectory of the minima are indicated by the dotted lines; short white vertical lines within the figures indicate ν associated with observable FQHE in the exhibited ν interval. In Figure 3.15 (a), (c), and (e), the 5/3 FQHE minimum is prominent, it runs mostly vertically, and bends towards lower filling factors at the highest angles. The 4/3 is observable over the approximate angular span $0^{\circ} \leq \theta \leq 45^{\circ}$. Once the 4/3 minima disappear, the 7/5 minima become observable, and the 7/5 minimum appears to bend towards higher filling factors with increasing angle. The 7/5 minimum become unobservable above θ ≈ 63°. An obvious size dependence is not discernable in this low density, low mobility condition.

Color plots of $R_{xx}$ with $R_{xy}/R_K$ as the abscissa, and $\cos(\theta)$ as the ordinate are exhibited in Figure 3.15 (b), (d), and (f). Figure 3.15 (b), (d), and (f) show some of the same general features as Figure 3.15 (a), (c), and (e), including these differences:

I. The dark bands associated with the $R_{xx}$ minima appear narrower here, as also observed in the high mobility condition.

II. An appreciable shift is observable in the Hall resistance of the 5/3 at the highest angles, θ ≥ 60°. This feature seems to suggest that the 5/3 could disappear at even higher angles.

III. The dark band associated with the 4/3 resistance minimum tracks to higher values of $R_{xy}/R_K$ with increasing angle before it vanishes.

IV. The dark band associated with the 7/5 resistance minimum tracks to smaller values of $R_{xy}/R_K$ before it too vanishes. In the vicinity of the crossover point where the 4/3 vanishes and the 7/5 appears at around θ = 49°, the lineshapes of two branches together are reminiscent of an “avoided crossing”.

Figure 3.16 shows plots of $R_{xx}$ vs. $\cos(\theta)$ along resistance minima (dotted lines) in Figure 3.15 for $W$ = 400, 200, and 100 $\mu m$ wide sections in panels (a), (b), and (c), respectively.

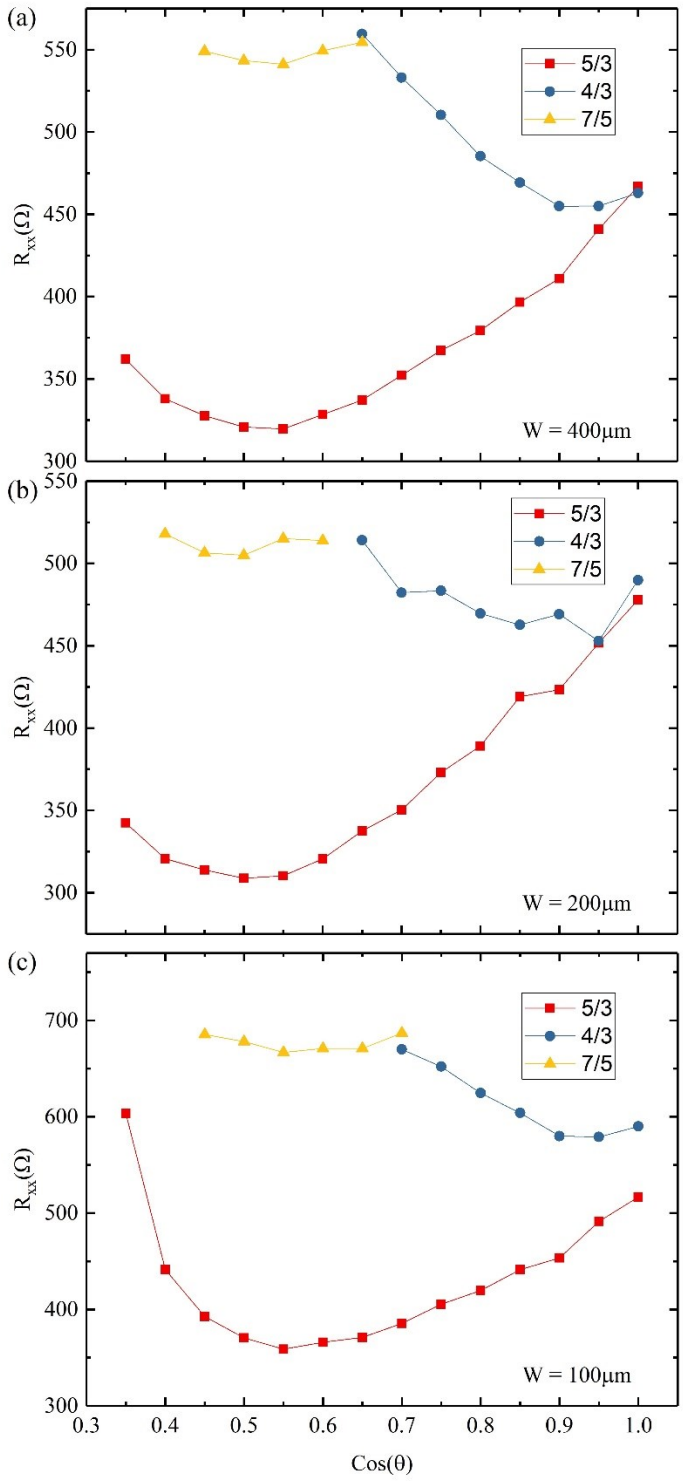


*Figure 3.16 $R_{xx}$ is plotted versus $\cos(\theta)$ along the resistance minima (white dotted lines) of $R_{xx}$ vs. $\cos(\theta)$ and vs. $\nu$ color plots in a low-density specimen. The minima diagonal resistance ($R_{xx}$) is shown vs. $\cos(\theta)$ in panels (a), (b), and (c), for the W = 400, 200, and 100 μm sections, respectively. Reproduced from Wijewardena et al.,(2022)[2].*

All three panels show that the 5/3 resistance drops with increasing angle to $\theta \approx 60°$ before increasing again at higher angles. We note that the increase in $R_{xx}$ for $\theta \geq 60°$ correlates with the shift of the corresponding dark bands away from $R_{xy}/R_K = (5/3)^{-1}$ Figure 3.15 (b), (d), and (f). In addition, the 4/3 resistance increases with increasing $\theta$ (or, equivalently, decreasing $\cos(\theta)$). It looks like the 7/5 becomes visible when its resistance falls below the 4/3 resistance.

### 3.3 Discussion

Here, we experimentally examined the diagonal and Hall resistances, observe dissimilar dependence when the results are plotted vs. $\nu$ (Figure 3.5 (a), (c), and (e)), and versus $R_{xy}/R_K$ (Figure 3.5 (b), (d), and (f)), respectively, and report a striking tilt-induced crossover from one fractional quantized Hall resistance state to another, e.g., 11/7 to 8/5, which suggests a tilt or Zeeman-energy-induced-crossover between different FQHE states associated with different $\nu$. Further, we showed that,

I. "Re-entrance" at $\nu = 4/3$ (see Figure 3.5 (a), (c), and (e)) includes also a shift in $R_{xy}/R_K$, (see Figure 3.5 (b), (d), and (f)).

II. An "avoided-crossing" type lineshape is suggested by the dotted lines in Figure 3.5 (b), (d), and (f) around a 4/3 transition.

III. There is also a size dependence in the angular interval associated with the $\nu = 4/3$ crossover (see Figure 3.5 (a), (c), and (e)).

IV. There is a size dependence in the angle associated with the disappearance of the $\nu = 7/5$ at high tilt angles (Figure 3.5 (a), (c), and (e)).

V. There also appears to be a curvature in the track of the resistance minimum when plotted vs $R_{xy}/R_K$ for the 4/3, 7/5 and 11/7 (see Figure 3.5 (b), (d), and (f)).

At the moment, it appears that the Hall resistance shift from $R_{xy}/R_K = (11/7)^{-1}$ to $R_{xy}/R_K = (8/5)^{-1}$, see Figure 3.9, reflects a crossing-trajectory from one canonical FQHE to another. Perhaps, for $\nu \leq 3/2$, curvature in the track of the resistance minima when plotted vs $R_{xy}/R_K$ reflect incomplete tilt induced crossovers, which require higher tilt angles and higher magnetic fields for their completion.

We begin by commenting upon the origin of size dependence in the angular interval in Figure 3.5 marked by black horizontal line segments with colored arrows within them, for the disappearance of the "4/3" and "7/5" FQHE's. A recent microwave power and temperature dependent study suggests that odd denominator rational fractional fillings of Landau levels, where the $R_{xx}$ minima disappear in a crossover range of tilt angles, exhibit so-called marginal metallic states, which are characterized by a profound temperature/microwave power insensitivity in the diagonal resistance [61]. In such a marginal metallic state, carrier, or composite fermion [69], interaction with the boundary is likely to determine size effects. Note that the color plots suggest that the angular span for the absence of a resistance minimum depends on sample size. Characteristics size scales of relevance here could be the sample size ($W$), the carrier localization length, $l_{loc}$, and perhaps the phase coherence/inelastic lengths[70, 71]. Assume that, in analogy to the metallic state observed at the center of Landau levels in the integral quantum Hall regime[70], the carrier, or composite fermion[69], localization length here is a function of the angle and varies similarly with angle in all three Hall devices. Further, for the sake of discussion, let us say that the localization length tends to diverge at some definite angle, say $\theta_c \sim 50^{\circ}$ for the "4/3" in Figure 3.5 (a), (c), and (e). As the localization length becomes larger on $\theta \rightarrow \theta_c$ from either side, the narrowest device $W = 100\ \mu m$ first satisfies the condition $W \geq l_{loc}$. Upon realizing this condition, carriers in this device are effectively delocalized as they

interact with the boundary, this Hall bar becomes "metallic," which leads to the vanishing of the resistance minimum and a temperature- or microwave power- independent diagonal resistance[61]. A closer approach to $\theta_c$ increases the localization length further such that the $W = 200\ \mu m$ specimen is the next to become "metallic," followed by the $W = 400\ \mu m$ device with an even closer approach to $\theta_c$. Such an explanation invoking the reduced role for localization in the narrower sample provides a qualitative understanding for the size dependence of the angular width for the disappearance of the resistance minima for the 4/3 and 7/5 trajectories in Figure 3.5[70].

Landau level crossings can occur upon varying the Zeeman energy with respect to the Landau level energies and such crossings can be manifested in transport[72, 73]. Following the work of Du et al.[69], which carried out such level crossing analysis in the FQHE regime, we provide here, for the sake of completeness, a composite-fermion-Landau-level (CF-LL) crossings analysis of the Figure 3.5 data, see Figure 3.17. In this approach, FQHE states around $\nu = 3/2$ are equivalent to IQHE states of composite fermions, of mass $m^*$ originating from $\nu = 3/2$ which are associated with CF Landau levels that are spaced by $\hbar eB_{eff}/m^*$ due to an effective magnetic field $B_{eff} = 3\left(B_\perp - B_{\perp,3/2}\right)$ with $B_\perp$ and $B_{\perp,3/2}$ the perpendicular component, and the perpendicular component at $\nu = 3/2$ respectively, of the magnetic field. While $B_{eff}$ sets the field scale for CF-LL quantization, the Zeeman energy depends upon the total magnetic field $B_{tot} = B_\perp/\cos(\theta)$. When the spin level of one CF Landau level coincides with the spin level of another CF Landau level due to, say, changing the tilt angle, the spectral gap disappears and $R_{xx}$ exhibits a relative resistance maximum. This coincidence condition is given by setting the Zeeman energy equal to integral multiples of CF-LL energy: $g^*\mu_B B_{tot} = j\hbar eB_{eff}/m^*$ with $j = 1, 2, 3$ ... [52, 69].

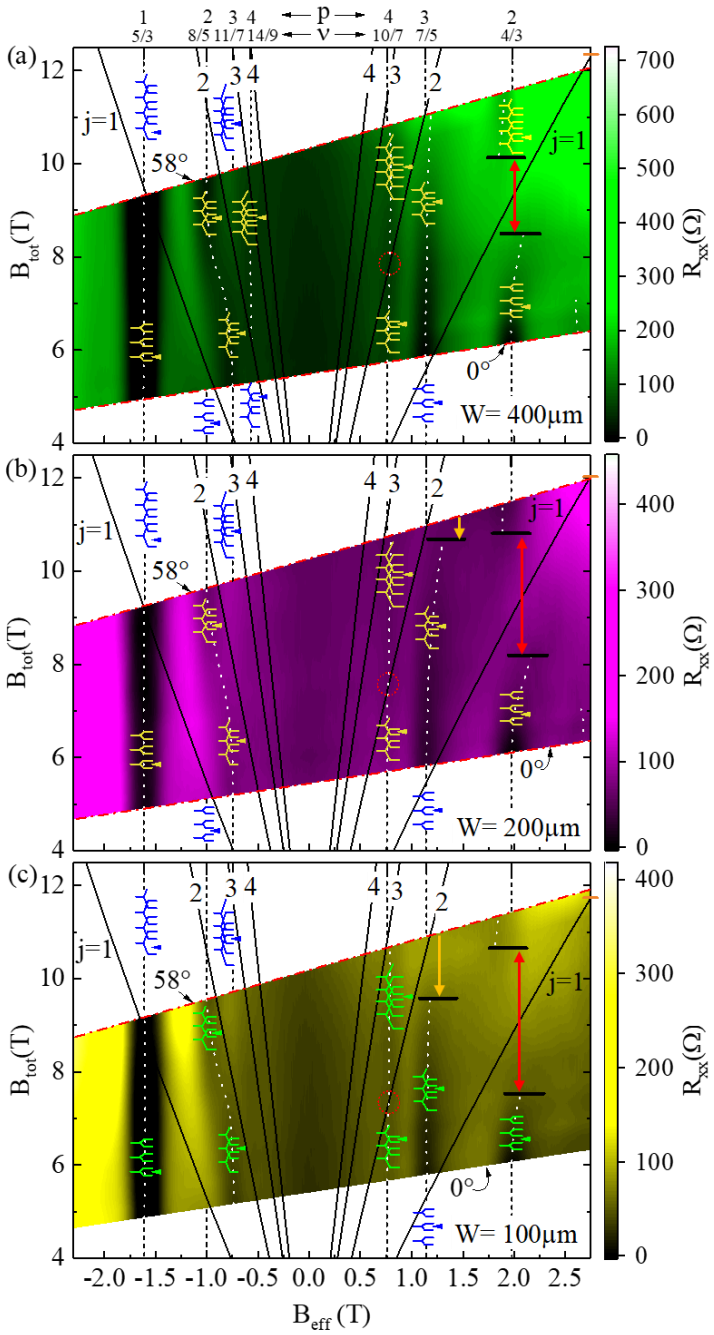


*Figure 3.17 $R_{xx}$ color plots with coincidence fan charts versus $B_{eff}$ and $B_{tot}$. (a), (b), and (c) depict color plots of $R_{xx}$ versus $B_{tot}$ for W = 400, 200, and 100 μm sections, respectively. The dotted lines follow the $R_{xx}$ minima. The dashed lines mark specified odd-denominator fractional fillings of Landau levels. The black curved lines show the trajectory of the Zeeman-Landau level (LL) coincidence condition in the $B_{tot}$ - $B_{eff}$ space. The CF-LL occupancy is indicated by the Landau level cartoons. The horizontal lines in black, with the colored vertical arrowed lines in red and yellow, mark the boundary of the size-dependent angular interval where the diagonal resistance minimum vanishes. Here, T = 55 mK. Reproduced from Wijewardena et al.,(2022)[2].*

That is, at coincidence, the $B_{tot} = jB_{eff}(2m_0/(g^*m^*))$, and the coincidence condition corresponds to lines in the $B_{tot} - B_{eff}$ space, whose slope depends on *j*[69]. Figure 3.17 we have displayed a color plot $R_{xx}$ versus $B_{tot}$ and $B_{eff}$ for the *W* = 400, 200, and 100 $\mu m$ sections. As in Figure 3.5, two different line types are used here: dotted lines within the colored regions identify the trajectory of the resistance minima, while dashed lines in the white regions inside the graphs mark rational odd-denominator filling factors. The size dependence in the tilt angle intervals for the vanishing of the $\nu = 4/3$ and $\nu = 7/5$ resistance minima, previously seen in Figure 3.5, are observable here over finite $B_{tot}$ intervals and marked with the vertical red and yellow arrowed lines, respectively. The center of the $B_{tot}$ interval where the 4/3 resistance minimum vanishes, for example, is equivalent to the point of maximum relative resistance utilized in the analysis by Du et al.[69]. Since this point of relative maximum resistance at 4/3 depends on device size, the fan charts and the associated parametric equation become dependent upon device size. Thus, $B_{tot} = jB_{eff}(2m_0/(g^*m^*))$ with, (a) $g^*m^*/2m_0 = 0.190 + 0.012(T^{-1})B_{eff}$ for the 400 $\mu m$ data, (b) $g^*m^*/2m_0 = 0.195 + 0.012(T^{-1})B_{eff}$ for the 200 $\mu m$ data, and (c) $g^*m^*/2m_0 = 0.201 + 0.012(T^{-1})B_{eff}$ for the 100 $\mu m$ data. In Figure 3.17, a manifestation of the size dependence of the fan charts is the variable ordinate-intercept of the $j = 1$ line at $B_{eff} = +2.75\ T$, which is marked with a short horizontal orange colored line. Notice that this intercept value decreases with decreasing *W*. For all three *W*, as mentioned, the $j = 1$ line passes through the middle of the $B_{tot}$ interval where the 4/3 resistance minima vanish. Similarly, the $j = 2$ line passes through the estimated center of the $B_{tot}$ where the 7/5 resistance minima vanish. Notice also that the $j = 2$ line crosses the dotted line marking the 10/7 resistance minimum. One might expect a vanishing of the 10/7 resistance minimum around the intersection of the $j = 2$ line and the 10/7, at the small dotted red circle. However, this is not observed in the data. That is, a spin

transition from one spin polarized 10/7 state to another is not observed in these data although it is suggested by the fan chart. Over the span $B_{eff} < 0$, the observable 14/9 resistance minimum falls between the $j = 2$ and $j = 3$ lines of coincidence for $W = 400\ \mu m$. Notice that the 14/9 minimum trajectory is only observable in Figure 3.17 (a), and not in Figure 3.17 (b) or (c). The 11/7 to 8/5 crossover, which is observable in panels Figure 3.17 (a-c), remains to be understood in the context of this CF-LL crossing plot. We remark, however, that the slope of the dotted line indicating the crossover is approximately the same as the slope of the neighboring $j = 2$ line. Du et al.[69] have used such level crossing analysis to determine the $B_{eff}$ -dependence of $g^*$ and $m^*/m$. Although a detailed analysis is beyond the scope of this work, we remark that, for $W = 400\ \mu m$, the results ($g^*m^*/2m_0 = 0.190 + 0.012(T^{-1})B_{eff}$) are also approximately consistent with $m^*/m = 0.65 + 0.00158\ B_{eff}$ and $g^* = 0.57 + 0.035\ B_{eff}$. This expression for $g^*$ suggests a value $g^* = 0.43$ at $\nu = 2$ and $g^* = 0.88$ at $\nu = 1$, which are consistent with expectations for observing a bare $g$-factor at $\nu = 2$, and an exchange enhanced value at $\nu = 1$.

So far as the observation of a size dependence of $g^*m^*$ is concerned, our result, that (a) $g^*m^*/2m_0 = 0.190 + 0.012(T^{-1})B_{eff}$ for the 400 $\mu m$ data, (b) $g^*m^*/2m_0 = 0.195 + 0.012(T^{-1})B_{eff}$ for the 200 $\mu m$ data, and (c) $g^*m^*/2m_0 = 0.201 + 0.012(T^{-1})B_{eff}$ for the 100 $\mu m$ data, represents a set of three parallel lines with the same slope ($0.012T^{-1}$) in a plot of $g^*m^*/2m_0$ versus $B_{eff}$. The question arises whether the observed size dependence should be attributed to a size dependent $g^*$ or $m^*$ or both. Consider first the $g^*$. The exchange enhanced spin gap can be written as: $\Delta_{spin} = g^*\mu_B B = g_0\mu_B B + E_{Ex}$, where $g^*(g_0)$ is the enhanced (bare) g-factor[74]. If overlapping Landau levels may be neglected, and at sufficiently low temperature, as in our experiments, one might simply write $E_{Ex} = (n^- - n^+)$, where Σ is a self-energy, and $n^-(n^+)$ are the concentrations in the two spin subbands[75]. Although the self energy Σ

can potentially be size dependent if the separation of an electron-hole pair becomes limited by the sample size[74], the exchange enhancement of the g-factor ought to vanish due to the concentration difference dependence of the exchange term, when the two spin subbands of the lowest Landau level are equally occupied as at $\nu = 2$. That is, one naively expects a size independent g-factor at $\nu = 2$. Yet, the results suggest a size dependent $g^*m^*$ even at $\nu = 2$. Due to this feature, and the simple parallel line behavior of $g^*m^*$ for the three sections, we suggest that the size dependence of $g^*m^*$ possibly originates from a size dependence to $m^*$only, with a larger $m^*$ in the smaller section of the sample. Since composite fermion masses are known to diverge as the filling factor approaches $\nu = 1/2$ and scale as $n^{1/2}$[76], perhaps it is plausible that it could also depend on the specimen size.

Finally, the tilt induced transformation of the 11/7 to the 8/5 with increasing angle Figure 3.6 (a, b) coincides with a decreasing activation energy for the 11/7 followed by an increasing activation energy for the 8/5 with increasing tilt angle, see Figure 3.12 (b). In reference to Figure 3.17, this feature suggests that the mobility gap at $p = 3\ (11/7)$ collapses as the mobility gap at $p = 2\ (8/5)$ becomes larger with increasing tilt angle. From the CF-LL scheme exhibited in Figure 3.17 the $p = 2\ (8/5)$ crossover from the unpolarized to polarized spin state over the corresponding $j = 1$ CF-LL line, see Figure 3.17, occurs close to $\theta = 0^{\circ}$. This suggests a possible collapsed gap at the outset, followed by a progressively stronger polarized spin state with an increasing mobility gap for the 8/5 for the entire range of experimentally accessible tilt angles. The CF-LL scheme exhibited in Figure 3.17 also suggests that $p = 3\ (11/7)$ corresponds to a partially polarized state at the outset, with a trajectory towards a crossing of the $j = 2$ CF-LL Line at the highest experimentally accessible angle, implying a decreasing activation energy with increasing angle. So, the observed trends in the activation energies, see Figure 3.12 (b), are not

inconsistent with Figure 3.17 although some expected crossovers (dotted red circles in Figure 3.17) are not manifested. The surprising feature here is, however, that one fractional state (11/7) is extinguished in favor of another (8/5) with increasing tilt. Since the associated filling factors are so close to each other, and resistance minima have a finite width in filling factor, it could be that, due to overlap and proximity, the stronger fraction simply competes against and consumes the weaker one, per experimental observation.

### 3.4 Conclusions

In summary, these results show that tuning the spin energy by tilting the specimen can produce fractional quantized Hall effect transformations that include both a change in $\nu$ for the $R_{xx}$ minimum, e.g., from the $\nu = 11/7$ to the $\nu = 8/5$, and a change in the $R_{xy}$, e.g., from $R_{xy}/R_K = (11/7)^{-1}$ to $R_{xy}/R_K = (8/5)^{-1}$, with increasing tilt angle. Further, the results showed a striking size dependence in the tilt angle interval for the vanishing of the 4/3 and 7/5 states, and concurrent observable shifts of $R_{xy}$ at the $R_{xx}$ minima- the latter occurring in the vicinity of $\nu = 4/3, 7/5$ and the 10/7, see Figure 3.5 (b), (d), and (f). The results demonstrate both size dependence in the FQHE regime and the possibility, not just of competition between different spin polarized states at the same $\nu$ and $R_{xy}$, but also the tilt or Zeeman-energy-dependent-crossover between distinct and different FQHE.

# 4 FABRICATION OF GRAPHENE DEVICES

Graphene, a two-dimensional crystal structure composed of a single layer of carbon atoms arranged in a honeycomb lattice, has garnered significant attention recently due to its extraordinary properties and wide-ranging potential applications[40, 77-82]. With an impressive strength-to-weight ratio, graphene is considered the thinnest and strongest material known, surpassing even steel[83]. Its exceptional electrical properties make it a highly efficient conductor of electricity, with electrons moving at velocities 100 times faster than in traditional semiconductors[77]. Moreover, graphene exhibits remarkable thermal conductivity, outperforming materials like copper and diamond, which makes it a promising candidate for heat dissipation applications[84].

The unique combination of its mechanical, electrical, and thermal properties has opened a broad spectrum of potential applications for graphene. In the field of electronics, graphene-based transistors have shown promise in enabling faster and more energy-efficient devices[77, 85]. Its exceptional strength and flexibility make it an ideal material for creating flexible and transparent electronic displays, wearable devices, and even biomedical sensors[85, 86]. Graphene has also found applications in energy storage, such as high-performance batteries and supercapacitors, due to its large surface area and excellent charge storage capacity[87]. Furthermore, the unique properties of graphene have led to advancements in composite materials, enabling the development of stronger and lighter materials for aerospace and automotive industries[88]. As researchers continue to explore and unlock the full potential of graphene, its exceptional properties offer a myriad of possibilities for technological advancements in various domains.

Even though graphene has been subjected to research for several decades, yet producing defect-free pure graphene is still challenging. Chemical Vapor Deposition (CVD) is one of the

popular methods available for graphene production[89, 90]. Another popular method, which produces much cleaner samples, is based on using naturally formed bulk material as the source and performing mechanical exfoliation. The method got widely popular after the successful isolation of a good graphene sample by Geim and Novoseleov using scotch tapes[91]. This work won them the Nobel prize in physics in the year 2010. The method has proven to be very successful in producing single layers of graphene, yet the size of graphene obtained from this method is smaller than the CVD method.

## 4.1 Exfoliation of 2D-materials

2D-layered materials consist of layers attached by Van der Waals forces[92]. These bonds between the layers can be broken very easily than the other types of bonds within the atoms in materials. Therefore, removing or peeling off a layer is easier if one can apply the correct magnitude of the force in the correct direction. When the magnitude and direction of the force are not ideal, the material layers can get broken, resulting in smaller flakes, or multiple layers will peel off instead of one layer[93]. This process is somewhat similar to peeling off an onion. Since the bulk materials and the layers involved with the mechanical exfoliation are on a microscopic scale, the process is complicated.

When it comes to graphene, natural graphite pieces consist of thousands of graphene layers. Placing such a piece on scotch tape and folding the tape over the graphite and pushing on it will attach the topmost and bottom-most parts of the graphite piece on the tape. When peeling off the tape, the graphite piece will break free from layers somewhere in the middle, resulting in two graphite pieces on the scotch tape. The attraction between the scotch tape and the graphite surface is stronger than the attractive forces among the graphene layers in between. Due to this reason, graphene layers are forced to separate when peeled off by hand. This process can be

carried out multiple times using different places in the same scotch tape that results in a spread of graphene and graphite pieces on the scotch tape.

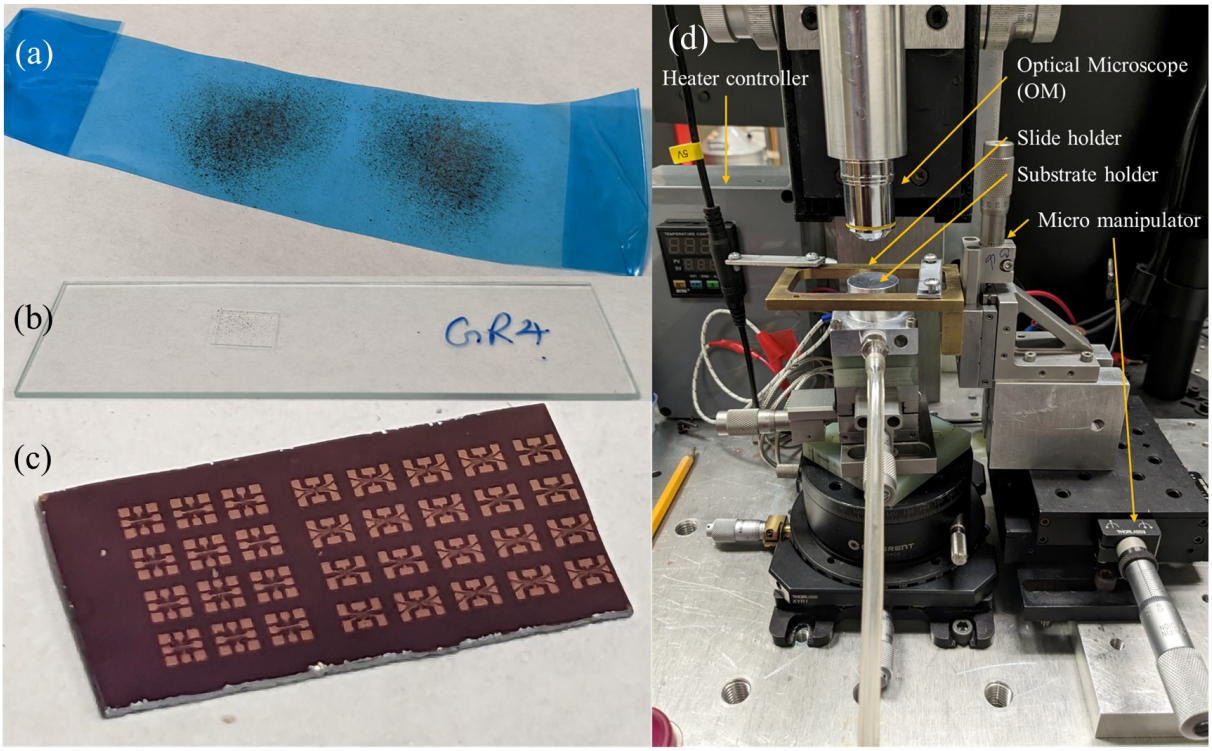


*Figure 4.1 Preparation of a graphene device using exfoliation techniques. (a) Adhesive tape used for exfoliating graphene from a graphite flake. (b) Glass slide with a piece of Polydimethylsiloxane (PDMS) used for extracting exfoliated graphene from the adhesive tape. (c) Silicon chip with 32 different patterns of metal contacts used for device fabrications. (d) Dry transfer setup used for transferring graphene flakes on PDMS to a targeted substrate.*

The graphene graphite mixture on the tape can be seen as a cloud of black color dust as shown in Figure 4.1 (a). This tape contains an exfoliated mixture that can be transferred onto a piece of Polydimethylsiloxane (PDMS) to identify good graphene layers. For this process, a properly cleaned glass slide is used to attach a PDMS piece (see Figure 4.1 (b)). Then, the scotch tape with the exfoliated mixture is placed on the PDMS. Applying pressure on the scotch tape attached to the PDMS will transfer exfoliated flakes onto the PDMS. Transferred graphene flakes can be identified using an Optical Microscope (OM). Identified graphene flakes can be

transferred on to a silicon wafer with metal contact pads (see Figure 4.1 (c)) in order to make magneto transport measurements. Figure 4.1 (d) shows the dry transfer setup used for transferring graphene and other 2D-materials on to a targeted substrate.

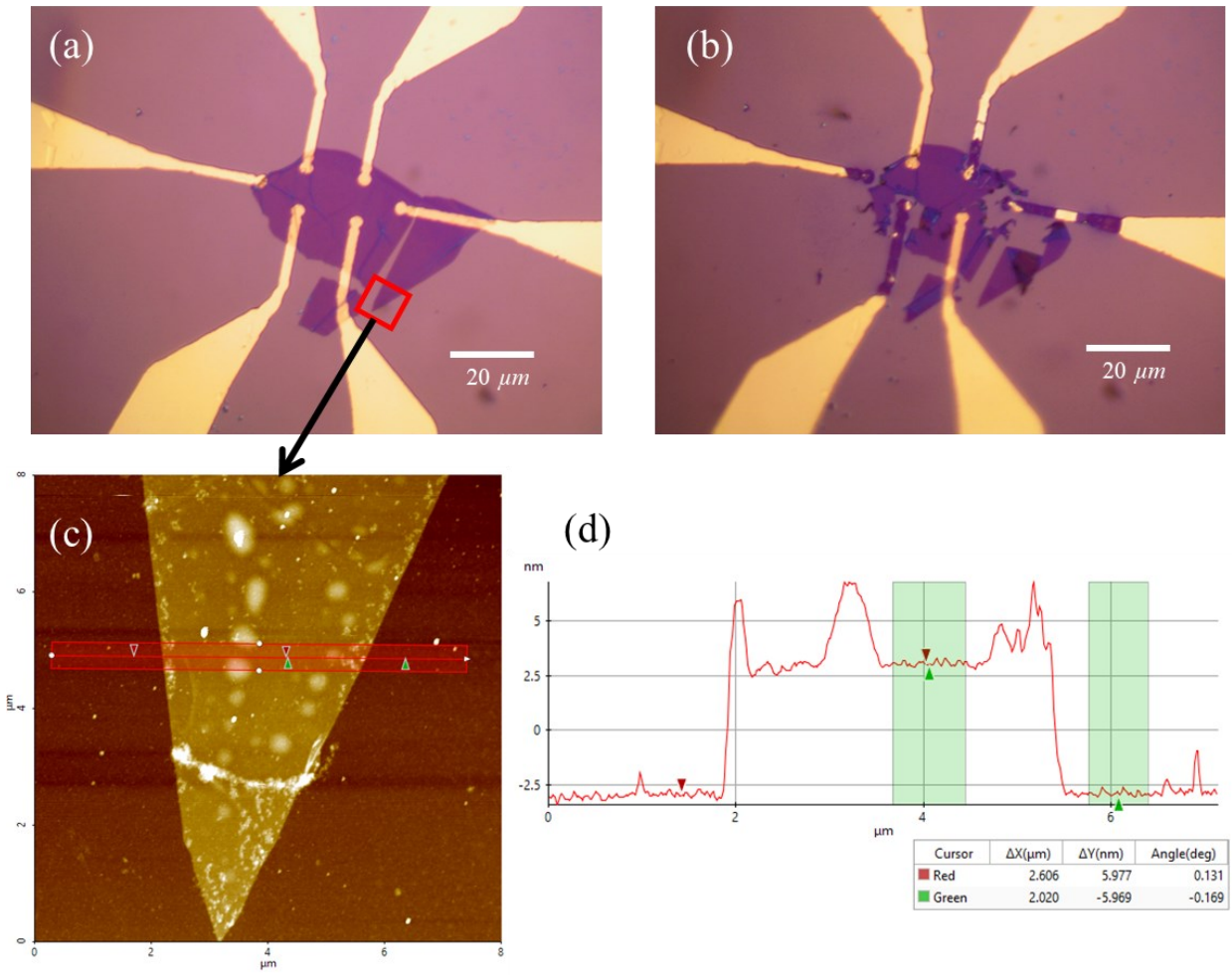


*Figure 4.2 Multi-layer graphene device fabricated using exfoliation and dry transfer techniques. (a) OM image of the device taken prior to transport measurements. (b) OM image of the device taken after transport measurements, showing damage caused by a static electric shock. (c) & (d) AFM scan conducted in the red rectangle shown in (a) and the associated height profile.*

The Figure 4.2 illustrates a multi-layer graphene device fabricated utilizing such exfoliation and dry transfer techniques. In Figure 4.2 (a) and (b), OM images captured before and after performing electrical transport measurements and experiencing a static electric shock are presented. Due to their small size, these devices are particularly susceptible to static electric

shocks. Therefore, it is essential to employ surge protection for the measurement channels to ensure their safety. Figure 4.2 (c) and (d) depict an Atomic Force Microscope (AFM) image of a specific region of the specimen and its corresponding height profile. The interlayer distance in bulk graphite is about 0.335 nm [91]. In Figure 4.2 (d), the thickness of the multi-layer graphene measures around 6 nm, indicating the presence of not more than 17 layers of graphene in the device. However, it is important to note that there could be air trapped beneath the graphene, which could contribute to the overall height and introduce measurement errors. Therefore, it is reasonable to assume that the device contains approximately 10 to 15 layers of graphene.

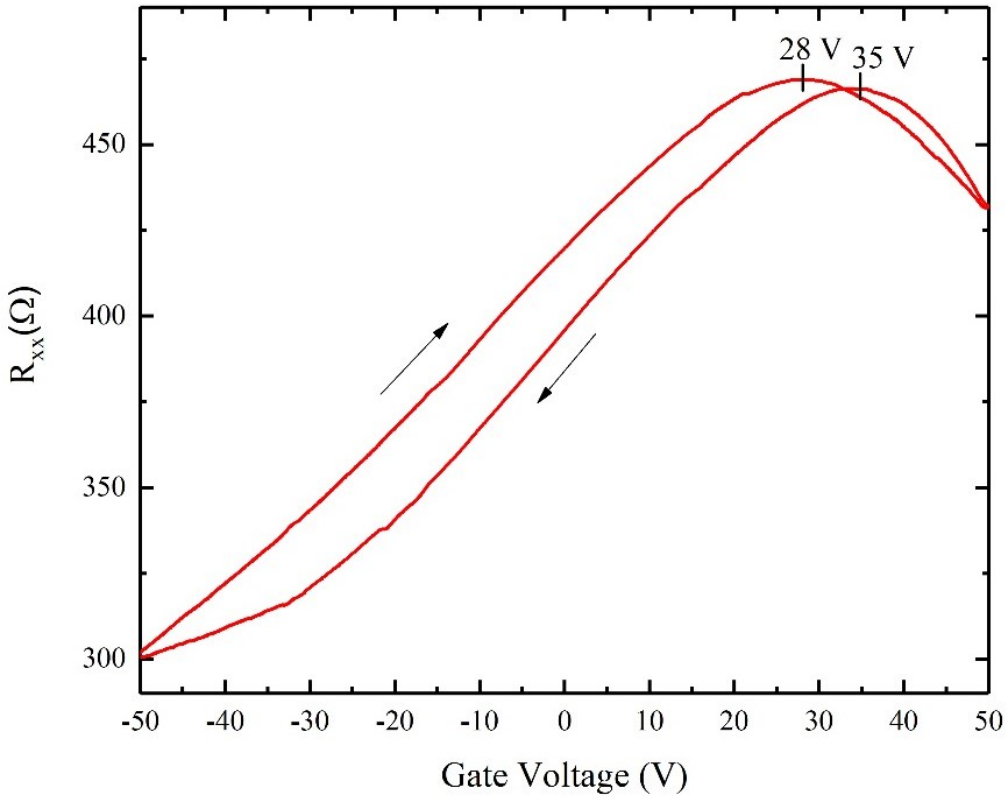


*Figure 4.3 Diagonal resistance ($R_{xx}$) as a function of back gate voltage in a multilayer graphene device with 10-15 layers. The charge neutrality point (CNP) is shifted towards higher gate voltage, indicating p-type behavior. The presence of hysteresis effect is observed by the shift between the up and down sweep curves. Measurements were conducted at room temperature.*

When conducting transport measurements on the device and measuring the diagonal resistance against the applied back gate voltage, a broadened peak was observed near the charge

neutrality point (CNP) in multi-layer graphene (see Figure 4.3). In contrast, single-layer graphene would exhibit a sharp peak in this measurement.

In single-layer graphene, the resistance plotted against the backgate voltage typically shows a symmetric and distinct peak known as the Dirac point. At this point, the Fermi level aligns with the Dirac point, resulting in an electrically neutral graphene sheet. However, in multi-layer graphene, the presence of multiple graphene layers introduces additional electronic states and interlayer coupling effects. This leads to a more complex band structure with multiple sets of Dirac cones. The interlayer coupling causes modifications in the electronic properties, resulting in a broadened resistance peak in the backgate voltage curve.

Several factors contribute to the broadening of the peak. These include interlayer coupling-induced band hybridization, increased charge transfer between layers, and the presence of additional scattering mechanisms. As a result, the resistance peak in the backgate voltage curve appears smeared or broadened compared to the sharper peak observed in single-layer graphene.

In Figure 4.4, several OM images are presented, showcasing a multi-layer graphene sample with h-BN coverage. This sample was fabricated using exfoliation and dry transfer techniques. One notable advantage of employing an h-BN cover for a graphene sample lies in its ability to shield the graphene from the surrounding environment[94].

Graphene, being a two-dimensional material consisting of a single layer of carbon atoms, is highly susceptible to various environmental factors such as moisture, oxygen, and contaminants. These external influences can significantly affect the electrical and structural properties of graphene, leading to performance degradation. By introducing a protective layer of hexagonal boron nitride (h-BN) on top of the graphene, the h-BN cover acts as a barrier, effectively

isolating the graphene from the external environment. h-BN is known for its excellent insulating and impermeable properties, providing an ideal protective enclosure for graphene[94-96]. Therefore, having a protective layer of an insulating material improves the quality of graphene significantly [97].

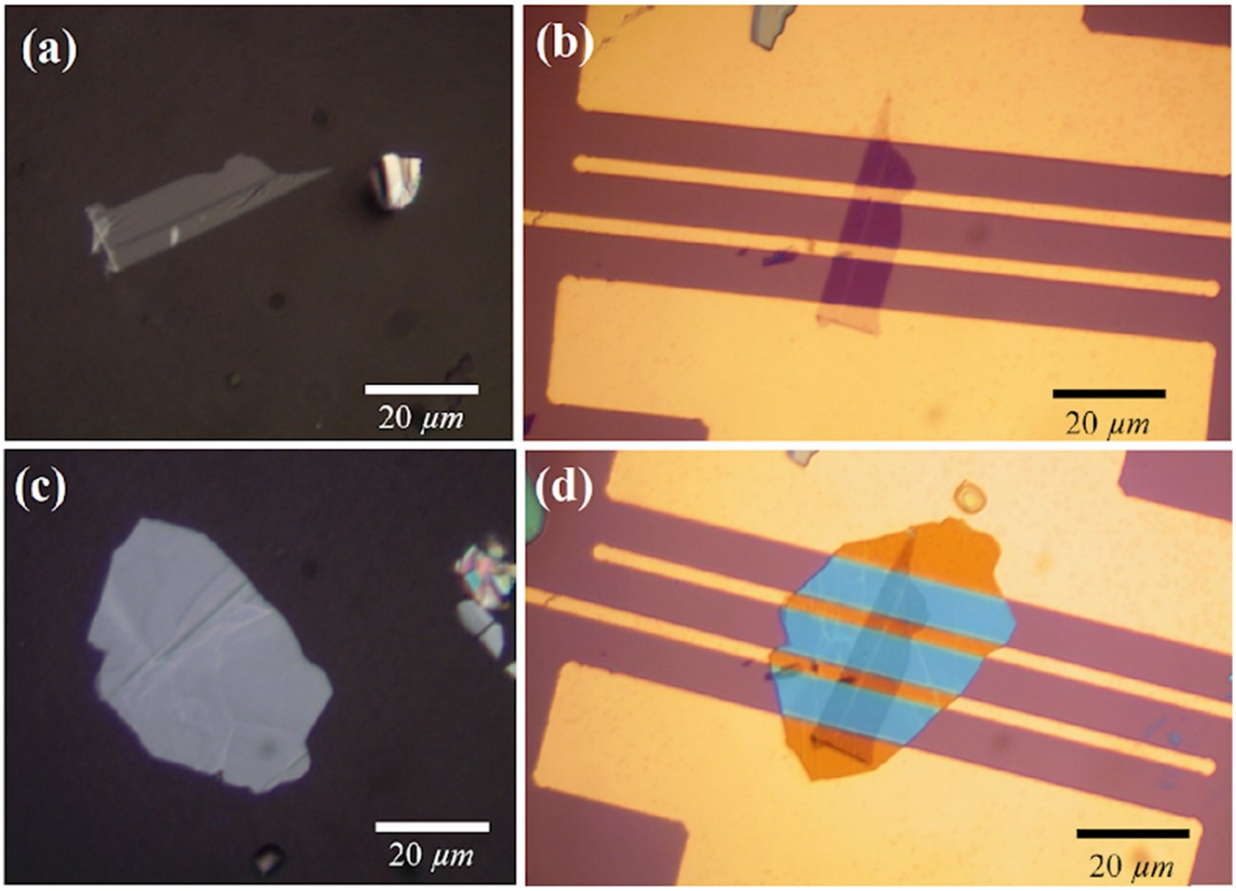


*Figure 4.4 Optical microscope (OM) images captured during the dry transfer process for fabricating a multi-layer graphene sample with a h-BN flake covering. (a) Multi-layer graphene flake on PDMS. (b) Graphene flake transferred on to a gold contact pattern. (c) few layers of h-BN flake on PDMS. (d) Multi-layer graphene flake on gold contact pads covered by h-BN.*

Transport measurements were conducted on the h-BN capped multilayer graphene device shown in Figure 4.4. The results are presented in Figure 4.5 (a), which illustrates the charge neutrality point (CNP) during the forward sweep around a back gate voltage of 14V. Remarkably, the CNP observed in this device is significantly improved compared to the CNP of

the bare multilayer graphene sample, which was 28V (see Figure 4.3). Additionally, Figure 4.5 (b) displays the effect of annealing the device with a 20 μA AC current for 40 minutes. A shift of approximately 5V towards the zero-gate voltage is observed. This shift suggests that further annealing could potentially enhance the quality of the device even more.

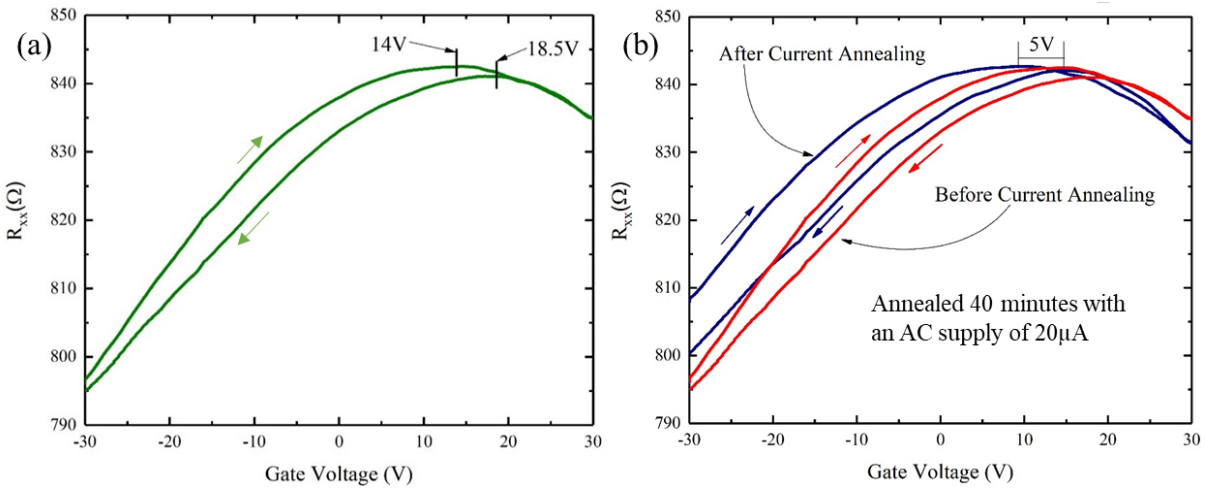


*Figure 4.5 Transport measurements and the effect of current annealing in an h-BN capped multilayer graphene device conducted at room temperature. (a) Diagonal resistance ($R_{xx}$) as a function of back gate voltage in the device, displaying both up and down sweep curves of the back gate voltage. (b) The difference in the device's behavior before and after annealing for 40 minutes with an AC supply of 20 μA.*

Furthermore, this highly sensitive graphene can be incorporated in creating new heterostructure electronic devices by stacking another 2D material like $MoS_2$, $WSe_2$, or h-BN on top of each other like a sandwich [98]. Creating these types of samples highly depends on obtaining large enough 2D material layers that can easily be stacked on top of each other. The size of the 2D flakes produced by the traditional mechanical exfoliation may not be sufficient to create a suitable device for electrical measurements. Therefore, finding a method that can be used to obtain large flakes of 2D materials is crucial for developing such Nano-electronic devices. While CVD techniques offer the advantage of generating sizable flakes of 2D-materials, ensuring the high quality of the grown material poses a significant challenge[99].

## 4.2 Chemical Vapor Deposition of graphene

CVD techniques have gained popularity as a viable approach for producing sizable graphene samples of commendable quality. Furthermore, this method offers the advantage of relatively lower production costs. The CVD method uses an enclosed quartz tube connected to several gas sources and a vacuum pump that can provide essential elements and conditions for the growth of desired material. Figure 4.6 shows a schematic diagram of such a setup. The quartz tube is placed in a furnace that can be heated to a temperature around 1000℃. CVD systems of this kind typically offer precise control over gas pressure and temperature, ensuring uniform growth of the desired material on a suitable substrate surface.

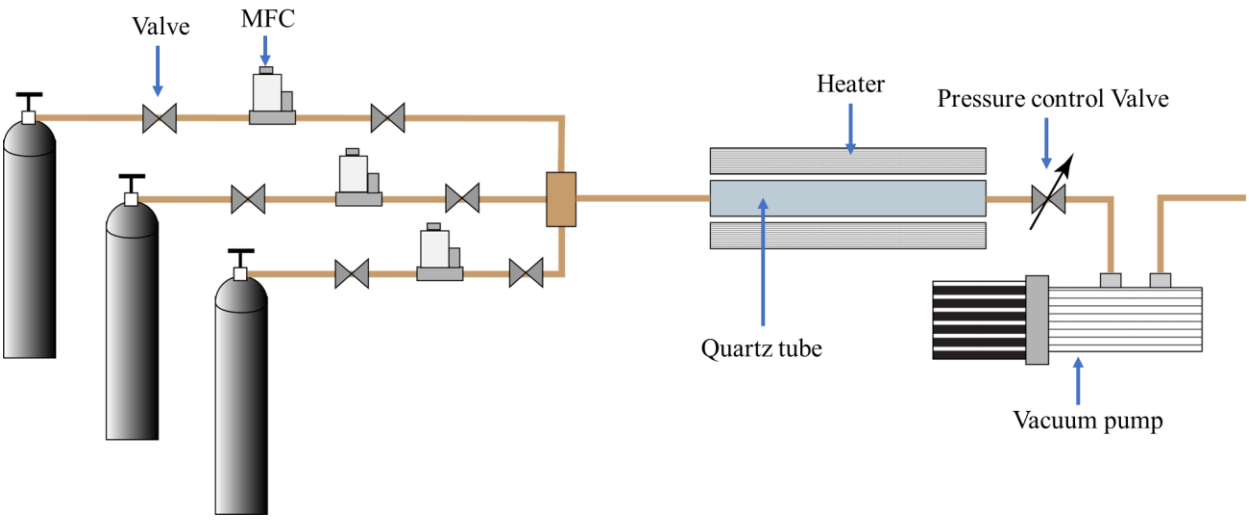


*Figure 4.6 An illustration of typical CVD system. Regulated gas flow from high pressure tanks further control by Mass Flow Controller (MFC)s and the sent to a Quartz tube reactor. External heaters increase the temperature of the reactor for the chemical deposition. The vacuum pump removes the exhaust gas.[100]*

In the deposition process of graphene, a precursor such as $CH_4$ is utilized as a carbon source[101-103]. To facilitate the decomposition of the precursor and initiate nucleation of graphene crystals, a catalyst thin film or foils, such as cobalt[104], nickel[105], or copper[106,

107], are employed for support. Figure 4.7 depicts the typical growth profile of graphene via LPCVD.

The production of graphene on a metal catalyst is influenced by several key factors. These include the carbon solubility limit within the metal, the metal's crystallographic parameters, and various thermodynamic variables like growth temperature and pressure. These elements play a significant role in shaping the synthesis process of graphene on a metal catalyst[101].

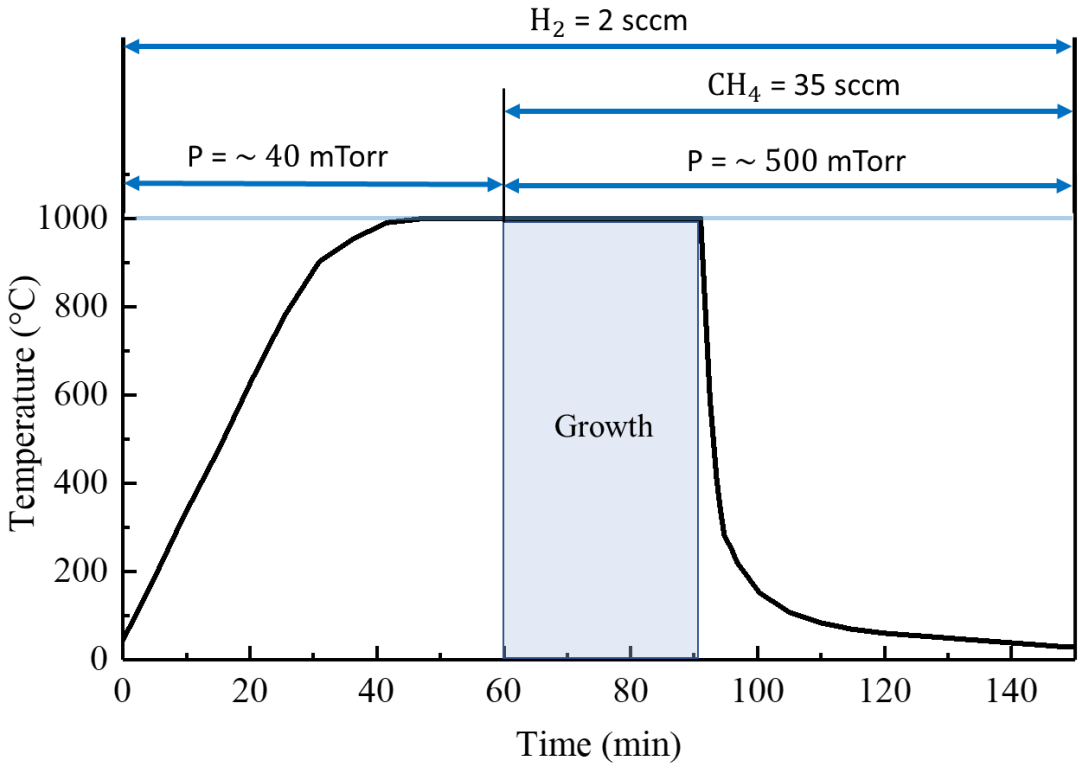


*Figure 4.7 Growth profile of a typical low pressure chemical vapor deposition of graphene.*

The method of growing graphene on copper has gained more attention due to copper's low carbon solubility as a catalyst, which restricts the growth process to the catalyst's surface[108-110]. Typically, the growth of graphene on a copper surface is self-limiting, resulting in the formation of a single layer of graphene[111-113]. This limitation arises because the decomposition of the carbon precursor is not favorable on existing graphene layers[113].

However, there have been reports of few-layer growth of graphene on copper, indicating that under specific conditions such as higher methane concentration[114] and impurity-induced growth[115], the self-limiting effect can be overcome[116, 117].

It is worth noting that graphene grown on copper exhibits a polycrystalline structure on a micrometer scale, which is a consequence of the growth process. The CVD process for growing graphene involves the formation of stable nuclei, which subsequently grow and merge at the grain boundaries, leading to the polycrystalline nature of the graphene produced on copper. This polycrystalline morphology poses challenges for graphene applications as it negatively impacts the quality of the material.

Therefore, it is crucial to develop growth techniques that minimize the density and orientation of two-dimensional grain boundaries in order to produce high-quality single crystal graphene[102, 103, 118, 119]. Extensive research has been dedicated to achieving precise and controlled growth of high-quality graphene. Various techniques have been explored to advance this goal, including seeded growth techniques[120], substrate electro-polishing[121, 122], oxygen, plasma, and proton-assisted CVD growth methods[123-127]. These approaches aim to enhance the quality and control of graphene growth, opening new possibilities for its applications.

# 5 CURRENT ANNEALING CVD GRAPHENE

Graphene is one of the most popular 2D materials.[78, 128-131] It is semimetallic and, has charge carriers that behave like Dirac fermions (zero effective mass)[78]. Graphene also shows high mobilities up to 200,000 $cm^2V^{-1}s^{-1}$ [128], and many other extraordinary effects. Half-integer quantum Hall effect[132] and ballistic transport properties at room temperature[129] are a few examples. Production of high-frequency electronic devices[130] and transparent low resistance conductors[133] will be feasible due to high carrier mobility and lower visible light absorption of graphene.

Obtaining disorder free graphene is essential and investigating the obstacles for doing that is crucial for the future of nanotechnology. The highest quality graphene with minimum structural defects are achieved by mechanical exfoliation of pyrolytic graphite[134]. However, the exfoliation method cannot be utilized in creating large-area monolayer graphene. Therefore, a method that can fabricate uniform monolayer graphene in large scale is required. Chemical Vapor Deposition (CVD) of graphene was demonstrated as a method of growing single-layer graphene [135]. It has been shown that large area of single-crystal, monolayer graphene (0.5 mm on a side) can be grown with good control, on copper foils[136, 137].

The problem with CVD graphene is the process-induced impurities and defects. Such defects would make our samples inhomogeneous, causing the transport properties to deviate from what we expect theoretically for ideal graphene. Since graphene is a zero bandgap semi-conductor, conversion of dominant carrier type can be induced using a gate bias. The conversion from holes to electrons happens without crossing a bandgap [138]. Having the Fermi level at the Dirac point would mean there is no net carrier density. Therefore, one can expect diverging Hall resistance and diagonal resistivity. However, experimental observations suggest that holes and

electrons undergo ambipolar transport over a wide range of gate voltage near the Charge Neutrality Point (CNP) of CVD monolayer graphene. This observation was explained by the formation of electron-hole streams [139] or puddles [140] at the Dirac point, that arise due to impurities or graphene ripples [141].

## 5.1 Impurities in CVD graphene

Graphene transferred on to silicon dioxide substrates are found to be p-type in most cases due to doping by unintentional adsorbates[142]. Clean mono-layer graphene is considered hydrophilic [143]. Graphene placed on a defective substrate (i.e., $SiO_2$), is more likely to be affected by water and that the underlying substrate can influence the transport properties of graphene significantly [144]. At ambient conditions, molecules like water and oxygen can easily interact with the underlying substrate since the graphene is only a single atomic layer. Once the sample is exposed to ambient conditions, the doping state remains unchanged even in a vacuum.

The traditional wet transfer method used to transfer graphene grown on copper to the substrate can leave metal ions such as $Cu^{2+}$ and $Fe^{3+}$ trapped between the graphene layer and the substrate. The copper layer is typically etched by oxidant solutions such as iron (III) nitrate [145] iron (III) chloride [146] and then cleaned by distilled water. Even after cleaning several times, there can be $Fe^{3+}$ ions that could contaminate the graphene [101].

### *5.1.1 Influence of impurities to the transport properties of graphene*

Impurities influence the transport properties of graphene through several mechanisms. Silicon dioxide ($SiO_2$) forms silanol bonds (Si-OH) on its surface in ambient conditions. Oxygen and water molecules that are close to the graphene $SiO_2$ interface will undergo a chemical redox reaction by trapping and de-trapping electrons [147]. If there is an applied electric field (Gate bias), electron trapping, or de-trapping can be stimulated based on the polarity of the field.

Adsorbed water molecules will act as dipoles that are oriented randomly. In an applied electric field, these dipoles will align themselves along the electric field direction, which will create a capacitive gating effect locally [142].

Ions that are trapped in the interface can drift through the $SiO_2$ at higher temperatures [148]. The movement of these ions will vary the distance to the graphene layer leading to a change in the localized gating effect. Figure 5.1 (a) demonstrates that the gating effect occurs due to water dipole and charged impurities. The combination of localized gating and charge trapping de-trapping effects emerge as the hysteresis in CVD graphene samples[149].

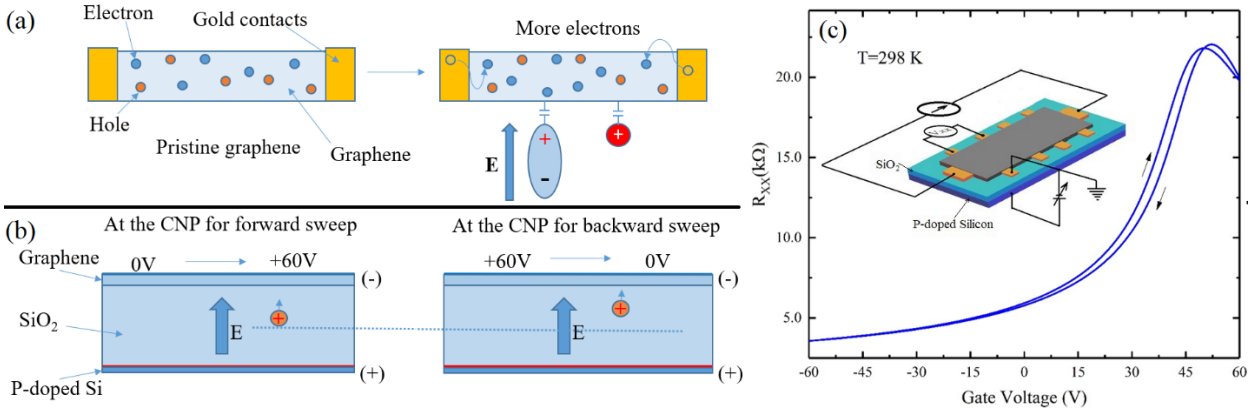


*Figure 5.1. Gate hysteresis effect in CVD graphene on $SiO_2$ substrate. (a) Electrostatic gating effect caused by water and charged impurities in an applied electric field. (b) Hysteresis caused by impurity migration through the $SiO_2$ substrate due to an applied electric field. The figure demonstrates an instance where the gate voltage is at the charge neutrality point for the forward and backward sweep from the left and right figures respectively. Note that the position of the charged impurity is different in two situations. (c) Typical hysteresis loop of a p-type graphene sample at room temperature where the diagonal resistance is measured against the gate voltage in a range of -60V to +60V as a loop. Inset shows the measurement configuration of the graphene sample. Reproduced with permission from Springer Nature [150].*

Figure 5.1 (b) explains the hysteresis using the drift of a positively charged impurity through $SiO_2$ in an applied electric field. Here, we consider the voltage that we observe at the charge neutrality point while forward and backward sweeping the gate voltage (GV). The impurity is at a different location while backward sweeping than it was in forward sweeping the GV.

Therefore, the influence of impurity is different. A typical hysteresis loop for a p-type graphene sample is shown in Figure 5.1 (c).

## 5.2 Annealing CVD graphene with a DC current.

Here we investigate the influence of long-time current annealing on the hysteresis effect and carrier transport of graphene specimen grown by the standard CVD method. We also demonstrate that the charge neutrality gate voltage can be controlled by cooling the sample with gate bias. Further, we study the effect of current annealing to the controllable range of CNP. The monolayer graphene was grown on 25 μm copper foils by chemical vapor deposition using a methane and hydrogen mixture as carbon precursor at about 1000° Celsius [135]. The graphene was transferred onto a 500 μm p-doped silicon wafer (100) with 285 nm of oxide layer using conventional wet transfer method [146]. Here we used millimeter-scale Hall bar devices with p-doped silicon as the back gate in the configuration depicted as in the inset of Figure 5.1 (c).

A closed-cycle refrigerator was utilized for the experiment. The sample was kept under vacuum for two days prior to the start of measurements using a turbo molecular pump ($10^{-5}Torr$). We can assume that most of the water molecules and other adsorbents are removed by pumping. The dominant effect will be from charge trapping (ionic impurities/ substrate trap sites). We studied the temperature and anneal-current dependence of the gate hysteresis effect. Samples were annealed for 10 hours with annealing currents of 100 μA, 1.5 mA, and 2 mA. The sample was held at a fixed $-$ 60 V back gate bias in order to create electron deficiency on graphene. We were able to cool the specimen to 35 K within four hours. A sweep rate of 0.2 V/s and a range of ± 60 V was used to sweep the back-gate voltage. To get an idea about the time frame for charge trapping and de-trapping, we carried out several hysteresis loops with different

wait time at + 60 V. A direct current of 10 μA was supplied to the sample, and the diagonal voltages were measured using digital multimeters.

Initially, we measured the hysteresis loops of our hall bar device at room temperature. As shown in Figure 5.2 (a), the back-gate voltage was cycled from − 60 V to + 60 V and then back to − 60 V without any delay at + 60 V for a first gate bias sweep, and then with a delay of 5, 10 and 15 minutes for subsequent sweeps. The results are shown in solid (orange), dotted (green), dashed (blue) and dotted dashed (red) lines respectively. Inset shows an enlarged portion from the region near the charge neutrality point. The difference between the gate voltage at the CNP for the forward and backward sweeps is an indication of hysteresis. When the wait time increases, the voltage difference between the CNP for forward and backward sweep also shows an increasing pattern. The voltage difference was 2.1 V for the data collected without any delay at + 60 V. Then the difference increased to 3.8 V and 4.5 V after waiting for 5 and 10 minutes at + 60 V respectively. It appears that the difference between up-sweep and down-sweep CNP's is not changing much after 10 minutes.

The hysteresis we observed here can be explained by charge trapping and de-trapping at the $SiO_2$-graphene interface and the top surface of graphene. When we are at a positive gate voltage, the electron concentration on graphene is higher compared to the holes. Trapping centers will trap electrons and reduce the effective electron concentration on graphene. This will reduce the effective gate voltage, moving the CNP to a more positive voltage. Similarly, the effect of a negative gate voltage can be explained as trapping and de-trapping of holes. Trapped charges will remain trapped until the polarity of the gate is switched. Silicon dioxide has silanol groups on the surface that act as charge traps. Thermally grown $SiO_2$ has effective trap density of about $5\times10^{10}$ $cm^{-2}$ interface traps and about $5\times10^{11}$ $cm^{-2}$ oxide traps [142].

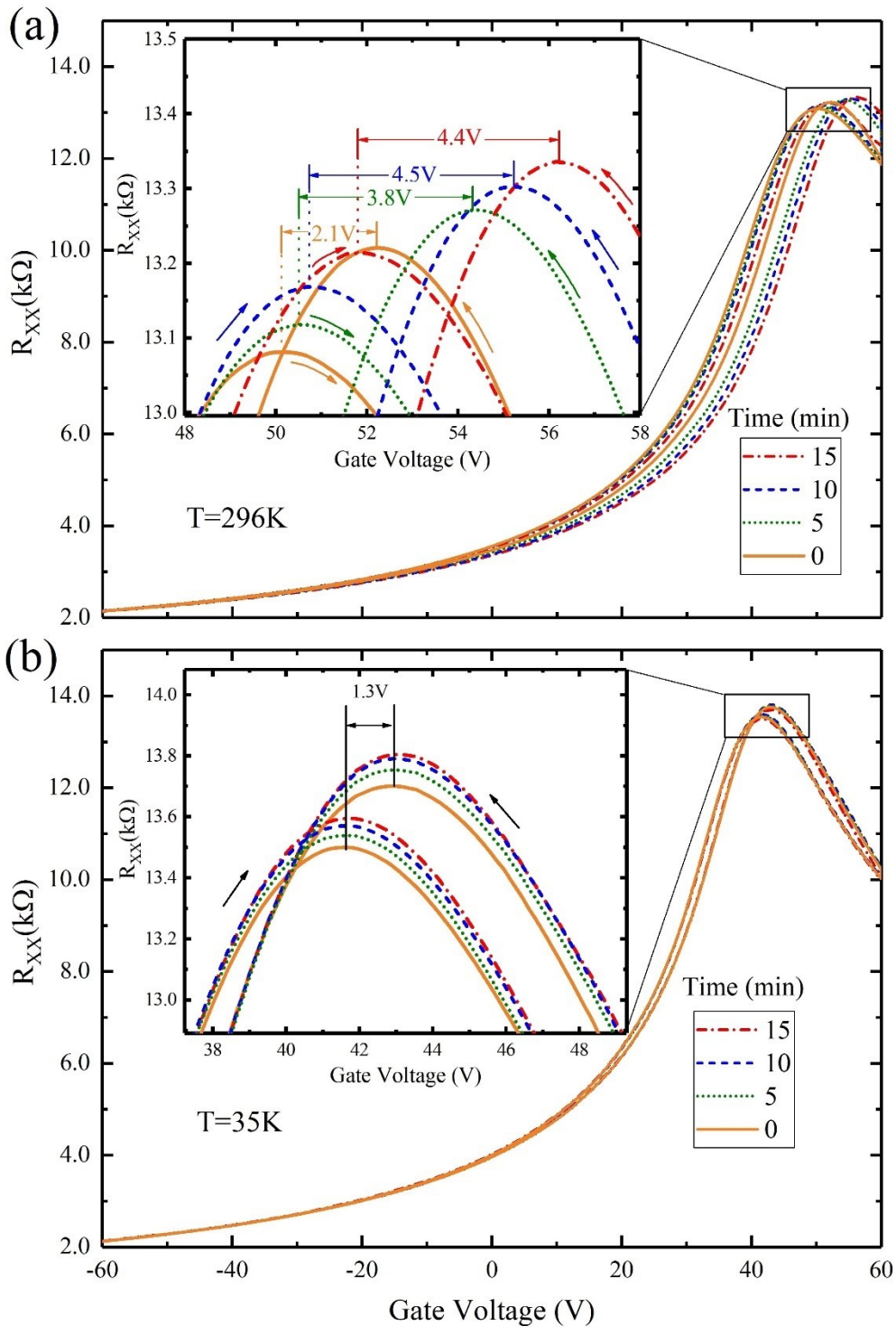


*Figure 5.2. Hysteresis loops with different wait times at +60 V GV at (a) room temperature and (b) 35 K. Diagonal resistance ($R_{xx}$) vs. the gate voltage for the wait times of 0, 5, 10 and 15 minutes at +60 V is shown in solid (orange), dotted (green), dashed (blue) and dotted dashed (red) lines respectively. Inset is a zoomed-in figure of the plot near the charge neutrality point in all the curves. Reproduced with permission from Springer Nature [150].*

We observed a reduction of hysteresis with reduced temperature. Figure 5.2 (b) shows that the difference between the gate voltage of CNP for the forward and backward sweep at the temperature of 35 K is 1.3 V which is smaller than what we observed at the room temperature. There is no observable difference between the data collected with different wait times at + 60 V that may be due to the prolonged time constant of charge trapping and de-trapping mechanism at lower temperatures. However, the observation of 1.3 V difference between the CNP for forward and backward sweeping indicates there is something that changed the effective gate voltage quickly even at 35 K. Since we did not change the polarity of gate voltage and only change the magnitude until we reach 0 V from + 60 V, we cannot reason this observation as an effect of dipolar impurities such as water or ice. The number of electrons or holes trapped by the silanol traps near the graphene $SiO_2$ interface can be increased or decreased based on the magnitude of the applied electric field [151]. However, we must investigate this further to have a better understanding.

We started current annealing the graphene Hall bar device with 100 μA DC supply. We annealed the sample for 10 hours in order to study the effects of long-time current annealing to the carrier transport. Figure 5.3 (a) demonstrates the hysteresis loops at room temperature before and after annealing by a solid (blue) and dotted dashed line (red) respectively. If we consider the gate bias we observed the CNP for the forward sweep, it was 44.5 V before annealing and is reduced to 37 V afterward. So, the annealing shifted the CNP toward the zero gate-voltage direction. Which means, the sample became less p-type. However, the difference between the CNP gate voltage for forward and the backward sweep was 2.4 V before, and the value increased to 5.6 V after annealing. This is an indication of a significant increase in hysteresis.

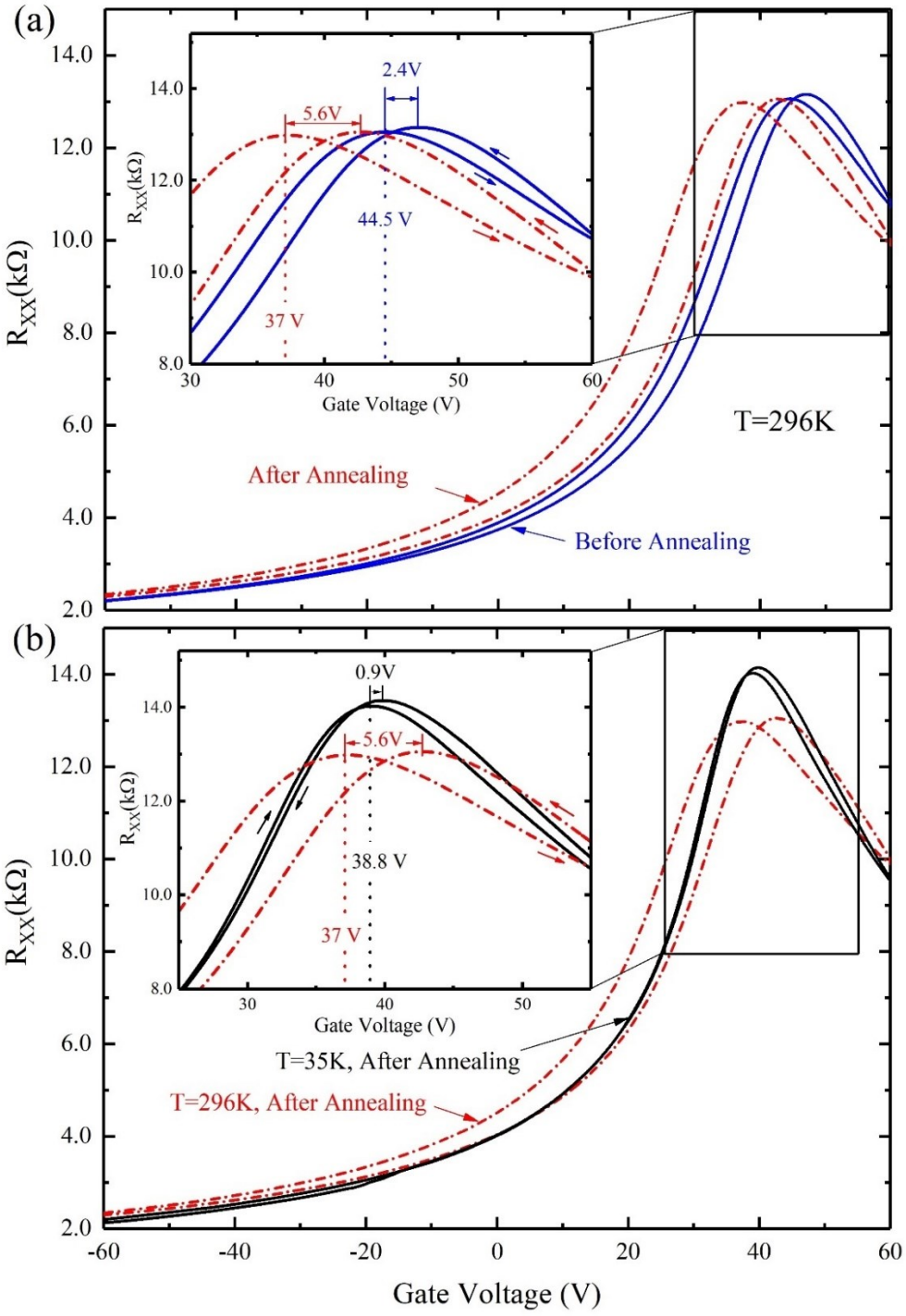


*Figure 5.3. Hysteresis loops after annealing the sample for 10 hours with 100 μA DC supply. Diagonal resistance ($R_{xx}$) is plotted against the back gate voltage, before annealing the sample in (a) solid (blue) line and after annealing in dashed-dotted line (red) in both (a) & (b) at the room temperature, (b) dotted dashed (red) line represent the data collected at 35 K after the annealing. Inset is a zoomed-in figure of the curves near the charge neutrality point. Reproduced with permission from Springer Nature [150].*

Figure 5.3 (b) shows the diagonal resistance ($R_{xx}$) plotted against the back-gate voltage after the current annealing at room temperature in the dotted dashed line and 35 K in solid (black) line. CNP voltage for the forward sweep at room temperature was 37 V, and it increased slightly to 38.8 V when cooled. The difference between the CNP voltage for the forward and backward sweep decreased to 0.9 V, which indicates a significant reduction of hysteresis. The increase of the CNP voltage observed at low temperature compared to the room temperature may be due to trapped charges within the surface or bulk charge traps during the sweep performed at the room temperature.

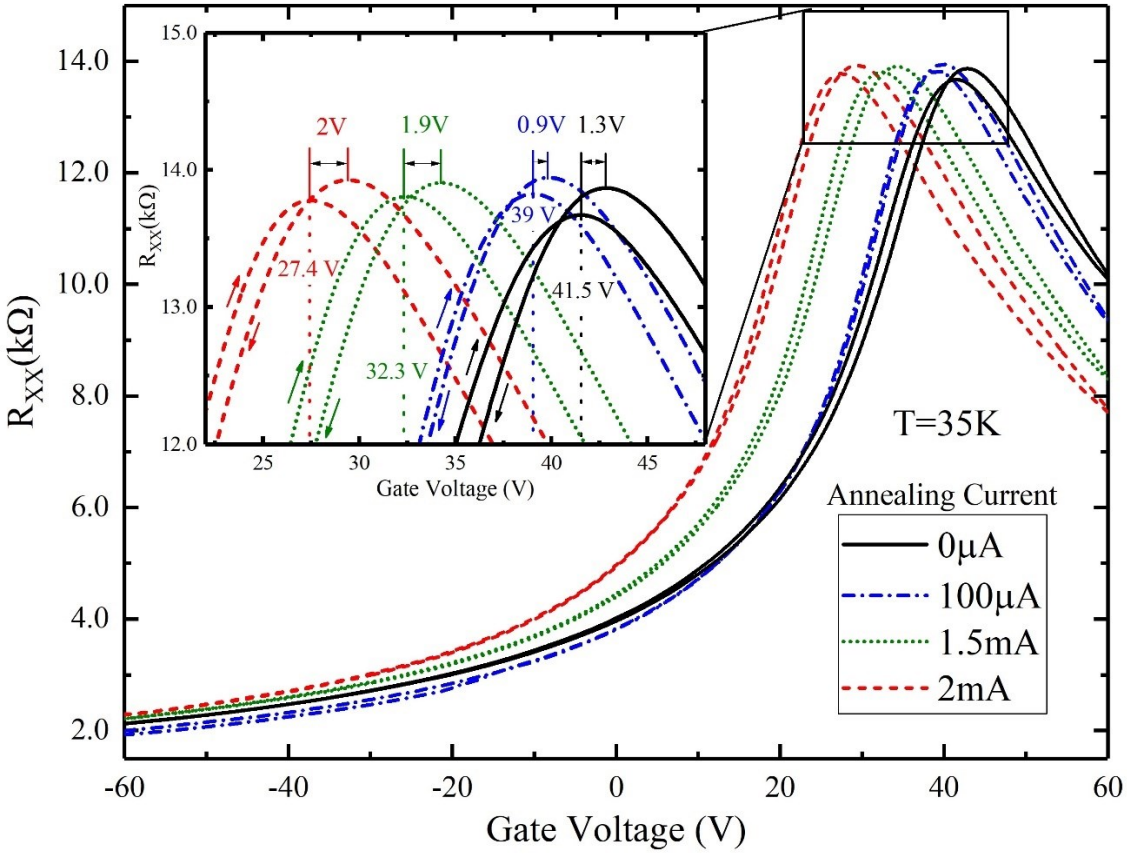


*Figure 5.4. Effect of the current annealing to the charge neutrality point. Diagonal resistance ($R_{xx}$) vs. the back-gate voltage is shown at 35 K without annealing the sample in solid (black) line, after annealing with 100 μA in dotted -dashed (blue)line, 1.5 mA in dotted line(green) and with 2 mA in dashed line (red). Reproduced with permission from Springer Nature [150].*

We annealed the sample further using a DC supply of 1.5 mA and 2 mA. The results are shown in Figure 5.4. The diagonal resistance ($R_{xx}$) is plotted against the back-gate voltage at 35 K. The data collected without annealing the sample is shown in solid (black) line, and after annealing with 100 μA is depicted in dotted-dashed (blue) line. The plots obtained after annealing with 1.5 mA and 2 mA are shown in dotted line (green) and dashed line (red) respectively. The inset shows an enlarged version of the plot near CNP of all the curves.

The CNP voltage observed while sweeping the back-gate voltage to the forward direction before annealing was 41.5 V. The voltage value shifted toward the zero with current annealing. We were able to get the CNP to 39 V with 100 μA anneal current and to 32.3 V and 27.4 V with 1.5 mA and 2 mA DC supply respectively. The difference between the CNP voltage for forward and backward sweep is decreased for 100 μA anneal current and then increased when the anneal current is increased. This observation indicates that the hysteresis increases even though the CNP shifted toward the zero voltage when annealed with a higher current for longer times.

Since the CNP changes in a broad range at room temperature and the change is significantly reduced at cryogenic temperatures, we studied the capability of controlling the charge neutrality voltage with a biased gate voltage supplied during sample cool down from room temperature. We observed that the CNP could be easily shifted toward the higher positive voltage side with a positive bias. With a negative back gate bias, we were able to get the CNP shifted toward lower positive voltage, but not to the negative voltage region where the device becomes n-type. Here we looked at the lower and upper limits of CNP shift we can achieve. We kept the sample for one hour with $-$ 60 V bias at room temperature and cooled to 35 K within 4 hours and then did the same thing with + 60 V bias. We performed this both before and after current annealing the sample. The results are shown in Figure 5.5.

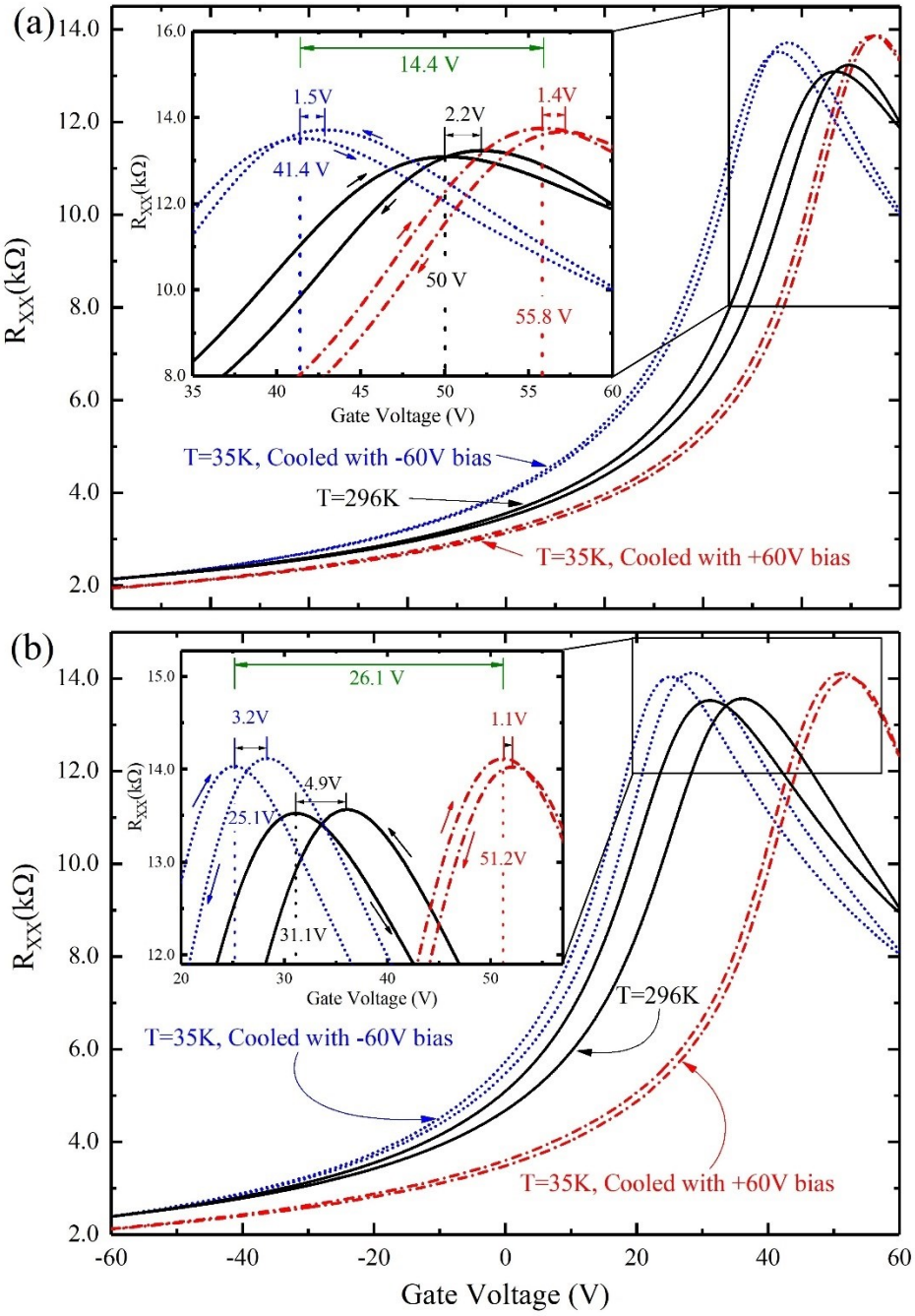


*Figure 5.5. Effect of current annealing on the tunable range of the charge neutrality point by cooling with a back-gate bias. (a) Demonstrates the situation before starting the current annealing, and the data collected afterward are plotted in (b). Both figures (a) and (b) shows the diagonal resistance ($R_{xx}$) plotted against the back-gate voltage after cooling with a -60 V gate bias in dotted line (blue) and with +60 V bias in dotted-dashed line (red) at 35 K. The solid (black) line corresponds to the data collected at room temperature. Insets provide a closer look at the region that we can observe the charge neutrality point. Reproduced with permission from Springer Nature [150].*

## 5.3 Conclusions

The hysteretic and electrical properties of back-gated graphene Hall bar devices prepared by standard CVD method were investigated by varying the back-gate voltage at room temperature as well as at cryogenic temperatures. A significant reduction of hysteresis was observed with cooling the device. The hysteresis effect can be explained as a result of the capacitive gating effect that can occur due to localized impurity potentials and the charge trapping and de-trapping mechanism near graphene top and bottom surfaces. The influence of gate sweeping toward impurity potentials got decreased significantly at a lower temperature (35 K).

We found that our samples were always p-type. The CNP shifted toward positive gate voltage with a positive gate bias suggesting that the charge trapping/de-trapping is dominant over the capacitive gating in our samples. The reason is, a capacitive gating will shift the CNP toward the negative gate voltage direction (or toward zero gate voltage from a higher positive value) while sweeping the gate voltage toward the positive direction, which is opposite to what we observed. The charge trapping mechanism agrees with our results. Observation of increased hysteresis after current annealing the sample for a long time may be due to the formation of charge traps in the substrate. Passing a higher current through the sample for a long time yield high temperature on the sample, which anneals the graphene and might create oxygen deficiency on $SiO_2$, which acts as charge trapping centers [152, 153]. Our observation of increasing the controllable range of CNP with respect to the applied back gate bias after current annealing also suggests a modification in the dielectric layer. Further studies are required to elucidate the underlying mechanism behind our observations.

## REFERENCES

[1] A. Shik, Quantum Wells, WORLD SCIENTIFIC1998.
[2] U.K. Wijewardena, T.R. Nanayakkara, A. Kriisa, C. Reichl, W. Wegscheider, R.G. Mani, Size dependence- and induced transformations- of fractional quantum Hall effects under tilted magnetic fields, Scientific Reports, 12 (2022) 19204.
[3] T. Ando, A.B. Fowler, F. Stern, Electronic properties of two-dimensional systems, Reviews of Modern Physics, 54 (1982) 437-672.
[4] W.T. Sommer, Liquid Helium as a Barrier to Electrons, Physical Review Letters, 12 (1964) 271-273.
[5] C.L. Kane, E.J. Mele, $Z_2$ Topological Order and the Quantum Spin Hall Effect, Physical Review Letters, 95 (2005) 146802.
[6] H.L. Störmer, R. Dingle, A.C. Gossard, W. Wiegmann, M.D. Sturge, Two-dimensional electron gas at a semiconductor-semiconductor interface, Solid State Communications, 29 (1979) 705-709.
[7] S. Schmult, C. Gerl, U. Wurstbauer, C. Mitzkus, W. Wegscheider, Carbon-doped high-mobility two-dimensional hole gases on (110) faced GaAs, Applied Physics Letters, 86 (2005).
[8] R. Dingle, H.L. Störmer, A.C. Gossard, W. Wiegmann, Electron mobilities in modulation-doped semiconductor heterojunction superlattices, Applied Physics Letters, 33 (2008) 665-667.
[9] R.G. Mani, Zero-resistance states induced by electromagnetic-wave excitation in GaAs/AlGaAs Heterostructures, Physica E: Low-dimensional Systems and Nanostructures, 22 (2004) 1-6.
[10] Y.J. Chung, K.A. Villegas Rosales, K.W. Baldwin, P.T. Madathil, K.W. West, M. Shayegan, L.N. Pfeiffer, Ultra-high-quality two-dimensional electron systems, Nature Materials, 20 (2021) 632-637.
[11] N.W. Ashcroft, N.D. Mermin, Solid state physics, Holt, Rinehart and Winston, New York, 1976.
[12] P. Drude, Zur Elektronentheorie der Metalle, Annalen der Physik, 306 (1900) 566-613.
[13] P. Drude, Zur Elektronentheorie der Metalle; II. Teil. Galvanomagnetische und thermomagnetische Effecte, Annalen der Physik, 308 (1900) 369-402.
[14] T. Ando, Y. Matsumoto, Y. Uemura, Theory of Hall Effect in a Two-Dimensional Electron System, Journal of the Physical Society of Japan, 39 (1975) 279-288.
[15] J. Wakabayashi, S. Kawaji, Hall Effect in Silicon MOS Inversion Layers under Strong Magnetic Fields, Journal of the Physical Society of Japan, 44 (1978) 1839-1849.
[16] K.v. Klitzing, G. Dorda, M. Pepper, New Method for High-Accuracy Determination of the Fine-Structure Constant Based on Quantized Hall Resistance, Physical Review Letters, 45 (1980) 494-497.
[17] K. von Klitzing, T. Chakraborty, P. Kim, V. Madhavan, X. Dai, J. McIver, Y. Tokura, L. Savary, D. Smirnova, A.M. Rey, C. Felser, J. Gooth, X. Qi, 40 years of the quantum Hall effect, Nature Reviews Physics, 2 (2020) 397-401.
[18] J. Weis, K. von Klitzing, Metrology and microscopic picture of the integer quantum Hall effect, Philosophical Transactions of the Royal Society A: Mathematical, Physical and Engineering Sciences, 369 (2011) 3954-3974.
[19] A. Abouzaid, J. Dai, S. Feiler, P. Kessler, C. Waddell, The Integer Quantum Hall Effect, 2018.

[20] R.G. Mani, K.v. Klitzing, Interference-voltage compensated Hall-effect device, German Patent Registration DE 4308375 A1, Germany, 1994.
[21] R.G. Mani, K.v. Klitzing, Hall-effect device with current and Hall-voltage connections, US Patent 5,646,527, USA, 1997.
[22] R.G. Mani, K.v. Klitzing, Offset reduction and separation of Hall and piezoresistive voltages through current injection, US Patent 6,008,643, USA, 1999.
[23] R.G. Mani, K. von Klitzing, Realization of dual, tunable, ordinary- and quantized-Hall resistances in doubly connected GaAs/AlGaAs heterostructures, Zeitschrift für Physik B Condensed Matter, 92 (1993) 335-339.
[24] M. RG, Transport Study of GaAs/AlGaAs Heterostructure-and n-Type GaAs-Devices in theAnti Hall Bar within a Hall Bar'Configuration, Journal of the Physical Society of Japan, 65 (1996) 1751-1759.
[25] R.G. Mani, Steady-state bulk current at high magnetic fields in Corbino-type GaAs/AlGaAs heterostructure devices, Europhysics Letters, 36 (1996) 203.
[26] R.G. Mani, K. von Klitzing, Temperature-insensitive offset reduction in a Hall effect device, Applied Physics Letters, 64 (1994) 3121-3123.
[27] R.G. Mani, K. von Klitzing, Hall effect under null current conditions, Applied Physics Letters, 64 (1994) 1262-1264.
[28] R.G. Mani, Experimental technique for realizing dual and multiple Hall effects in a single specimen, Europhysics Letters, 34 (1996) 139.
[29] R.G. Mani, Dual Hall effects in inhomogeneous doubly connected GaAs/AlGaAs heterostructure devices, Applied Physics Letters, 70 (1997) 2879-2881.
[30] R.G. Mani, Dual ordinary, integral quantum, and fractional quantum Hall effects in partially gated doubly connected GaAs/$Al_xGa_{1-x}As$ heterostructure devices, Physical Review B, 55 (1997) 15838-15841.
[31] D.C. Tsui, H.L. Stormer, A.C. Gossard, Two-Dimensional Magnetotransport in the Extreme Quantum Limit, Physical Review Letters, 48 (1982) 1559-1562.
[32] R.B. Laughlin, Anomalous Quantum Hall Effect: An Incompressible Quantum Fluid with Fractionally Charged Excitations, Physical Review Letters, 50 (1983) 1395-1398.
[33] J.K. Jain, Composite-fermion approach for the fractional quantum Hall effect, Physical Review Letters, 63 (1989) 199-202.
[34] R.G. Mani, K. von Klitzing, Fractional quantum Hall effects as an example of fractal geometry in nature, Zeitschrift für Physik B Condensed Matter, 100 (1996) 635-642.
[35] J.K. Jain, Composite Fermions, Cambridge University Press, Cambridge, 2007.
[36] S. Das Sarma, A. Pinczuk, Perspectives in Quantum Hall Effects: Novel Quantum Liquids in Low-Dimensional Semiconductor Structures, 1996.
[37] S. Girvin, R. Prange, The quantum Hall effect, DOI (1987).
[38] Y.J. Chung, D. Graf, L.W. Engel, K.A.V. Rosales, P.T. Madathil, K.W. Baldwin, K.W. West, L.N. Pfeiffer, M. Shayegan, Correlated States of 2D Electrons near the Landau Level Filling $\nu$ =1/7, Physical Review Letters, 128 (2022) 026802.
[39] K.A. Villegas Rosales, P.T. Madathil, Y.J. Chung, L.N. Pfeiffer, K.W. West, K.W. Baldwin, M. Shayegan, Fractional Quantum Hall Effect Energy Gaps: Role of Electron Layer Thickness, Physical Review Letters, 127 (2021) 056801.
[40] K.S. Novoselov, A.K. Geim, S.V. Morozov, D. Jiang, M.I. Katsnelson, I.V. Grigorieva, S.V. Dubonos, A.A. Firsov, Two-dimensional gas of massless Dirac fermions in graphene, Nature, 438 (2005) 197-200.

[41] K.I. Bolotin, F. Ghahari, M.D. Shulman, H.L. Stormer, P. Kim, Observation of the fractional quantum Hall effect in graphene, Nature, 462 (2009) 196-199.
[42] C.R. Dean, A.F. Young, P. Cadden-Zimansky, L. Wang, H. Ren, K. Watanabe, T. Taniguchi, P. Kim, J. Hone, K.L. Shepard, Multicomponent fractional quantum Hall effect in graphene, Nature Physics, 7 (2011) 693-696.
[43] B.I. Halperin, Theory of the quantized Hall conductance, helv. phys. acta, 56 (1983) 75.
[44] J.K. Jain, Thirty Years of Composite Fermions and Beyond, Fractional Quantum Hall Effects, pp. 1-78.
[45] J.P. Eisenstein, H.L. Stormer, L. Pfeiffer, K.W. West, Evidence for a phase transition in the fractional quantum Hall effect, Physical Review Letters, 62 (1989) 1540-1543.
[46] R.G. Clark, S.R. Haynes, A.M. Suckling, J.R. Mallett, P.A. Wright, J.J. Harris, C.T. Foxon, Spin configurations and quasiparticle fractional charge of fractional-quantum-Hall-effect ground states in the N=0 Landau level, Physical Review Letters, 62 (1989) 1536-1539.
[47] J.P. Eisenstein, H.L. Stormer, L.N. Pfeiffer, K.W. West, Evidence for a spin transition in the $\nu = 2/3$ fractional quantum Hall effect, Physical Review B, 41 (1990) 7910-7913.
[48] L.W. Engel, S.W. Hwang, T. Sajoto, D.C. Tsui, M. Shayegan, Fractional quantum Hall effect at $\nu = 2/3$ and 3/5 in tilted magnetic fields, Physical Review B, 45 (1992) 3418-3425.
[49] U.K. Wijewardena, T. Nanayakkara, A. Kriisa, C. Reichl, W. Wegscheider, R. Mani, Tilt-induced transformations of fractional quantum Hall effects, APS March Meeting Abstracts, 2023, pp. W29.00005.
[50] B.E. Feldman, A.J. Levin, B. Krauss, D.A. Abanin, B.I. Halperin, J.H. Smet, A. Yacoby, Fractional Quantum Hall Phase Transitions and Four-Flux States in Graphene, Physical Review Letters, 111 (2013) 076802.
[51] W. Kang, J.B. Young, S.T. Hannahs, E. Palm, K.L. Campman, A.C. Gossard, Evidence for a spin transition in the $\nu = 2/5$ fractional quantum Hall effect, Physical Review B, 56 (1997) R12776-R12779.
[52] A.S. Yeh, H.L. Stormer, D.C. Tsui, L.N. Pfeiffer, K.W. Baldwin, K.W. West, Effective Mass and g Factor of Four-Flux-Quanta Composite Fermions, Physical Review Letters, 82 (1999) 592-595.
[53] A. Kou, D.T. McClure, C.M. Marcus, L.N. Pfeiffer, K.W. West, Dynamic Nuclear Polarization in the Fractional Quantum Hall Regime, Physical Review Letters, 105 (2010) 056804.
[54] L.A. Tracy, J.P. Eisenstein, L.N. Pfeiffer, K.W. West, Spin Transition in the Half-Filled Landau Level, Physical Review Letters, 98 (2007) 086801.
[55] Y. Liu, S. Hasdemir, A. Wójs, J.K. Jain, L.N. Pfeiffer, K.W. West, K.W. Baldwin, M. Shayegan, Spin polarization of composite fermions and particle-hole symmetry breaking, Physical Review B, 90 (2014) 085301.
[56] R.G. Mani, Transport Study of GaAs/AlGaAs Heterostructure- and n-Type GaAs-Devices in the `Anti Hall Bar within a Hall Bar' Configuration, Journal of the Physical Society of Japan, 65 (1996) 1751-1759.
[57] R.G. Mani, A. Kriisa, W. Wegscheider, Size-dependent giant-magnetoresistance in millimeter scale GaAs/AlGaAs 2D electron devices, Scientific Reports, 3 (2013) 2747.
[58] R.G. Mani, J.R. Anderson, Study of the single-particle and transport lifetimes in GaAs/AlGaAs, Physical Review B, 37 (1988) 4299-4302.
[59] B.I. Halperin, P.A. Lee, N. Read, Theory of the half-filled Landau level, Physical Review B, 47 (1993) 7312-7343.

[60] R.R. Du, H.L. Stormer, D.C. Tsui, L.N. Pfeiffer, K.W. West, Shubnikov-deHaas oscillations around $\nu = 1/2$ Landau level filling factor, Solid State Communications, 90 (1994) 71-75.
[61] R.G. Mani, U.K. Wijewardena, T.R. Nanayakkara, A. Kriisa, C. Reichl, W. Wegscheider, Marginal metallic state at a fractional filling of '8/5' and '4/3' of Landau levels in the GaAs/AlGaAs 2D electron system, Scientific Reports, 11 (2021) 15003.
[62] R.G. Mani, J.H. Smet, K. von Klitzing, V. Narayanamurti, W.B. Johnson, V. Umansky, Zero-resistance states induced by electromagnetic-wave excitation in GaAs/AlGaAs heterostructures, Nature, 420 (2002) 646-650.
[63] M.A. Zudov, R.R. Du, L.N. Pfeiffer, K.W. West, Evidence for a New Dissipationless Effect in 2D Electronic Transport, Physical Review Letters, 90 (2003) 046807.
[64] R.G. Mani, Evolution of Shubnikov–de Haas oscillations under photoexcitation in the regime of the radiation-induced zero-resistance states, Physica E: Low-dimensional Systems and Nanostructures, 40 (2008) 1178-1181.
[65] T. Ye, H.-C. Liu, W. Wegscheider, R.G. Mani, Combined study of microwave-power/linear-polarization dependence of the microwave-radiation-induced magnetoresistance oscillations in GaAs/AlGaAs devices, Physical Review B, 89 (2014) 155307.
[66] Z. Wang, R.L. Samaraweera, C. Reichl, W. Wegscheider, R.G. Mani, Tunable electron heating induced giant magnetoresistance in the high mobility GaAs/AlGaAs 2D electron system, Scientific Reports, 6 (2016) 38516.
[67] R.G. Mani, C. Gerl, S. Schmult, W. Wegscheider, V. Umansky, Nonlinear growth in the amplitude of radiation-induced magnetoresistance oscillations, Physical Review B, 81 (2010) 125320.
[68] J. Iñarrea, R.G. Mani, W. Wegscheider, Sublinear radiation power dependence of photoexcited resistance oscillations in two-dimensional electron systems, Physical Review B, 82 (2010) 205321.
[69] R.R. Du, A.S. Yeh, H.L. Stormer, D.C. Tsui, L.N. Pfeiffer, K.W. West, Fractional Quantum Hall Effect around $\nu = 3/2$: Composite Fermions with a Spin, Physical Review Letters, 75 (1995) 3926-3929.
[70] B. Kramer, S. Kettemann, T. Ohtsuki, Localization in the quantum Hall regime, Physica E: Low-dimensional Systems and Nanostructures, 20 (2003) 172-187.
[71] L.W. Engel, D. Shahar, Ç. Kurdak, D.C. Tsui, Microwave frequency dependence of integer quantum Hall effect: Evidence for finite-frequency scaling, Physical Review Letters, 71 (1993) 2638-2641.
[72] E.P. De Poortere, E. Tutuc, S.J. Papadakis, M. Shayegan, Resistance Spikes at Transitions Between Quantum Hall Ferromagnets, Science, 290 (2000) 1546-1549.
[73] D. Maryenko, J. Falson, Y. Kozuka, A. Tsukazaki, M. Kawasaki, Polarization-dependent Landau level crossing in a two-dimensional electron system in a MgZnO/ZnO heterostructure, Physical Review B, 90 (2014) 245303.
[74] D.R. Leadley, R.J. Nicholas, J.J. Harris, C.T. Foxon, Critical collapse of the exchange-enhanced spin splitting in two-dimensional systems, Physical Review B, 58 (1998) 13036-13046.
[75] A. Raymond, J.L. Robert, C. Bousquet, W. Zawadzki, F. Alexandre, I.M. Masson, Gigantic exchange enhancement of spin g-factor for two-dimensional electron gas in GaAs, Solid State Communications, 55 (1985) 271-274.
[76] P.T. Coleridge, Z.W. Wasilewski, P. Zawadzki, A.S. Sachrajda, H.A. Carmona, Composite-fermion effective masses, Physical Review B, 52 (1995) R11603-R11606.
[77] A.K. Geim, K.S. Novoselov, The rise of graphene, Nat Mater, 6 (2007) 183-191.

[78] A.H. Castro Neto, F. Guinea, N.M.R. Peres, K.S. Novoselov, A.K. Geim, The electronic properties of graphene, Reviews of Modern Physics, 81 (2009) 109-162.
[79] Y. Zhang, T.T. Tang, C. Girit, Z. Hao, M.C. Martin, A. Zettl, M.F. Crommie, Y.R. Shen, F. Wang, Direct observation of a widely tunable bandgap in bilayer graphene, Nature, 459 (2009) 820-823.
[80] R.G. Mani, A. Kriisa, R. Munasinghe, Radiation-induced magnetoresistance oscillations in monolayer and bilayer graphene, Scientific Reports, 9 (2019) 7278.
[81] R.G. Mani, J. Hankinson, C. Berger, W.A. de Heer, Observation of resistively detected hole spin resonance and zero-field pseudo-spin splitting in epitaxial graphene, Nature Communications, 3 (2012) 996.
[82] K.S. Novoselov, V.I. Fal′ko, L. Colombo, P.R. Gellert, M.G. Schwab, K. Kim, A roadmap for graphene, Nature, 490 (2012) 192-200.
[83] P. Zare, M. Aleemardani, A. Seifalian, Z. Bagher, A.M. Seifalian, Graphene Oxide: Opportunities and Challenges in Biomedicine, Nanomaterials, 11 (2021) 1083.
[84] A.A. Balandin, S. Ghosh, W. Bao, I. Calizo, D. Teweldebrhan, F. Miao, C.N. Lau, Superior Thermal Conductivity of Single-Layer Graphene, Nano Letters, 8 (2008) 902-907.
[85] D.-M. Sun, C. Liu, W.-C. Ren, H.-M. Cheng, A Review of Carbon Nanotube- and Graphene-Based Flexible Thin-Film Transistors, Small, 9 (2013) 1188-1205.
[86] T. Das, B.K. Sharma, A.K. Katiyar, J.-H. Ahn, Graphene-based flexible and wearable electronics *, Journal of Semiconductors, 39 (2018) 011007.
[87] N. Mahmood, C. Zhang, H. Yin, Y. Hou, Graphene-based nanocomposites for energy storage and conversion in lithium batteries, supercapacitors and fuel cells, Journal of Materials Chemistry A, 2 (2014) 15-32.
[88] A. Kausar, I. Rafique, B. Muhammad, Aerospace Application of Polymer Nanocomposite with Carbon Nanotube, Graphite, Graphene Oxide, and Nanoclay, Polymer-Plastics Technology and Engineering, 56 (2017) 1438-1456.
[89] J. Sun, N. Lindvall, M.T. Cole, K.T.T. Angel, T. Wang, K.B.K. Teo, D.H.C. Chua, J. Liu, A. Yurgens, Low Partial Pressure Chemical Vapor Deposition of Graphene on Copper, IEEE Transactions on Nanotechnology, 11 (2012) 255-260.
[90] J.K. Wassei, M. Mecklenburg, J.A. Torres, J.D. Fowler, B.C. Regan, R.B. Kaner, B.H. Weiller, Chemical Vapor Deposition of Graphene on Copper from Methane, Ethane and Propane: Evidence for Bilayer Selectivity, Small, 8 (2012) 1415-1422.
[91] K.S. Novoselov, A.K. Geim, S.V. Morozov, D. Jiang, Y. Zhang, S.V. Dubonos, I.V. Grigorieva, A.A. Firsov, Electric field effect in atomically thin carbon films, Science, 306 (2004) 666-669.
[92] A.K. Geim, I.V. Grigorieva, Van der Waals heterostructures, Nature, 499 (2013) 419-425.
[93] M. Yi, Z. Shen, A review on mechanical exfoliation for the scalable production of graphene, Journal of Materials Chemistry A, 3 (2015) 11700-11715.
[94] N. Jain, C.A. Durcan, R. Jacobs-Gedrim, Y. Xu, B. Yu, Graphene interconnects fully encapsulated in layered insulator hexagonal boron nitride, Nanotechnology, 24 (2013) 355202.
[95] I. Jo, M.T. Pettes, J. Kim, K. Watanabe, T. Taniguchi, Z. Yao, L. Shi, Thermal Conductivity and Phonon Transport in Suspended Few-Layer Hexagonal Boron Nitride, Nano Letters, 13 (2013) 550-554.
[96] U.K. Wijewardena, T. Nanayakkara, S. Withanage, A. Kriisa, R. Mani, Fabrication and Characterization of h-BN capped Exfoliated Multi-layer Graphene, APS March Meeting Abstracts, 2020, pp. G53.00004.

[97] N. Petrone, T. Chari, I. Meric, L. Wang, K.L. Shepard, J. Hone, Flexible Graphene Field-Effect Transistors Encapsulated in Hexagonal Boron Nitride, ACS Nano, 9 (2015) 8953-8959.
[98] X. Zhou, X. Hu, J. Yu, S. Liu, Z. Shu, Q. Zhang, H. Li, Y. Ma, H. Xu, T. Zhai, 2D Layered Material-Based van der Waals Heterostructures for Optoelectronics, Advanced Functional Materials, 28 (2018) 1706587.
[99] A. Ambrosi, M. Pumera, The CVD graphene transfer procedure introduces metallic impurities which alter the graphene electrochemical properties, Nanoscale, 6 (2014) 472-476.
[100] C. Miao, C. Zheng, O. Liang, Y.-H. Xie, Chemical vapor deposition of graphene, Physics and applications of graphene-experiments, DOI (2011) 2011.
[101] S. Bhaviripudi, X. Jia, M.S. Dresselhaus, J. Kong, Role of Kinetic Factors in Chemical Vapor Deposition Synthesis of Uniform Large Area Graphene Using Copper Catalyst, Nano Letters, 10 (2010) 4128-4133.
[102] S. Withanage, T. Nanayakkara, U.K. Wijewardena, A. Kriisa, R.G. Mani, The role of surface morphology on nucleation density limitation during the CVD growth of graphene and the factors influencing graphene wrinkle formation, MRS Advances, 4 (2019) 3337-3345.
[103] T.R. Nanayakkara, U.K. Wijewardena, S.M. Withanage, A. Kriisa, R.L. Samaraweera, R.G. Mani, Strain relaxation in different shapes of single crystal graphene grown by chemical vapor deposition on copper, Carbon, 168 (2020) 684-690.
[104] J. Vaari, J. Lahtinen, P. Hautojärvi, The adsorption and decomposition of acetylene on clean and K-covered Co(0001), Catalysis Letters, 44 (1997) 43-49.
[105] Q. Yu, J. Lian, S. Siriponglert, H. Li, Y.P. Chen, S.-S. Pei, Graphene segregated on Ni surfaces and transferred to insulators, Applied Physics Letters, 93 (2008).
[106] X. Li, W. Cai, J. An, S. Kim, J. Nah, D. Yang, R. Piner, A. Velamakanni, I. Jung, E. Tutuc, S.K. Banerjee, L. Colombo, R.S. Ruoff, Large-Area Synthesis of High-Quality and Uniform Graphene Films on Copper Foils, Science, 324 (2009) 1312-1314.
[107] O. Sarajlic, R.G.G. Mani, Mesoscale Scanning Electron and Tunneling Microscopy Study of the Surface Morphology of Thermally Annealed Copper Foils for Graphene Growth, Chemistry of Materials, 25 (2013) 1643-1648.
[108] S. Chen, L. Brown, M. Levendorf, W. Cai, S.-Y. Ju, J. Edgeworth, X. Li, C.W. Magnuson, A. Velamakanni, R.D. Piner, J. Kang, J. Park, R.S. Ruoff, Oxidation Resistance of Graphene-Coated Cu and Cu/Ni Alloy, ACS Nano, 5 (2011) 1321-1327.
[109] J. Cho, L. Gao, J. Tian, H. Cao, W. Wu, Q. Yu, E.N. Yitamben, B. Fisher, J.R. Guest, Y.P. Chen, N.P. Guisinger, Atomic-Scale Investigation of Graphene Grown on Cu Foil and the Effects of Thermal Annealing, ACS Nano, 5 (2011) 3607-3613.
[110] H. Chen, W. Zhu, Z. Zhang, Contrasting Behavior of Carbon Nucleation in the Initial Stages of Graphene Epitaxial Growth on Stepped Metal Surfaces, Physical Review Letters, 104 (2010) 186101.
[111] R.M. Jacobberger, M.S. Arnold, Graphene Growth Dynamics on Epitaxial Copper Thin Films, Chemistry of Materials, 25 (2013) 871-877.
[112] G.A. López, E.J. Mittemeijer, The solubility of C in solid Cu, Scripta Materialia, 51 (2004) 1-5.
[113] X. Li, W. Cai, L. Colombo, R.S. Ruoff, Evolution of Graphene Growth on Ni and Cu by Carbon Isotope Labeling, Nano Letters, 9 (2009) 4268-4272.
[114] A.W. Robertson, J.H. Warner, Hexagonal single crystal domains of few-layer graphene on copper foils, Nano Lett, 11 (2011) 1182-1189.

[115] J. Li, J. Zhuang, C. Shen, Y. Tian, Y. Que, R. Ma, J. Pan, Y. Zhang, Y. Wang, S. Du, F. Ding, H.-J. Gao, Impurity-induced formation of bilayered graphene on copper by chemical vapor deposition, Nano Research, 9 (2016) 2803-2810.
[116] K. Yan, H. Peng, Y. Zhou, H. Li, Z. Liu, Formation of bilayer bernal graphene: layer-by-layer epitaxy via chemical vapor deposition, Nano Lett, 11 (2011) 1106-1110.
[117] L. Gao, J.R. Guest, N.P. Guisinger, Epitaxial Graphene on Cu(111), Nano Letters, 10 (2010) 3512-3516.
[118] S. Withanage, T. Nanayakkara, B. Gunawardana, C.R. Munasinghe, U.K. Wijewardena, R. Samaraweera, A. Kriisa, R. Mani, The effect of multi-step Cu surface oxidization on growth of single crystal graphene by low pressure chemical vapor deposition, APS March Meeting Abstracts, 2019, pp. E13. 002.
[119] T. Nanayakkara, S. Withanage, U.K. Wijewardena, A. Kriisa, R. Samaraweera, R. Mani, Study of the Shape Single Crystal Graphene Growth by Chemical Vapor Deposition on Copper Foil, APS March Meeting Abstracts, 2020, pp. W57.00008.
[120] L. Gan, Z. Luo, Turning off hydrogen to realize seeded growth of subcentimeter single-crystal graphene grains on copper, ACS Nano, 7 (2013) 9480-9488.
[121] Z. Luo, Y. Lu, D.W. Singer, M.E. Berck, L.A. Somers, B.R. Goldsmith, A.T.C. Johnson, Effect of Substrate Roughness and Feedstock Concentration on Growth of Wafer-Scale Graphene at Atmospheric Pressure, Chemistry of Materials, 23 (2011) 1441-1447.
[122] B. Zhang, W.H. Lee, R. Piner, I. Kholmanov, Y. Wu, H. Li, H. Ji, R.S. Ruoff, Low-temperature chemical vapor deposition growth of graphene from toluene on electropolished copper foils, ACS Nano, 6 (2012) 2471-2476.
[123] X. Xu, Z. Zhang, L. Qiu, J. Zhuang, L. Zhang, H. Wang, C. Liao, H. Song, R. Qiao, P. Gao, Z. Hu, L. Liao, Z. Liao, D. Yu, E. Wang, F. Ding, H. Peng, K. Liu, Ultrafast growth of single-crystal graphene assisted by a continuous oxygen supply, Nature Nanotechnology, 11 (2016) 930-935.
[124] N. Woehrl, O. Ochedowski, S. Gottlieb, K. Shibasaki, S. Schulz, Plasma-enhanced chemical vapor deposition of graphene on copper substrates, AIP Advances, 4 (2014).
[125] N.C. Yeh, C.C. Hsu, J. Bagley, W.S. Tseng, Single-step growth of graphene and graphene-based nanostructures by plasma-enhanced chemical vapor deposition, Nanotechnology, 30 (2019) 162001.
[126] M. Li, D. Liu, D. Wei, X. Song, D. Wei, A.T.S. Wee, Controllable Synthesis of Graphene by Plasma-Enhanced Chemical Vapor Deposition and Its Related Applications, Advanced Science, 3 (2016) 1600003.
[127] G. Yuan, D. Lin, Y. Wang, X. Huang, W. Chen, X. Xie, J. Zong, Q.Q. Yuan, H. Zheng, D. Wang, J. Xu, S.C. Li, Y. Zhang, J. Sun, X. Xi, L. Gao, Proton-assisted growth of ultra-flat graphene films, Nature, 577 (2020) 204-208.
[128] J.-H. Chen, C. Jang, S. Xiao, M. Ishigami, M.S. Fuhrer, Intrinsic and extrinsic performance limits of graphene devices on SiO2, Nature Nanotechnology, 3 (2008) 206-209.
[129] X. Du, I. Skachko, A. Barker, E.Y. Andrei, Approaching ballistic transport in suspended graphene, Nature Nanotechnology, 3 (2008) 491-495.
[130] Y.-M. Lin, C. Dimitrakopoulos, K.A. Jenkins, D.B. Farmer, H.-Y. Chiu, A. Grill, P. Avouris, 100-GHz Transistors from Wafer-Scale Epitaxial Graphene, Science, 327 (2010) 662-662.
[131] U.K. Wijewardena, S.E. Brown, X.-Q. Wang, Epoxy-Carbonyl Conformation of Graphene Oxides, The Journal of Physical Chemistry C, 120 (2016) 22739-22743.

[132] X. Du, I. Skachko, F. Duerr, A. Luican, E.Y. Andrei, Fractional quantum Hall effect and insulating phase of Dirac electrons in graphene, Nature, 462 (2009) 192-195.
[133] R.R. Nair, P. Blake, A.N. Grigorenko, K.S. Novoselov, T.J. Booth, T. Stauber, N.M.R. Peres, A.K. Geim, Fine Structure Constant Defines Visual Transparency of Graphene, Science, 320 (2008) 1308-1308.
[134] K.S. Novoselov, A.K. Geim, S.V. Morozov, D. Jiang, Y. Zhang, S.V. Dubonos, I.V. Grigorieva, A.A. Firsov, Electric Field Effect in Atomically Thin Carbon Films, Science, 306 (2004) 666-669.
[135] X. Li, W. Cai, J. An, S. Kim, J. Nah, D. Yang, R. Piner, A. Velamakanni, I. Jung, E. Tutuc, S.K. Banerjee, L. Colombo, R.S. Ruoff, Large-area synthesis of high-quality and uniform graphene films on copper foils, Science, 324 (2009) 1312-1314.
[136] O.I. Sarajlic, R.G. Mani, Mesoscale Scanning Electron and Tunneling Microscopy Study of the Surface Morphology of Thermally Annealed Copper Foils for Graphene Growth, Chemistry of Materials, 25 (2013) 1643-1648.
[137] X. Li, C.W. Magnuson, A. Venugopal, R.M. Tromp, J.B. Hannon, E.M. Vogel, L. Colombo, R.S. Ruoff, Large-Area Graphene Single Crystals Grown by Low-Pressure Chemical Vapor Deposition of Methane on Copper, Journal of the American Chemical Society, 133 (2011) 2816-2819.
[138] Nguyen H. Shon, T. Ando, Quantum Transport in Two-Dimensional Graphite System, Journal of the Physical Society of Japan, 67 (1998) 2421-2429.
[139] R.G. Mani, Method for determining the residual electron- and hole-densities about the neutrality point over the gate-controlled n ↔ p transition in graphene, Applied Physics Letters, 108 (2016) 033507.
[140] J. Martin, N. Akerman, G. Ulbricht, T. Lohmann, J.H. Smet, K. von Klitzing, A. Yacoby, Observation of electron–hole puddles in graphene using a scanning single-electron transistor, Nature Physics, 4 (2008) 144-148.
[141] M.I. Katsnelson, A.K. Geim, Electron Scattering on Microscopic Corrugations in Graphene, Philosophical Transactions: Mathematical, Physical and Engineering Sciences, 366 (2008) 195-204.
[142] H. Wang, Y. Wu, C. Cong, J. Shang, T. Yu, Hysteresis of Electronic Transport in Graphene Transistors, ACS Nano, 4 (2010) 7221-7228.
[143] A. Kozbial, Z. Li, J. Sun, X. Gong, F. Zhou, Y. Wang, H. Xu, H. Liu, L. Li, Understanding the intrinsic water wettability of graphite, Carbon, 74 (2014) 218-225.
[144] T.O. Wehling, A.I. Lichtenstein, M.I. Katsnelson, First-principles studies of water adsorption on graphene: The role of the substrate, Applied Physics Letters, 93 (2008) 202110.
[145] X. Li, Y. Zhu, W. Cai, M. Borysiak, B. Han, D. Chen, R.D. Piner, L. Colombo, R.S. Ruoff, Transfer of Large-Area Graphene Films for High-Performance Transparent Conductive Electrodes, Nano Letters, 9 (2009) 4359-4363.
[146] K. Yan, H. Peng, Y. Zhou, H. Li, Z. Liu, Formation of Bilayer Bernal Graphene: Layer-by-Layer Epitaxy via Chemical Vapor Deposition, Nano Letters, 11 (2011) 1106-1110.
[147] T. Feng, D. Xie, G. Li, J. Xu, H. Zhao, T. Ren, H. Zhu, Temperature and gate voltage dependent electrical properties of graphene field-effect transistors, Carbon, 78 (2014) 250-256.
[148] J.E. Furneaux, T.L. Reinecke, Effects of interface charge on the quantum Hall effect, Physical Review B, 33 (1986) 6897-6908.

[149] U.K. Wijewardena, R. Samaraweera, A. Kriisa, B. Gunawardana, T. Nanayakkara, C.R. Munasinghe, R. Mani, Transport Properties of CVD Graphene Cooled with a Biased Gate Voltage, APS March Meeting Abstracts, 2018, pp. V40. 006.
[150] U.K. Wijewardena, T. Nanayakkara, R. Samaraweera, S. Withanage, A. Kriisa, R.G. Mani, Effects of Long-Time Current Annealing to the Hysteresis in CVD Graphene on SiO2, MRS Advances, 4 (2019) 3319-3326.
[151] J.S. Lee, S. Ryu, K. Yoo, I.S. Choi, W.S. Yun, J. Kim, Origin of Gate Hysteresis in Carbon Nanotube Field-Effect Transistors, The Journal of Physical Chemistry C, 111 (2007) 12504-12507.
[152] P. Kumar, A. Kumar, Carrier type modulation in current annealed graphene layers, Applied Physics Letters, 104 (2014) 083517.
[153] U.K. Wijewardena, T. Nanayakkara, R. Samaraweera, B. Gunawardana, C.R. Munasinghe, S. Withanage, A. Kriisa, R. Mani, Effect of current annealing to the transport properties of CVD graphene cooled with a biased gate voltage, APS March Meeting Abstracts, 2019, pp. A13. 004.

# APPENDICES

## Appendix A: Instrumentation for the Study of FQHE in GaAs/AlGaAs

In order to study the Fractional Quantum Hall Effect (FQHE), it is essential to achieve extremely low temperatures. To accomplish this, we utilized the Oxford Triton dry dilution refrigerator, capable of cooling the system down to temperatures as low as 10 mK. Additionally, we implemented techniques such as lock-in methods and ground isolation to ensure low noise measurements. Moreover, we incorporated a sample holder that allows for rotation, enabling the tilting of the sample with respect to the magnetic field.

### *Appendix A.1 Oxford Triton dilution refrigerator*

The measurements were performed using the Oxford Triton closed cycle dilution refrigerator shown in Figure A.1. This system includes a powerful superconducting magnet that can produce a maximum field of 12 T at a temperature of 4.2 K. The cryostat, which encloses the cold part of the system, maintains a vacuum environment known as the outer vacuum chamber (OVC) to protect the cold components. Additionally, radiation shields are used to prevent unwanted heating of the inner cold parts.

The cooling process involves two main loops: the pre-cool loop and the Dilution Unit. The pre-cool loop circulates a gas mixture to cool down the system to 10 K or lower. Then, the gas in the pre-cool loop is removed using a turbopump. The gas mixture is then circulated in the dilution system to reach a temperature below 1 K. At this stage, the helium gas mixture needs to be condensed into a liquid form, which requires high pressure and low temperature.

To achieve this, several steps are taken. First, the mixture is compressed using a $^3$He compressor. Then, it passes through a series of heat exchangers inside the cryostat to cool the mixture to 4 K. In a traditional dilution system, a separate pump is used to condense the helium

gas into liquid at the $^4$He stage (also known as the 1 K pot), but this system does not have that option. Instead, the mixture is condensed using a Joule-Thompson stage, which consists of a highly efficient heat exchanger located in the still pumping line, and an impedance where the gas undergoes an isenthalpic expansion process.

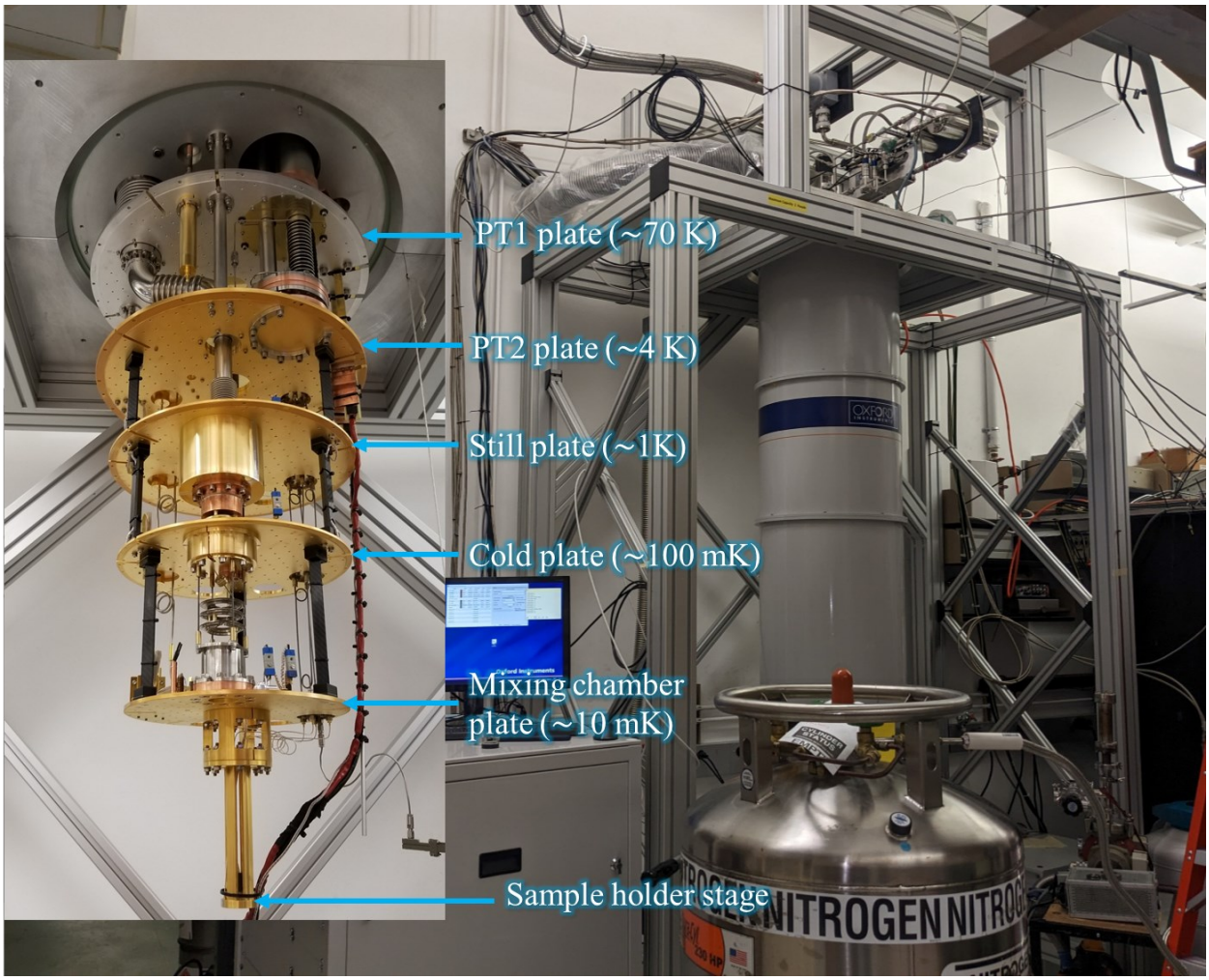


*Figure A.1 Picture of the Oxford Triton dilution refrigerator. Inside and other components inside the vacuum chamber are shown in the inset figure on the left.*

***Appendix A.2 Sample rotation setup***


*Figure A.2 Sample rotation system. (a) The setup features a stepper motor and a sample rotator assembly connected to the top plate of the dilution refrigerator. (b) The controller box, equipped with an Arduino board programmed for stepper motor control. (c) A GaAs/AlGaAs sample in a chip carrier connected to the rotatable sample holder. A rotation sensor is visible on the right, while coaxial loops for microwave application are visible on both sides of the sample. (d) The sample puck attached to the refrigerator, with the radiation shield of the puck removed for clarity.*

### *Appendix A.3 Measurement instrumentation*

We have employed low-frequency lock-in techniques in our experimental setup to accurately measure electrical signals from the samples. In the initial phase of our experiments, we utilized a custom-built ground isolation box that incorporates two optoisolators to isolate the ground of the signal source from the measuring device (see Figure A.3). To power the box, we employed two 9V batteries. This innovative technique effectively minimizes the adverse effects of ground loops on our measurements. Moreover, the isolation box is equipped with a variable resistor assembly, allowing us to maintain a constant current. We carefully selected the resistance in the box to be significantly larger than the resistance of the sample, ensuring that any variations in current caused by the sample's resistance are negligible. Specifically, for our measurements, we employed a 10 MΩ resistor, which provided a 100 nA current when driven by a 1 V input signal from the lock-in's internal oscillator. Subsequently, we upgraded our setup by incorporating the SRS CS580 current source to provide isolated current to the sample, replacing the need for the ground isolation box.

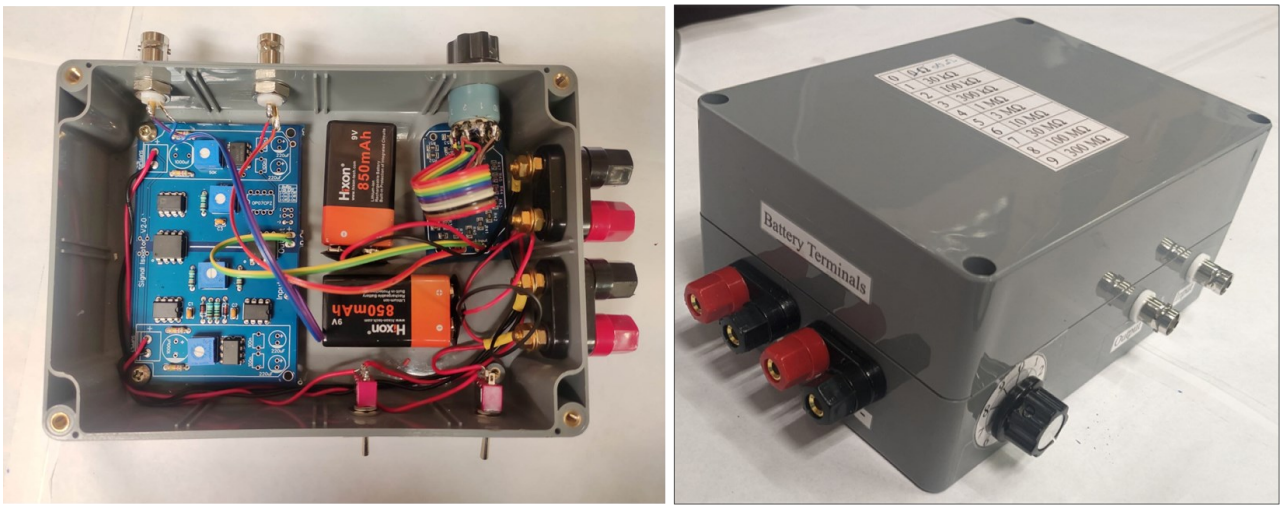


*Figure A.3 Ground Isolation Box. The left figure depicts the internal components of the box, which consist of two rechargeable 9V batteries, a variable resistor assembly, and optoisolator circuitry. The right figure showcases the external appearance of the box, featuring battery charging terminals, input and output BNC connectors, and a resistance selector knob.*

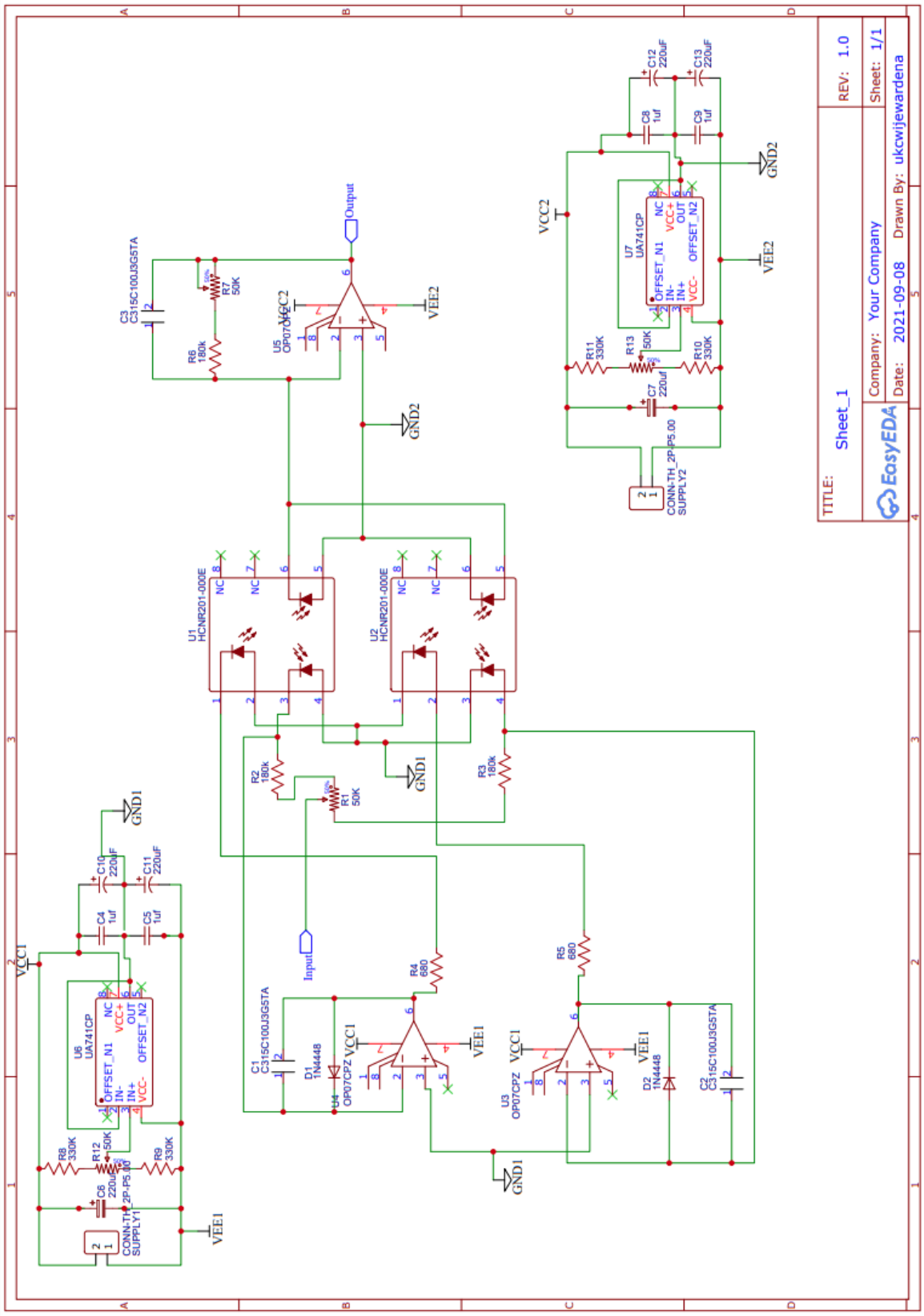


*Figure A.4 Circuit diagram for the ground isolation with two optoisolators.*

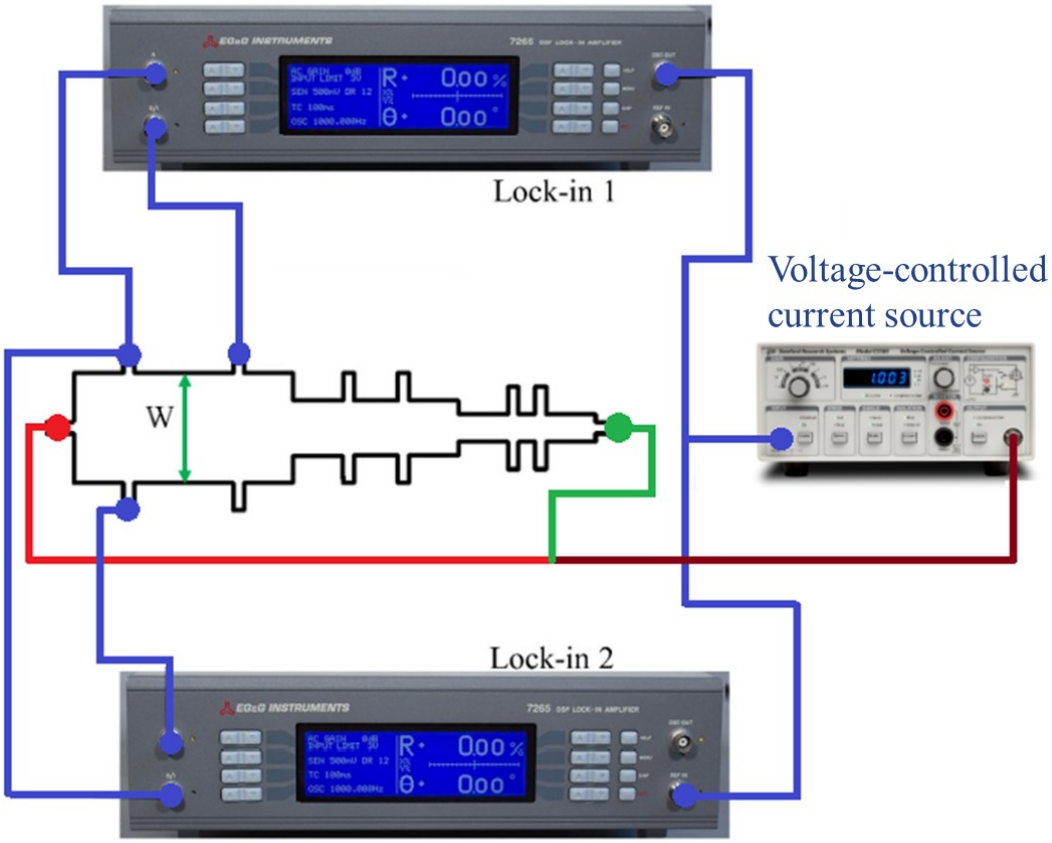


*Figure A.5 Schematic diagram of electrical connections for a typical measurement. Lock-in Amplifier 1 measures the longitudinal voltage while supplying AC voltage with a specific frequency to the input of either the ground isolation box or the SRS CS580 source. The same signal serves as the input reference for Lock-in Amplifier 2, which measures the Hall voltage of the sample. Please note that the display of the lock-in amplifiers does not accurately represent the actual measurement conditions.*

## Appendix B: Fabrication and measurements of graphene devices

### *Appendix B.1 Exfoliated graphene devices*

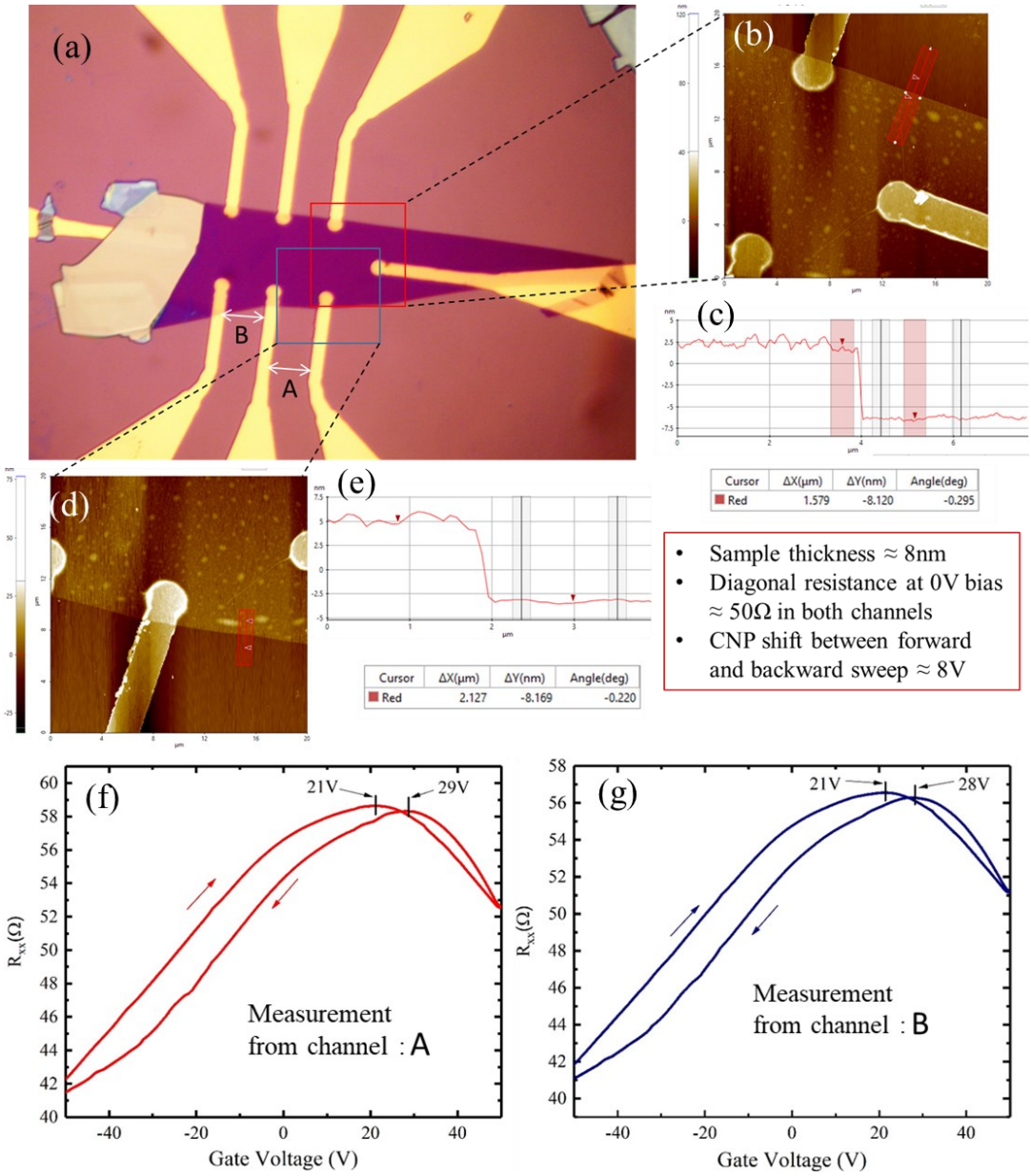


*Figure A.6 Optical Microscope (OM) image, Atomic Force Microscopy (AFM) images, and transport measurements of multi-layer graphene device GrE_SM3. (a) OM image of the graphene device indicating the regions selected for AFM analysis. (b, c) AFM images and corresponding height profiles of the areas marked in (a). (d, e) AFM images and corresponding height profiles of other areas indicated in (a). (f) Transport measurements from Channel A, as shown in (a). (g) Transport measurements from Channel B, as depicted in (a). Note: The AFM images provide nanoscale topographic information, while the transport measurements show the electrical characteristics of the graphene device.*

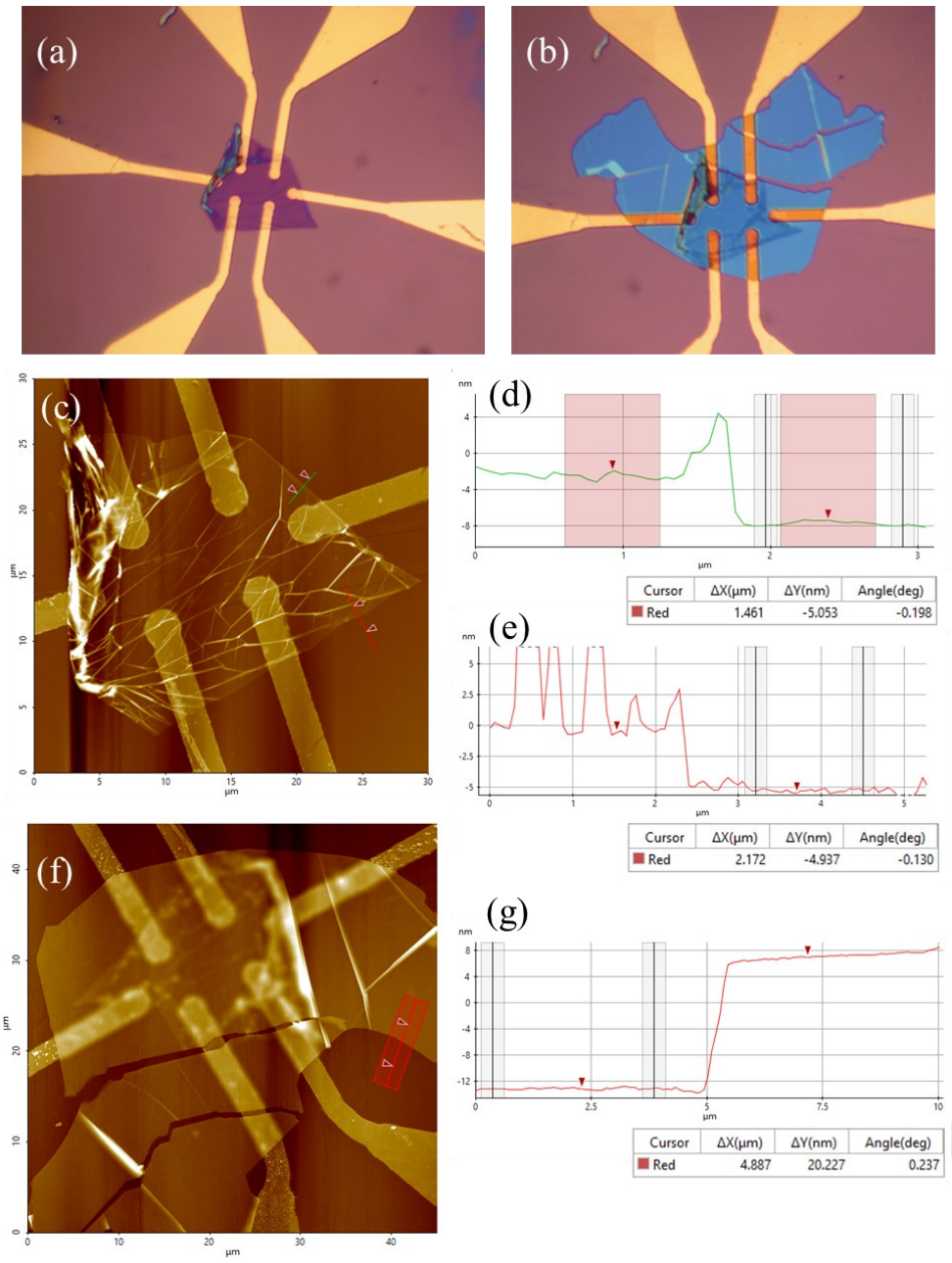


*Figure A.7 Exfoliated multi-layer graphene devise GrE_SM10 covered by h-BN. (a) OM image taken before covering the device with an h-BN flake. (b) OM image taken after covering the device with an h-BN flake. (c) Atomic Force Microscopy (AFM) image of the device before covering it with h-BN. (d) Height profile marked in green on the AFM image in (c). (e) Height profile marked in red on the AFM image in (c). (f) AFM image of the device after covering it with h-BN. (g) Height profile marked in red on the AFM image in (f). Note: The OM images capture the overall appearance of the device before and after the h-BN covering, while the AFM images provide nanoscale details of the device's topography. The corresponding height profiles show the variations in height along the marked lines on the AFM images.*

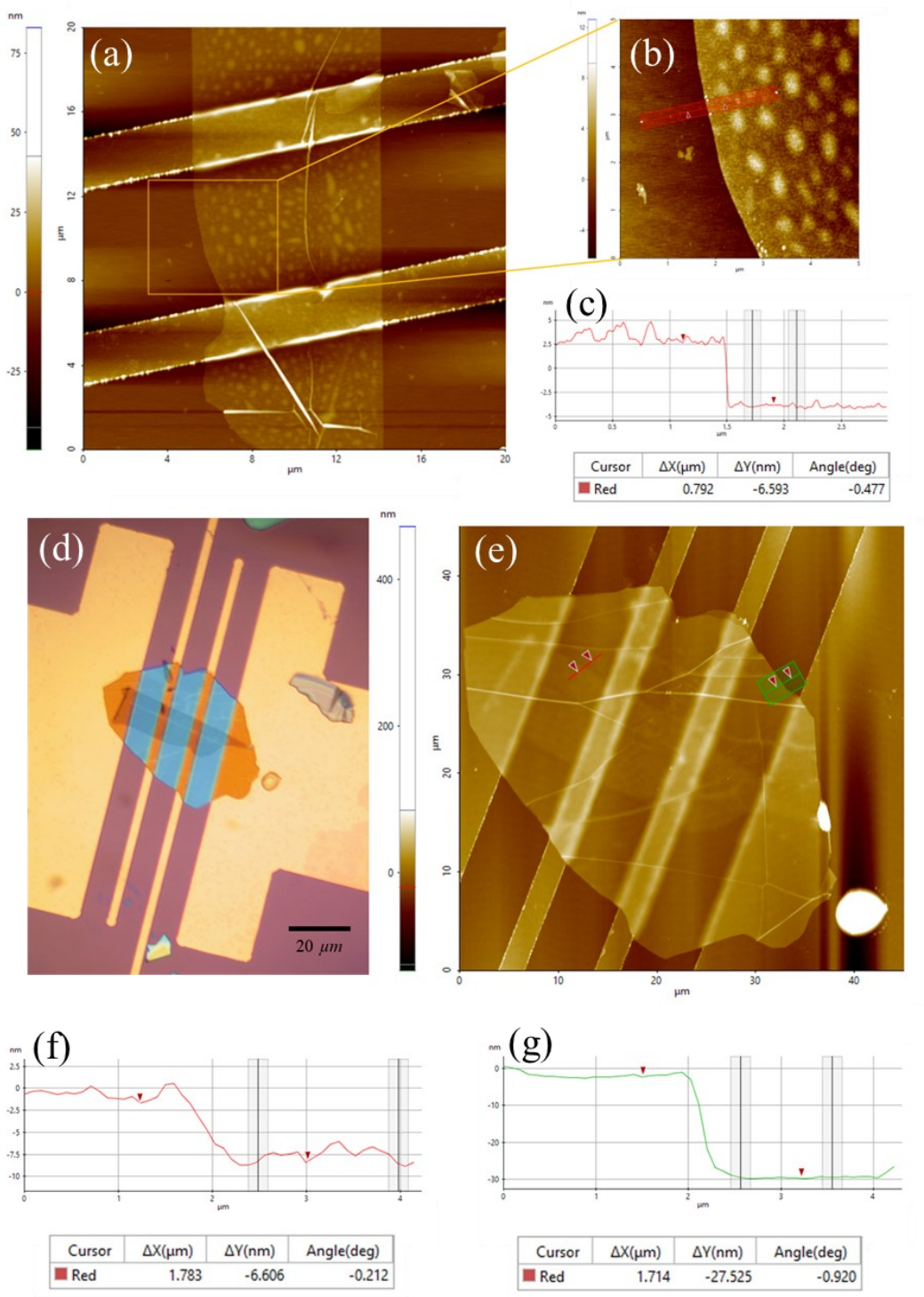


*Figure A.8 OM image and AFM images of h-BN capped multi-layer graphene devise GrE_SM11. (a, b) AFM images taken from the device before covering with h-BN (c) Corresponding height profile obtained from the AFM image in (b). (d) OM image of the h-BN capped devise. (e) AFM image after covering the device with h-BN. (f) Height profile taken along the red line shown in (e), corresponding to the graphene underneath the h-BN. (g) Height profile taken along the green line shown in (e), representing the thickness of the h-BN flake.*

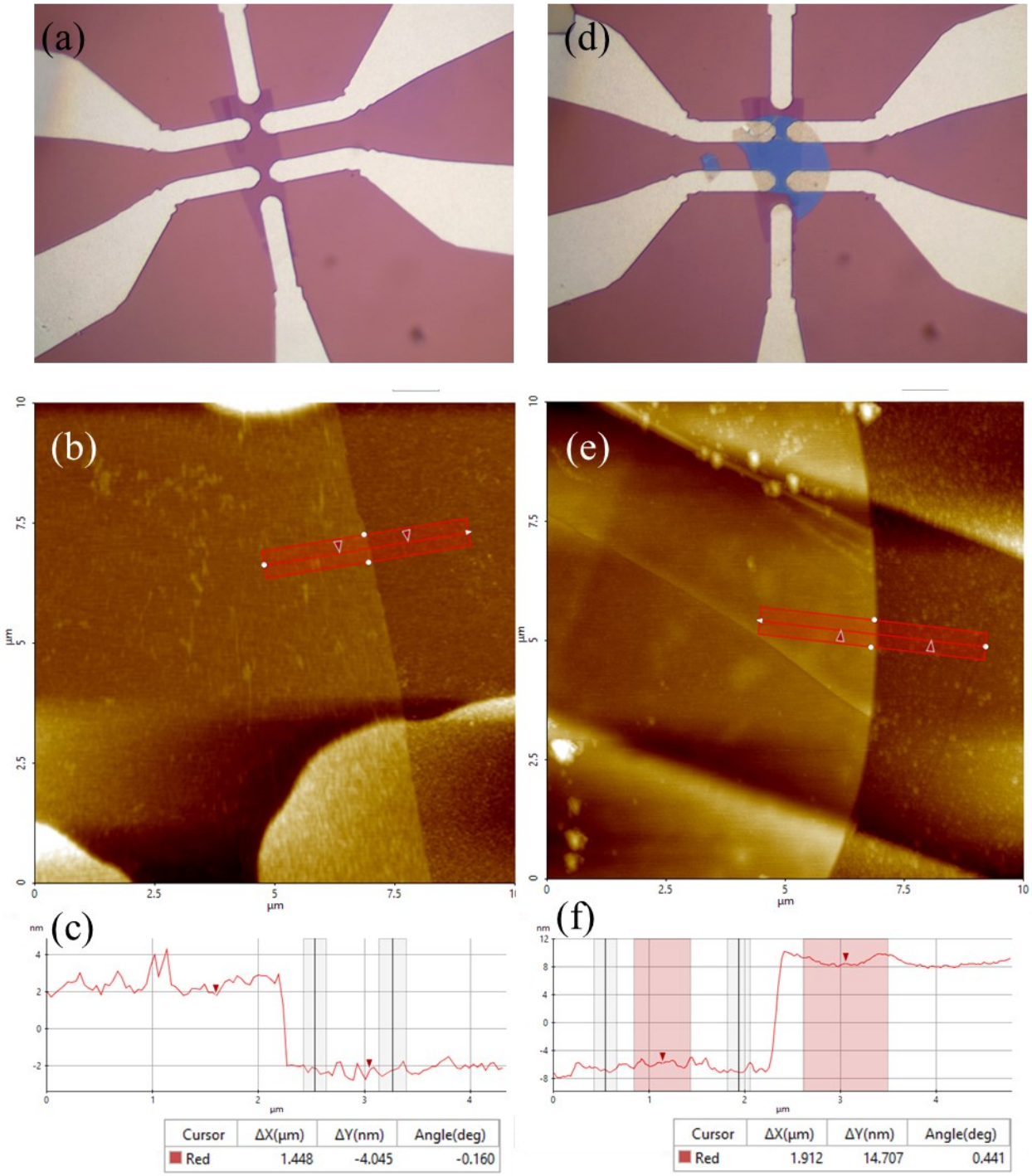


*Figure A.9 OM and AFM images of a partially h-BN capped multi-layer graphene device GrE_SM14. (a, b, c) OM, AFM images and height profile before covering with h-BN respectively. (d, e, f) OM, AFM images and height profile after covering with h-BN respectively.*

### *Appendix B.2 Measurements of graphene devices*

Measurements were done utilizing APD cryogenics closed cycle refrigerator that can cool a sample down to 10K. The system is equipped with a vacuum chamber and a water-cooled magnet, vacuum pump, $^4$He compressor, digital multimeters, and computer system for data collection.

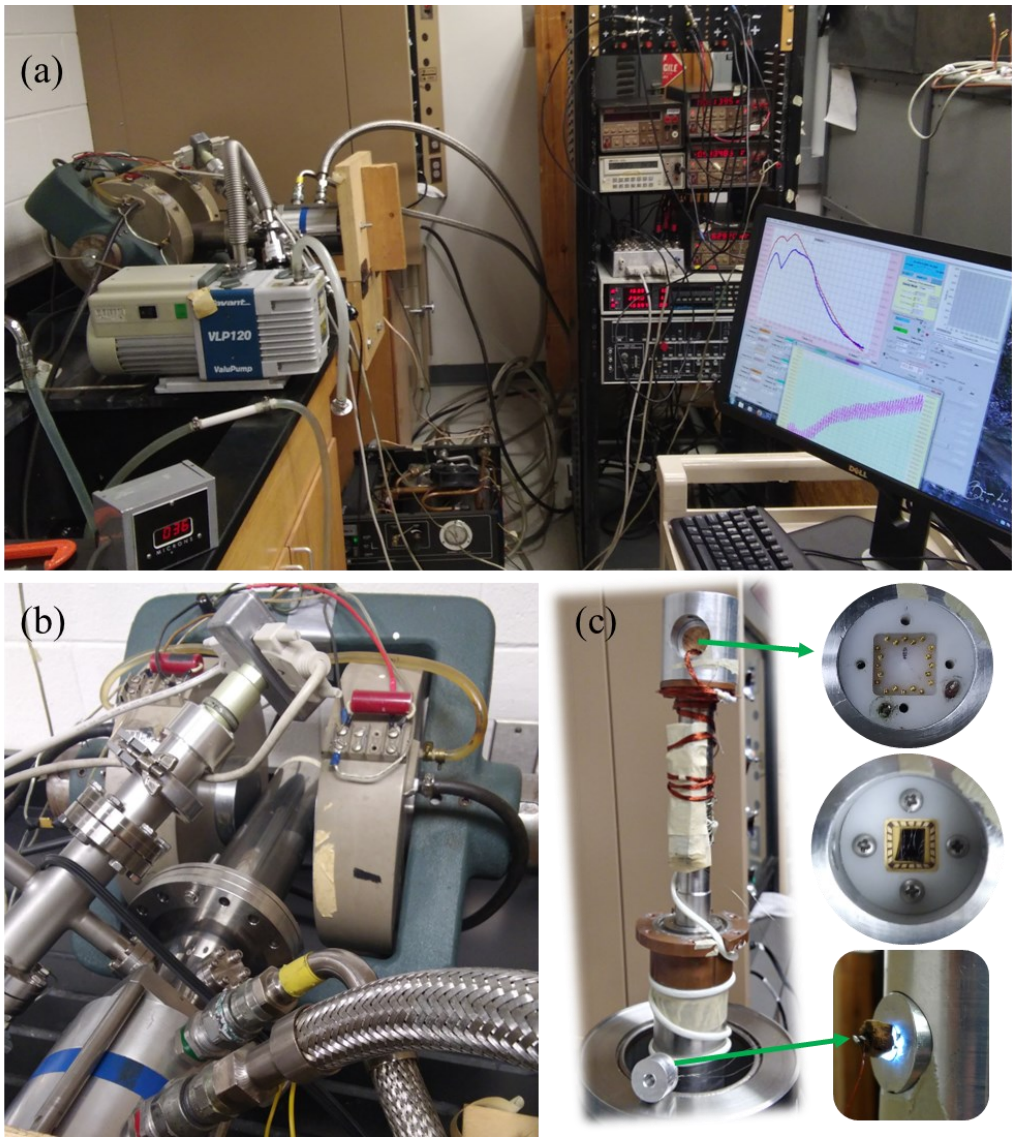


*Figure A.10 Closed cycle refrigerator and measurement setup. (a) Overview of the complete system, showcasing the vacuum pump, cold head, magnet, compressor measurement rack, and computer system. (b) Assembled cold head in detail. (c) Composite figure revealing the cold head without the radiation shield and vacuum chamber cover, alongside the sample holder with the illumination assembly.*

## Appendix C: Permission from publishers for reusing the published materials

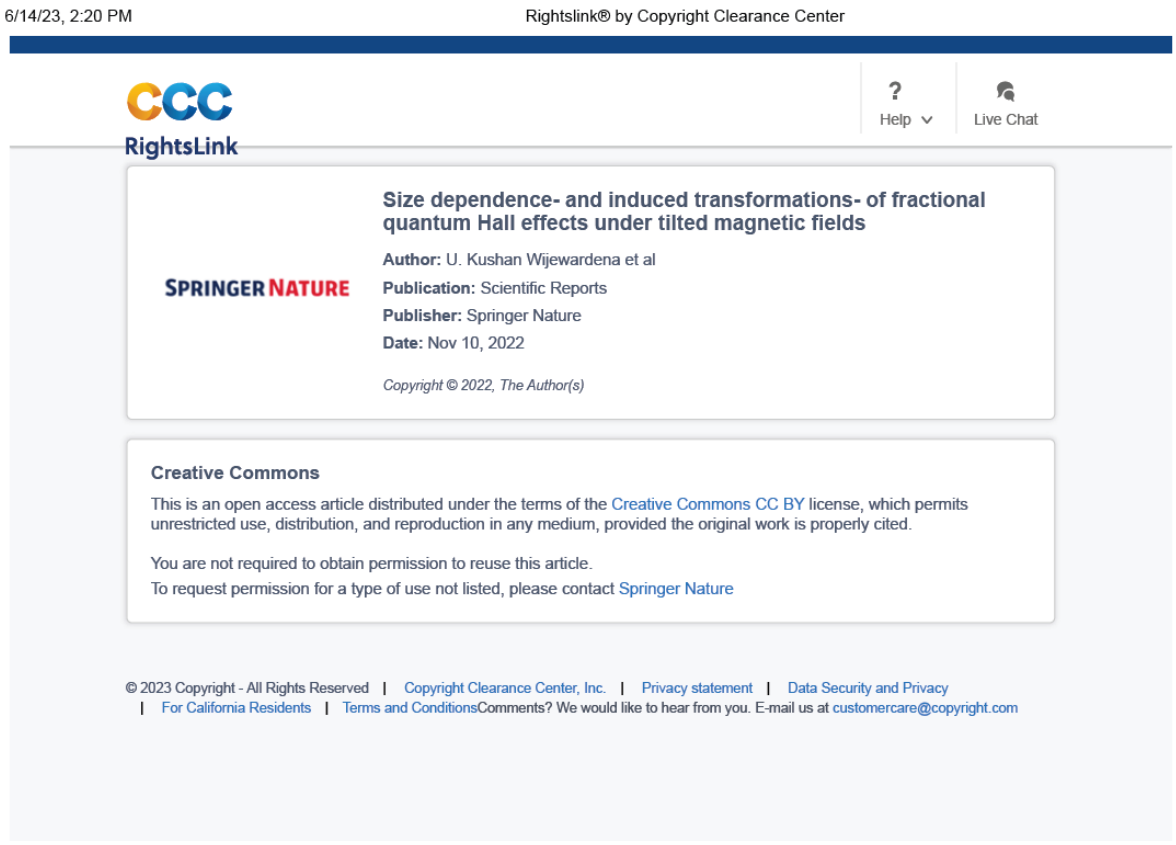

SPRINGER NATURE

## Effects of Long-Time Current Annealing to the Hysteresis in CVD Graphene on SiO2

**Author:** U. Kushan Wijewardena et al
**Publication:** MRS Advances
**Publisher:** Springer Nature
**Date:** Sep 17, 2019



### Order Completed

Thank you for your order.

This Agreement between U. Kushan Wijewardena ("You") and Springer Nature ("Springer Nature") consists of your license details and the terms and conditions provided by Springer Nature and Copyright Clearance Center.

Your confirmation email will contain your order number for future reference.

| | |
|---|---|
| License Number | 5567770504428 |
| License date | Jun 14, 2023 |

Printable Details

#### Licensed Content

| | |
|---|---|
| Licensed Content Publisher | Springer Nature |
| Licensed Content Publication | MRS Advances |
| Licensed Content Title | Effects of Long-Time Current Annealing to the Hysteresis in CVD Graphene on SiO2 |
| Licensed Content Author | U. Kushan Wijewardena et al |
| Licensed Content Date | Sep 17, 2019 |

#### Order Details

| | |
|---|---|
| Type of Use | Thesis/Dissertation |
| Requestor type | academic/university or research institute |
| Format | electronic |
| Portion | full article/chapter |
| Will you be translating? | no |
| Circulation/distribution | 1 - 29 |
| Author of this Springer Nature content | yes |

#### About Your Work

| | |
|---|---|
| Title | Fractional Quantum Hall Effect Under Tilted Magnetic Fields in GaAs/AlGaAs Heterostructure Hall Bar Devices, and the Effect of Current Annealing in CVD Graphene Devices |
| Institution name | Georgia State University |
| Expected presentation date | Aug 2023 |

#### Additional Data

| | |
|---|---|
| Order reference number | 1987 |